

UNIVERSITY OF SOUTHAMPTON

# **Disc Winds Matter: Modelling Accretion and Outflow on All Scales**

by

James Matthews

A thesis submitted in partial fulfillment for the  
degree of Doctor of Philosophy

in the  
Faculty of Physical Sciences and Engineering  
Department of Physics & Astronomy

April 2016

*“Here, on the edge of what we know, in contact with the ocean of the unknown, shines the mystery and the beauty of the world.*

*And it’s breathtaking.”*

Seven Brief Lessons on Physics, Carlo Rovelli

*“Good enough for government work.”*

Christian Knigge

UNIVERSITY OF SOUTHAMPTON

## *Abstract*

Faculty of Physical Sciences and Engineering  
Department of Physics & Astronomy

Doctor of Philosophy

by James Matthews

Outflows are ubiquitous in accreting systems across 10 orders of magnitude in mass. They can take the form of highly collimated radio jets, or less collimated, mass loaded winds emanating from the accretion disc. Perhaps the most spectacular evidence for accretion disc winds is the blue-shifted, broad absorption lines (BALs) in UV resonance lines, seen in cataclysmic variables (CVs) and approximately 20% of quasars. In addition to directly producing absorption in the spectrum, it is possible that accretion disc winds may significantly affect the line and continuum *emission* from CVs and quasars – as a result, they may even dominate the spectral appearance of such objects. When one considers that disc winds are also a possible mechanism for AGN feedback, it becomes clear that understanding the physics and true spectral imprint of these winds is of wide-ranging astrophysical significance.

In this thesis I use the confusingly named Monte Carlo radiative transfer (MCRT) code, PYTHON, to conduct a series of MCRT and photoionization simulations designed to test simple biconical disc wind models. I provide a detailed description of these methods, focusing particularly on the macro-atom implementation developed by Leon Lucy. First, I apply them to the optical spectra of CVs. Second, I conduct tests of quasar unification models. Finally, informed by the previous study, I use Sloan Digital Sky Survey and Hubble Space Telescope data to test the models in an empirical way, by using emission line equivalent widths as a probe of unification geometries.

Overall, the work presented here suggests that *disc winds matter*. They not only act as a spectral ‘filter’ for the underlying accretion continuum, but may actually dominate the emergent spectrum from accreting objects. As a result, unveiling their driving mechanisms, mass-loss rates, and ionization structure is an important goal for the astronomical community.

# Contents

<b>Abstract</b>	<b>ii</b>
<b>1 Introduction</b>	<b>1</b>
1.1 The Physics of Accretion . . . . .	3
1.1.1 Spherical Accretion and The Eddington Limit . . . . .	4
1.1.2 Accretion Discs . . . . .	5
1.1.2.1 Steady-state Accretion Discs: The $\alpha$ -prescription . . . . .	6
1.1.3 Boundary layers, black hole spin and the ISCO . . . . .	7
1.1.4 The emergent spectrum . . . . .	9
1.2 Accreting Compact Binaries . . . . .	13
1.2.1 Roche Lobe-Overflow . . . . .	13
1.2.2 Cataclysmic Variables . . . . .	14
1.2.2.1 Dwarf Novae and the Disc-instability Model . . . . .	15
1.2.2.2 Nova-like Variables . . . . .	16
1.2.3 Low Mass X-ray Binaries . . . . .	19
1.3 Quasars and Active Galactic Nuclei . . . . .	20
1.3.1 AGN Unification and the dusty Torus . . . . .	21
1.3.2 X-ray Properties of AGN . . . . .	24
1.3.2.1 The Soft X-ray Excess . . . . .	26
1.3.3 The Broad Line Region: Connection to winds and unification . . . . .	26
1.4 The Current Understanding of the Disc Continuum . . . . .	27
1.4.1 The Spectral shape of CV discs . . . . .	27
1.4.2 The Big Blue Bump in AGN . . . . .	28
1.4.2.1 The Accretion Disc Size Problem . . . . .	28
1.4.2.2 Fitting AGN Spectra and the 1000Å Break . . . . .	29
1.5 The Universality of Accretion . . . . .	29
1.5.1 The RMS-flux relation . . . . .	30
1.5.2 Accretion states and disc-jet coupling . . . . .	30
1.5.3 A Global Picture . . . . .	31
<b>2 Accretion Disc Winds</b>	<b>33</b>
2.1 Observational Evidence . . . . .	33
2.1.1 Cataclysmic Variables . . . . .	34
2.1.2 X-ray Binaries . . . . .	36
2.1.3 AGN and Quasars . . . . .	38
2.1.3.1 Broad Absorption Line Quasars . . . . .	38

2.1.3.2	Warm Absorbers . . . . .	41
2.1.3.3	Ultra-fast Outflows . . . . .	42
2.1.4	Stellar Winds . . . . .	43
2.1.4.1	Clumping in stellar winds . . . . .	44
2.1.5	Outflow Physics . . . . .	45
2.2	Driving Mechanisms . . . . .	45
2.2.1	Thermal Winds . . . . .	46
2.2.2	Radiatively Driven Winds . . . . .	47
2.2.3	Line-driven Winds . . . . .	47
2.2.4	Magnetic Winds . . . . .	48
2.3	Accretion Disc Wind Models . . . . .	49
2.3.1	MCGV95: A Line-driven Wind Model for AGN . . . . .	49
2.3.2	De Kool & Begelman: A Radiatively Driven, Magnetically Confined Wind . . . . .	50
2.3.3	Elvis 2000: A Structure for Quasars . . . . .	51
2.3.4	Proga et al.: Line-driven Hydrodynamic Models for AGN and CVs . . . . .	51
2.4	A Kinematic Prescription . . . . .	54
2.5	The big picture: AGN Feedback . . . . .	56
2.5.1	Observational evidence for feedback . . . . .	57
2.5.2	Alternative Explanations . . . . .	61
<b>3</b>	<b>Radiative Transfer and Ionization</b> . . . . .	<b>62</b>
3.1	Fundamentals of Radiative Transfer . . . . .	62
3.1.1	Spectral Line Formation . . . . .	64
3.1.2	Local thermodynamic equilibrium . . . . .	65
3.1.2.1	Dilute approximation . . . . .	66
3.1.3	The Two Level Atom . . . . .	66
3.1.3.1	Einstein coefficients and the two-level atom . . . . .	67
3.1.4	The Sobolev Approximation . . . . .	67
3.1.4.1	Escape Probabilities . . . . .	68
3.1.5	Monte Carlo approaches . . . . .	68
3.2	PYTHON: A Monte Carlo Ionization and Radiative Transfer Code . . . . .	69
3.2.1	Basics . . . . .	69
3.2.2	Radiation Packets . . . . .	71
3.2.3	Radiative Transfer procedure . . . . .	72
3.3	Macro-atoms . . . . .	73
3.3.1	Transition Probabilities . . . . .	74
3.3.2	Rate equations . . . . .	75
3.3.2.1	Collision strengths . . . . .	77
3.3.3	Macro-atom estimators . . . . .	78
3.3.4	$k$ -packets . . . . .	79
3.3.5	Putting it all together . . . . .	79
3.3.6	Ionization Fractions and Level Populations . . . . .	79
3.4	A hybrid line transfer scheme: including simple-atoms . . . . .	82
3.4.1	Line Transfer . . . . .	82
3.4.2	Estimators . . . . .	82
3.4.3	Ionization and Excitation . . . . .	83

3.5	Heating And Cooling Balance . . . . .	83
3.5.1	Convergence . . . . .	84
3.6	Spectral Cycles . . . . .	84
3.7	Atomic Data . . . . .	86
3.8	Clumping . . . . .	86
3.8.1	Motivation . . . . .	86
3.8.2	Microclumping . . . . .	87
3.9	Code Validation . . . . .	88
3.9.1	Testing against Cloudy . . . . .	88
3.9.2	Testing against Tardis . . . . .	88
3.10	Code Maintenance and Version Control . . . . .	88
3.10.1	Parallelisation . . . . .	88
4	<b>Quasar Emission Line Equivalent Widths as Probes of Orientation and Unification</b>	89
4.1	Data Sample . . . . .	89
4.2	The Angular Distribution of Emission from an Accretion Disc and Broad-Line Region . . . . .	92
4.2.1	Standard Thin Disc Models . . . . .	92
4.2.2	Including GR, Comptonisation and Opacity Effects . . . . .	93
4.2.3	Alternative Continuum Models: Irradiation and Truncated Discs . . . . .	93
4.3	Predicted EW distributions compared to observations: A Monte Carlo approach . . . . .	93
4.4	Discussion . . . . .	97
4.4.1	Radio Observations . . . . .	97
4.4.2	Polarisation . . . . .	97
4.4.3	Compton-thick Fractions . . . . .	97
4.4.4	Theoretical Considerations . . . . .	97
4.5	Conclusions . . . . .	97
	<b>Bibliography</b>	100

# Chapter 1

## Introduction

“And now you’re asking, I don’t know where to begin”

*Mike Vennart, Silent/Transparent*

The release of gravitational potential energy as mass falls towards a compact object is the most efficient energetic process in the universe, even more efficient than nuclear fusion. This *accretion* process is thought to power the huge radiative engines at the centres of many galaxies – accreting supermassive black holes known as active galactic nuclei (AGN). As the matter falls into the potential well of the black hole it often forms an accretion disc. This disc is an efficient radiator of the gravitational potential energy released. and can sometimes outshine the entire stellar population of the galaxy, appearing as a quasi-stellar object (QSO) or *quasar*. As well as powering, AGN, accretion discs are present in X-ray binaries (XRBs), young-stellar objects (YSOs) and cataclysmic variables (CVs). Accretion is a universal process; broadly speaking, the physics is similar regardless of whether matter is falling on to a  $\sim 1 M_{\odot}$  neutron star or white dwarf, or a  $\sim 10^{10} M_{\odot}$  black hole.

Outflows are ubiquitous in accreting systems. We see collimated radio jets in AGN (Hazard et al. 1963; Potash & Wardle 1980; Perley et al. 1984; Marscher 2006) and XRBs (Belloni 2010), and there is even evidence of radio emission in CVs (Benz et al. 1983; Coppejans et al. 2015). These radio jets tend to appear in specific accretion states (Fender 2001; Fender et al. 2004; Körding et al. 2008), implying an intrinsic connection to the accretion process. Even more intriguing, in XRBs less collimated, mass-loaded

outflows or *winds* are observed in the opposite accretion state, possibly emanating from the accretion disc. Evidence for disc winds is widespread across the mass range, but perhaps the most spectacular indication is the blue-shifted, broad absorption lines (BALs) in the rest-frame ultraviolet (UV) seen in high-state CVs (Heap et al. 1978; Greenstein & Oke 1982; Cordova & Mason 1982) and the so-called broad absorption line quasars (BALQSOs) that make up 20 – 40% of quasars (Weymann et al. 1991; Knigge et al. 2008; Allen et al. 2011). BALs and ‘P-Cygni’ profiles (Struve 1935; Rottenberg 1952) are also seen in stellar winds (e.g. Cassinelli 1979) and sometimes even in the optical spectra of CVs (Patterson et al. 1996; Ringwald & Naylor 1998; Kafka & Honeycutt 2004). Broad, blue-shifted absorption is also observed in the Fe K $\alpha$  line in some AGN (Reeves et al. 2003; Pounds & Reeves 2009; Tombesi et al. 2010) – these are known as ultra-fast outflows or UFOs.

The astrophysical significance of disc winds extends, quite literally, far beyond the accretion environment. They offer a potential mechanism by which the central accretion engine can interact with the host galaxy and interstellar medium via a ‘feedback’ mechanism (King 2003; Fabian 2012). Feedback is required in models of galaxy evolution (Springel et al. 2005) and may explain the famous ‘ $M_{BH} - \sigma$ ’ (Silk & Rees 1998; Häring & Rix 2004) and ‘ $M_{BH} - M_{bulge}$ ’ (Magorrian et al. 1998) relations. Winds also offer a natural way to *unify* much of the diverse phenomenology of AGN, CVs and XRBs. This principle of unification can be applied along more than one ‘axis’ of parameter space. For example, there exist elegant models that attempt to explain *all* of the behaviour of quasars with only a central black hole, a jet, an accretion disc, and an associated outflow, just by varying the viewing angle (Elvis 2000). Similarly elegantly, it has been shown that much of the behaviour of XRBs is directly applicable to AGN (McHardy et al. 2006), and models of outflows in CVs have been successfully ‘scaled-up’ and applied to quasars and AGN (e.g. Higginbottom et al. 2013).

Despite their clear importance and ubiquity, there are still many unanswered questions relating to the true impact of winds and their underlying physical origins. Here, I aim to address some of these questions, and take steps towards building a more holistic picture of the impact of winds on the spectral appearance and accretion physics of disc systems. This thesis is structured as follows. In the remainder of this chapter, I will give the background accretion theory and detail the successes and failures of accretion disc models when compared to observations, as well as describing the different classes

of accreting objects in more detail. In chapter 2, I dedicate some time to specifically discussing the theory of, and observational evidence for, accretion disc winds. In chapter 3, I outline the Monte Carlo radiative transfer (MCRT) and photoionization methods I have used in order to investigate the impact of disc winds on the spectra of accreting systems. The next three chapters contain three separate submitted papers, in which I discuss the impact of disc winds on the spectra of CVs (Chapter 4), and test disc wind quasar unification models (Chapters 5 and 6). In chapter 8, I summarise my findings and their astrophysical significance, and discuss potential avenues for future work.

## 1.1 The Physics of Accretion

The basic phenomenon of accretion- matter falling into a gravitational potential well- is ubiquitous in astrophysics. The energy,  $\Delta E$ , released by a parcel of mass,  $\Delta m$ , falling from infinity onto an object of mass  $M$  and radius  $R_*$  is given by

$$\Delta E = \frac{GM\Delta m}{R_*}, \quad (1.1)$$

meaning that the power by mass accreting at a rate  $\dot{M}$  is given by

$$L_{acc} = \frac{GM\dot{M}}{R}. \quad (1.2)$$

We can also characterise the efficiency of any energetic process by relating the energy released to the rest mass energy of the parcel of mass, such that

$$\Delta E = \eta\Delta Mc^2, \quad (1.3)$$

where  $\eta$  is the radiative efficiency. Similarly, in terms of luminosity,  $L$ ,

$$L = \eta\dot{M}c^2, \quad (1.4)$$

Nuclear fusion is one of the more efficient energetic processes in the universe, with an efficiency of  $\eta = 0.007$ . If we rearrange the above equations in terms of  $\eta$  we find

$$\eta = \frac{G}{c^2} \frac{M}{R_*}. \quad (1.5)$$

In other words, the efficiency of accretion is directly related to the *compactness*,  $M/R_*$ , of the central object.

### 1.1.1 Spherical Accretion and The Eddington Limit

The simplest geometry one might propose for accretion would be one in which a central mass accretes matter from an all-encompassing cloud. The process of spherical accretion has come to be known as Bondi-Hoyle-Lyttleton accretion ([Hoyle & Lyttleton 1939](#); [Bondi & Hoyle 1944](#)). In particular, [Bondi \(1952\)](#) studied spherically symmetric accretion onto a point mass and derived the Bondi radius,

$$r_B = \frac{GM}{c_S^2}, \quad (1.6)$$

where  $c_S = c_S(r_B)$  is the sound speed as a function of radius. The Bondi radius represents a critical point inside which the material is supersonic and will accrete on the free-fall timescale.

When this timescale is long enough, the accreting matter can radiate away its potential energy, generating a luminosity  $L$ . This radiation will induce a force on electrons, given by

$$F_{rad} = \frac{L\sigma_T}{4\pi r^2 c}, \quad (1.7)$$

where  $\sigma_T = 6.65 \times 10^{-25} \text{ cm}^2$  is the Thomson cross-section. If this radiation force term dominates over the gravitational force, then the material will no longer fall inwards. Consider radiation pressure acting on electron-proton pairs, for which the gravitational force is approximately given by  $GMm_p/r^2$ . Combining this expression with equation 1.7 gives a natural maximum accretion luminosity, known as the *Eddington limit*, of

$$L_{Edd} = \frac{4\pi GMm_p c}{\sigma_T}, \quad (1.8)$$

with an associated Eddington accretion rate of

$$\dot{M}_{Edd} = \frac{L_{Edd}}{\eta c^2}. \quad (1.9)$$

The Eddington limit makes a number of assumptions, namely that the accretion flow is steady, spherically symmetric, ionized, and has its opacities dominated by electron

scattering. Clearly, there are many astrophysical situations where this does not hold. For example, the recent outburst of V404 Cyg showed wildly variable luminosities on short timescales (see, e.g., [Kuulkers et al. 2015](#); [Motta et al. 2015](#), among many, many ATels), and in any binary system or disc dominated system the assumption of spherical symmetry will break down. Nevertheless, the Eddington limit provides a good order of magnitude estimate of the maximum luminosity of an accreting object, and also provides a useful way of parameterising accretion rate, as it scales linearly with mass. It can also be used to characterise the *state* of an accretion disc. In general, sources above  $\sim 0.1 L_{Edd}$  find themselves in a ‘soft’ or thin-disc state, whereas for much lower Eddington fractions, sources will possess advection-dominated accretion flows (ADAFs; [Narayan & Yi 1994, 1995](#)). It is also clear that around the Eddington limit radiation pressure must play a major role in determining the disc morphology (see section [2.2.2](#)).

### 1.1.2 Accretion Discs

In many astrophysical situations – for example, in binary systems and gas clouds orbiting BHs – any accreting matter will possess some net angular momentum. If the medium is dense enough, collisions between particles will be frequent, but the total angular momentum vector of two colliding particles will always be conserved. This provides a mechanism for a gas cloud to relax to its minimum energy state – an accretion disc.

As well as losing gravitational potential energy as it falls towards the central mass, a parcel of matter must also lose its angular momentum. Crucially, accretion discs provide a way for this to happen. If the disc overall maintains the same total angular momentum, it follows that angular momentum must therefore be transported outwards. The mechanism for transporting angular momentum outwards is unknown, and is one of the biggest weaknesses of current accretion disc theory. The most commonly invoked candidate is the magnetorotational instability (MRI; [Balbus & Hawley 1991](#)), in which accretion discs are subject to a strong shearing instability even when the magnetic field is weak. Possible alternative are that the angular momentum is lost via a magneto-hydrodynamic outflow ([Blandford & Payne 1982](#)) or spiral shock waves ([Ju et al. 2016](#)). An efficient mechanism for angular momentum transport is necessary as the viscosity introduced in the next section is generally inefficient in this regard (?).

### 1.1.2.1 Steady-state Accretion Discs: The $\alpha$ -prescription

The so-called  $\alpha$ -disc model developed by (Shakura & Sunyaev 1973, hereafter SS73) and Lynden-Bell (1969) is currently the leading candidate for explaining how energy and angular momentum is transported an accretion disc. The starting point for this model is the parameterisation of viscosity,  $\nu'$ , using the simple form

$$\nu' = \alpha c_s H, \quad (1.10)$$

where  $H$  is the scale height of the disc,  $\alpha$  is a parameter  $\leq 1$  and  $c_s$  is the sound speed. Viscous torques then allow the conversion of orbital kinetic energy into heat, which can be radiated away. If we make one further assumption, that the accretion rate is constant throughout the disc, we can write down a mass continuity equation valid at all radii, given by

$$\dot{M} \equiv 2\pi R V_R \Sigma = 0, \quad (1.11)$$

where  $\Sigma$  is the surface density at that point. The angular momentum equation then becomes

$$\nu' \Sigma = \frac{\dot{M}}{3\pi} \left[ 1 - \left( \frac{R}{R_*} \right)^{1/2} \right]. \quad (1.12)$$

The viscous torques throughout the disc cause a local loss of mechanical energy, allowing one to derive (see, e.g. Frank et al. 1992) a rate of viscous dissipation, per unit area, given by

$$D(R) = \frac{1}{2} \nu' \Sigma (R \Omega')^2. \quad (1.13)$$

Here,  $D(R)$  is proportional to the derivative of the angular velocity,  $\Omega' = d\Omega/dR$ . By combining equations 1.13 and 1.12 we can show that the viscous dissipation rate is

$$D(R) = \frac{GM\dot{M}}{8\pi R^3} \left[ 1 - \left( \frac{R}{R_*} \right)^{1/2} \right] \quad (1.14)$$

where we have also set the angular velocity to the Keplerian velocity. This expression is independent of viscosity – which is fortunate, because we do not know what value of  $\alpha$  to use in equation 1.10. This result comes about because of the implicit assumption that the viscosity regulates the mass accretion rate so as to achieve a steady state.

We can now integrate across both sides of the whole disc to obtain the disc luminosity,

$$L_{disc} = 2 \int_{R_*}^{\infty} D(R) 2\pi R dR = \frac{GM\dot{M}}{2R_*} = \frac{1}{2} L_{acc}. \quad (1.15)$$

This result can also be shown by considering the binding energy of gas at  $R_*$  and infinity. From equation 1.14 one can also derive an effective temperature distribution, by setting

$$\sigma T_{eff}^4(R) = D(R), \quad (1.16)$$

which then gives

$$T_{eff}(R) = T_* \left[ 1 - \left( \frac{R}{R_*} \right)^{1/2} \right]^{1/4}, \quad (1.17)$$

where

$$T_* = \left( \frac{3GMM}{8\pi R_*^3 \sigma} \right)^{1/4}. \quad (1.18)$$

When  $R \gg R_*$  this simplifies to

$$T_{eff}(R) = T_* (R/R_*)^{-3/4}. \quad (1.19)$$

Now we have not only derived the total luminosity of an accretion disc, but also the effective temperature profile which will govern the shape of the emergent SED. This temperature profile is shown in figure 1.1 for three different compact objects, assuming an Eddington fraction of 0.2.

### 1.1.3 Boundary layers, black hole spin and the ISCO

In equation 1.15 I showed that  $L_{disc} = 1/2 L_{acc}$ . One might then ask: where does the rest of the luminosity go? The answer is dependent on the compact object in question. In an accreting WD, the rotating matter must eventually deposit itself on the surface of the WD. This is illustrated in figure 1.2, which shows the angular velocity as a function of radius in a disc around a compact object rotating with angular velocity  $\Omega_*$ . The boundary layer (BL) is the region to the left of the dotted line, inside the maximum of  $\Omega_K$ , the Keplerian angular velocity. The luminosity of the boundary layer is (Frank et al. 1992)

$$L_{BL} = \frac{1}{2} \frac{GM\dot{M}}{R} \left[ 1 - \left( \frac{\Omega_*}{\Omega_K(R_*)} \right) \right]^2, \quad (1.20)$$

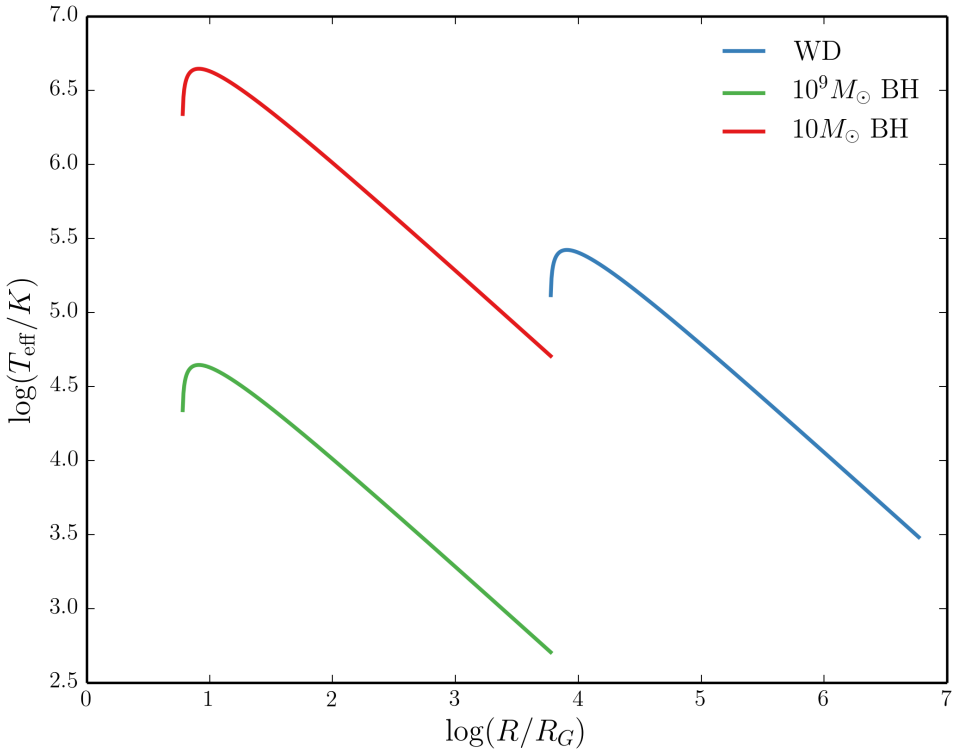


FIGURE 1.1: The temperature profile of an accretion disc for three different classes of compact object.

where  $\Omega_K(R_*)$  is the Keplerian angular velocity at  $R_*$ , assuming the thickness of the BL is small. When  $\Omega_K(R_*) \gg \Omega_*$ , this reduces to  $L_{BL} = 1/2 L_{acc} = L_{disc}$

In cataclysmic variables, BLs can be approximated with blackbodies and their temperatures estimated indirectly via the [Zanstra \(1929\)](#) method (e.g. [Hoare & Drew 1991, 1993](#)). However, they likely exhibit a variety of atomic features ([Suleimanov et al. 2014](#)). Extreme-UV (EUV) datasets have confirmed the existence of boundary layer emission in non-magnetic CVs ([Mauche 1996](#)), although these observations are limited in number.

Clearly, in BH systems a boundary layer cannot exist in the same way, due to the lack of a physical surface. Instead, the energy must either go into growing the BH, contributing to its angular momentum or being channeled into a jet or other radiative source (see section 1.5.2). The question of what happens at the inner disc edge is complicated further by the fact that the disc cannot extend to the event horizon of the BH. Instead, there is an ‘innermost stable circular orbit’ (ISCO) beyond which the accreting matter will simply fall into the BH along nearly radial paths. The radius of this orbit,  $R_{ISCO}$ ,

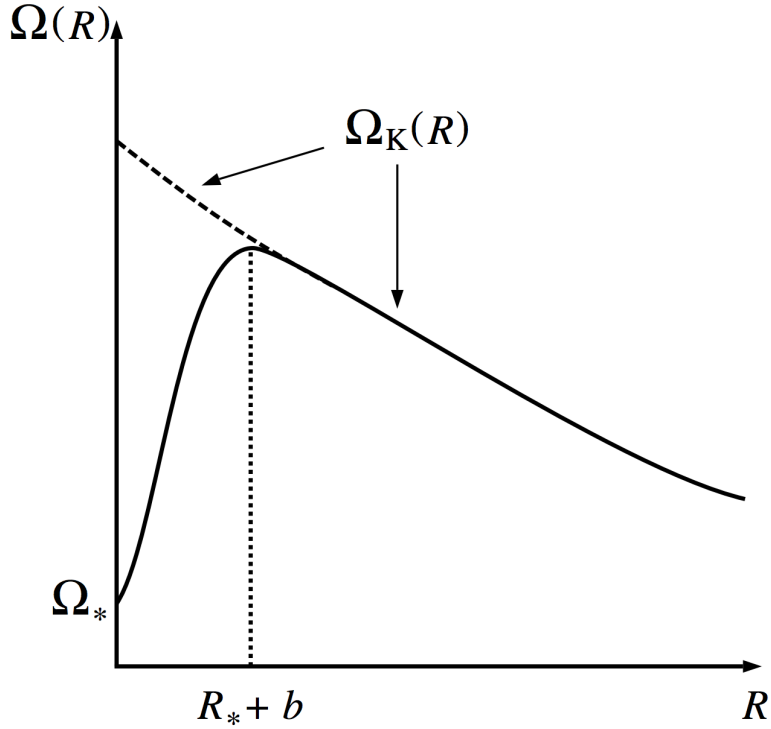


FIGURE 1.2: Credit: Frank et al. 2002. Angular velocity as a function of radius in an accretion disc around a rotating compact object with angular velocity  $\Omega_*$ .  $\Omega_K$  is the Keplerian angular velocity. This graph also helps explain why there is a turnover in the temperature-radius relation, as  $D(R)$  is proportional to the square of the derivative of this quantity.

and the horizon radius,  $R_H$ , is shown for different values of the BH spin parameter,  $a_*$ , in figure 1.3, showing how matter can orbit closer to a prograde spinning BH. In estimating the luminosity of a Keplerian disc around a BH, one should really set  $R_* = R_{ISCO}$  in equation 1.5, giving us the interesting result that rapidly spinning (Kerr) BHs are more radiatively efficient than Schwarzschild BHs.

#### 1.1.4 The emergent spectrum

It is important to recognise that the steady-state disc treatment *does not specify the exact shape of the disc SED*. What it does do is say where energy is originally released. The simplest assumption is that each annulus emits as a blackbody with temperature  $T_{eff}(R)$ , and the specific intensity through the emitting surface thus follows the Planck Law:

$$B_\nu(T) = \frac{2h\nu^3}{c^2} \frac{1}{\exp(h\nu/kT) - 1} \quad (1.21)$$

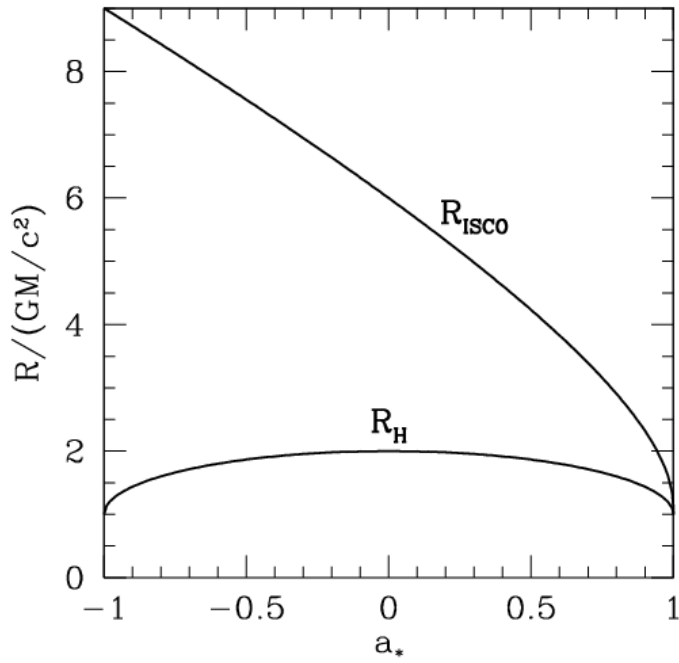


FIGURE 1.3: Credit: Narayan 2014. The radius of the ISCO,  $R_{ISCO}$ , and the horizon,  $R_H$ , is as a function of the BH spin parameter,  $a_*$ .  $a_* = 0$  corresponds to a Schwarzschild BH, and  $a_* = 1$  and  $a_* = -1$  to prograde and retrograde Kerr BHs respectively. Note that this figure ignores the counteracting torque of photons swallowed by the BH, which actually limits  $a_*$  to a value of around 0.998 (Thorne 1974).

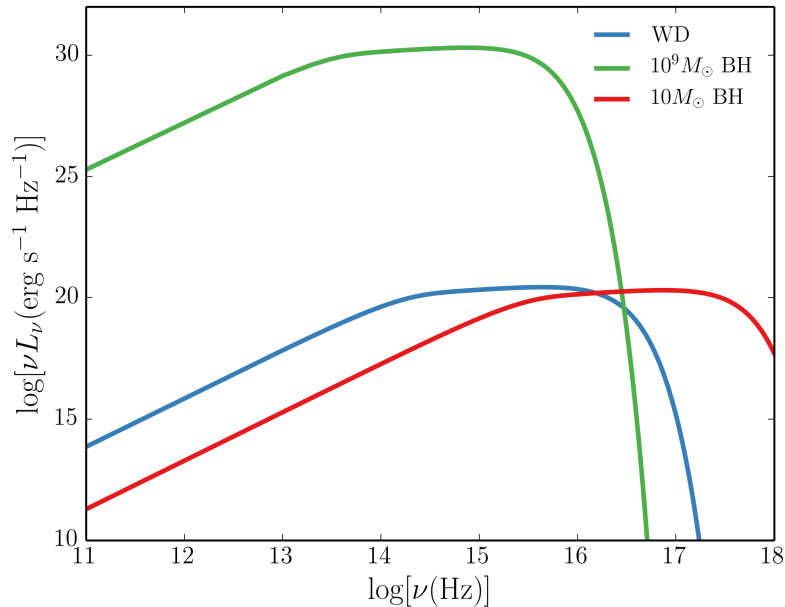


FIGURE 1.4: Accretion disc SEDs for three different compact objects, corresponding roughly to a quasar, an XRB and a CV. The SEDs are computed via an area-weighted sum of blackbodies with effective temperatures governed by equation 1.17, and the  $\nu^{1/3}$  shape in the middle of the spectra can be seen.

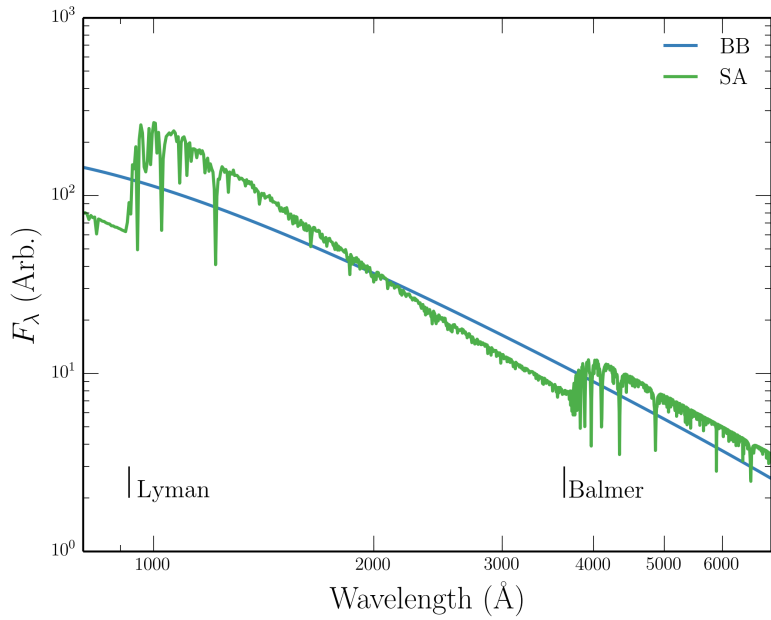


FIGURE 1.5: A comparison between a Planck curve and Kurucz (1991) stellar atmosphere model at  $T_{eff} = 50,000\text{K}$  and surface gravity of  $\log(g) = 5$ . The major photoabsorption edges are marked. Flux is reprocessed into different wavelengths by bound-free opacities, and line blanketing also has a big effect on the spectrum. The Hydrogen and Helium lines also experience significant pressure broadening.

Under this assumption it is possible to show that at intermediate frequencies, where  $kT(R_{max}) \ll h\nu \ll kT_*$ , then the spectrum appears as a ‘stretched blackbody’ with the form

$$F_\nu \propto \nu^{1/3}. \quad (1.22)$$

Figure 1.4 shows the blackbody SEDs expected for the same objects as figure 1.1, in which the  $\nu^{1/3}$  portion can be clearly seen. A disc atmosphere model with frequency-dependent opacity creates a somewhat different (and more realistic) spectrum. Figure 1.5 shows a comparison between a stellar atmosphere model and blackbody model for  $T_{eff} = 50,000\text{K}$ , showing how an annulus at that temperature can have a significantly different spectral shape when one includes frequency-dependent opacities in the atmosphere. It is of course possible that *neither* blackbody or disc atmosphere treatments are realistic. I shall therefore devote a little time to discussing the observational arguments for accretion discs and reviewing the different classes of accreting objects.

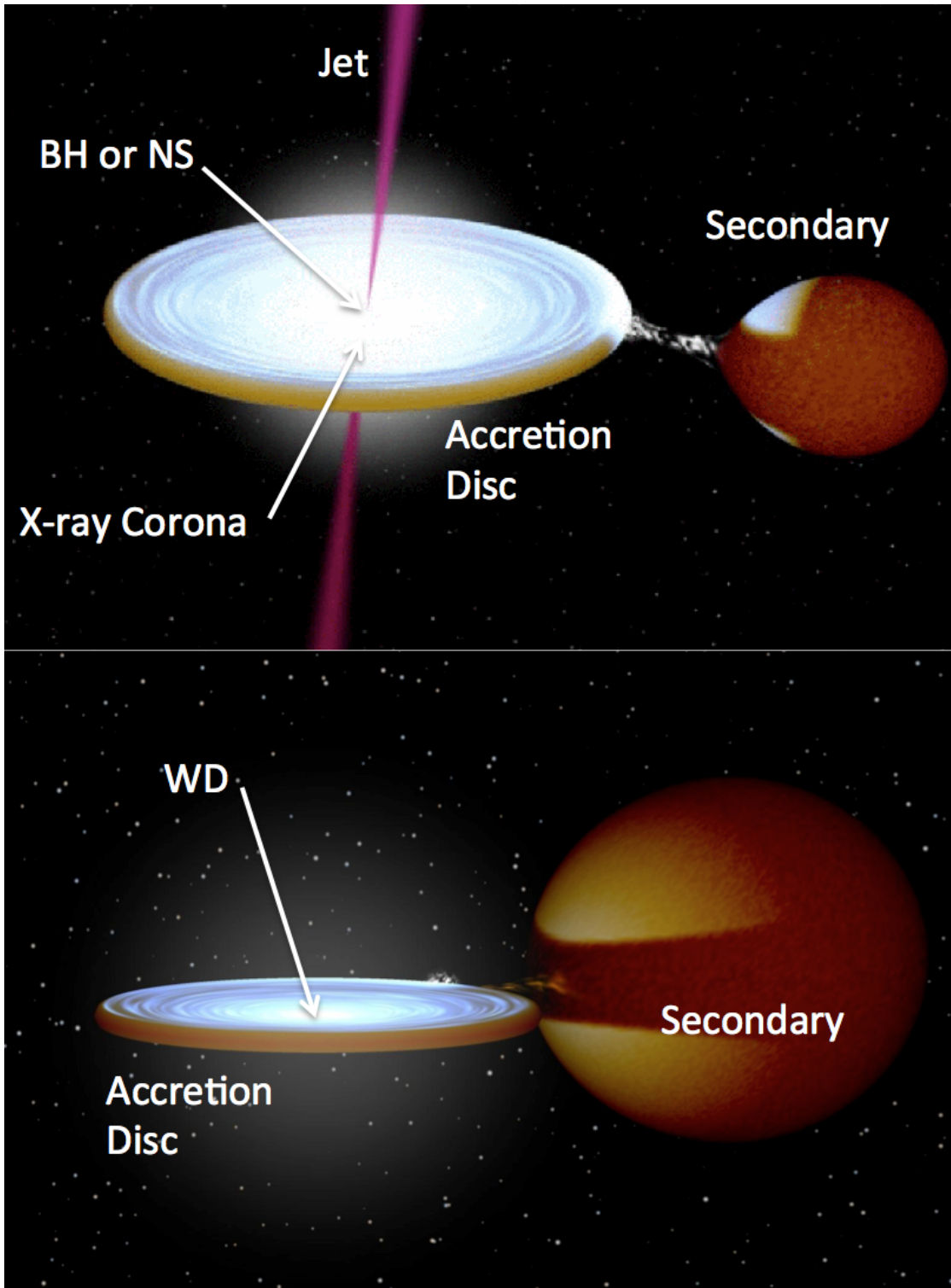


FIGURE 1.6: Credit: Rob Hynes. Artists impression of a low-mass X-ray binary (top) and cataclysmic variable (bottom). The key components are marked, and the clear similarity in overall structure is apparent.

## 1.2 Accreting Compact Binaries

Accreting compact binaries form many different classes, but are all characterised by matter streaming from a donor onto a compact object. When the compact object is more massive than the donor then it is designated as the ‘primary’, and the companion as the ‘secondary’. In high-mass X-ray binaries (HMXBs), the opposite is formally true. There are only two ways by which matter can transfer from the secondary to the compact object. One is by Roche Lobe-overflow (RLOF), whereby stellar evolution causes the donor star to fill its Roche Lobe, the surface of equipotential around the star. The alternative is that the donor may expel material via a disc or radiatively driven stellar wind, allowing some of it to flow onto the compact object. Although accretion from a wind or circumstellar disc is common in HMXBs ([Bartlett 2013](#)), here I will focus on RLOF as it is more common in the systems that possess high-state accretion discs and associated outflows. Two examples of these are shown in figure [1.6](#)

### 1.2.1 Roche Lobe-Overflow

Let us consider a binary system, with masses  $M_1$  and  $M_2$ , at positions  $\vec{r}_1$  and  $\vec{r}_2$ . The Roche potential,  $\Phi_R$ , in this system is then

$$\Phi_R = -\frac{GM_1}{|\vec{r} - \vec{r}_1|} - \frac{GM_2}{|\vec{r} - \vec{r}_2|} - 1/2(\vec{\omega} \times \vec{r})^2, \quad (1.23)$$

where  $\vec{\omega}$  is the angular velocity of the binary and is a vector normal to the orbital plane. This potential is plotted in figure [1.7](#) for a mass ratio,  $q = M_2/M_1$  of 0.25.

In the context of semi-detached binary systems, the most important region of the potential is the dumbbell shaped region enclosing the masses. Each of these enclosed regions is known as the ‘Roche lobe’ of the object and can be expressed approximately in terms of the mass ratio and separation of the system. A good approximation for the size of the Roche lobe takes the form ([Eggleton 1983](#))

$$\frac{R_2}{a} = \frac{0.49q^{2/3}}{0.6q^{2/3} + \ln(1 + q^{1/3})}. \quad (1.24)$$

Here  $R_2$  is the radius of a sphere with the same volume as the Roche lobe for the secondary star, which we can see depends only on  $q$  and the orbital separation,  $a$ . If

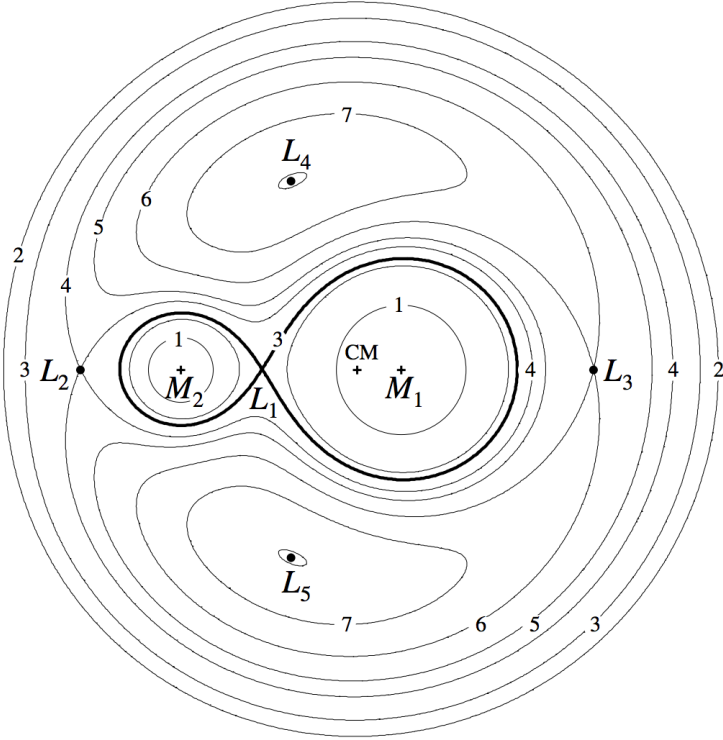


FIGURE 1.7: Credit: Frank et al. 2002. The Roche potential in a binary system for  $q = M_2/M_1$  of 0.25. The Lagrangian points are marked, as are the locations of the individual and system centres of mass.

this secondary expands enough to fill its Roche lobe, then matter will fall onto the other object. This process is known as Roche Lobe overflow (RLOF), and is vitally important in astrophysics. Although caused by stellar evolution, any accretion from RLOF will affect the mass ratio of the binary system and thus itself affects the evolution of binary systems. This helps determine the orbital period distribution of binaries (e.g. Knigge et al. 2011) as well as affecting the delay time distribution of Type Ia Supernovae, for which CVs are one of the progenitor candidates (e.g. Wang & Han 2012). It is also worth noting that the existence of gravitational waves has been required in models to explain the orbital period evolution of CVs since the 1960s (Kraft et al. 1962).

### 1.2.2 Cataclysmic Variables

Cataclysmic variables (CVs) are systems in which a WD accretes matter from a donor star via Roche-lobe overflow (see the ‘CV bible’, Warner 2003). CVs are not always dominated by their accretion luminosity; classical novae and super soft sources (SSS)

emit mostly due to nuclear burning or detonation on the WD surface. Accretion dominated CVs – the focus here – can be classified according to the magnetic field strength of the WD ( $B_{WD}$ ) and photometric activity. Magnetic systems are classified as either ‘Polars’ ( $B_{WD} \gtrsim 10^7$  G) or ‘Intermediate Polars’ ( $10^6 \lesssim B_{WD} \gtrsim 10^7$  G); in these systems the accretion flow inside the some critical radius (related to the Alfven radius) is dominated by the WDs magnetic field (e.g. [Patterson 1994](#)). In polars, this radius is large enough, due to the strong magnetic field, that no disc forms at all ([Liebert & Stockman 1985](#)). When  $B_{WD} \lesssim 10^6$  G then the accreting material can fall onto the WD via a disc, and the CV is classified as non-magnetic. There are two main types of non-magnetic CVs; dwarf novae and nova-like variables.

### 1.2.2.1 Dwarf Novae and the Disc-instability Model

Dwarf novae (DNe) are CVs that are characterised by repeated periods of quiescence and dramatic outburst. One of the most famous DNe is SS Cyg, whose light curve is shown in figure 1.8. The repeated outbursts can be clearly seen, and SS Cyg itself has been undergoing this behaviour for the full century for which it has been observed. A spectrum over the course of a typical outburst is shown in figure 1.9, and is characterised by the appearance of an optically thick accretion disc continuum – note the similarity to the stellar atmosphere disc spectrum computed in section 1.1.2.1, and to the intermediate inclination nova-like variables discussed in the next section.

The leading scenario for explaining DN outbursts, and in fact also the outbursts in low mass X-ray binaries or ‘soft X-ray transients’, is the disc-instability model (DIM; [Osaki 1974](#); [Lasota 2001](#)). In this model, a gradual increase in supply rate from the donor star (and hence surface density in the disc) causes the disc to heat up. Eventually, the disc hits a critical temperature, around 7000 K, and becomes ionized. Now the surface density in the disc can increase significantly, and the disc becomes geometrically thin and optically thick. Most importantly, it can undergo efficient radiative cooling, and a significant increase in brightness is observed.

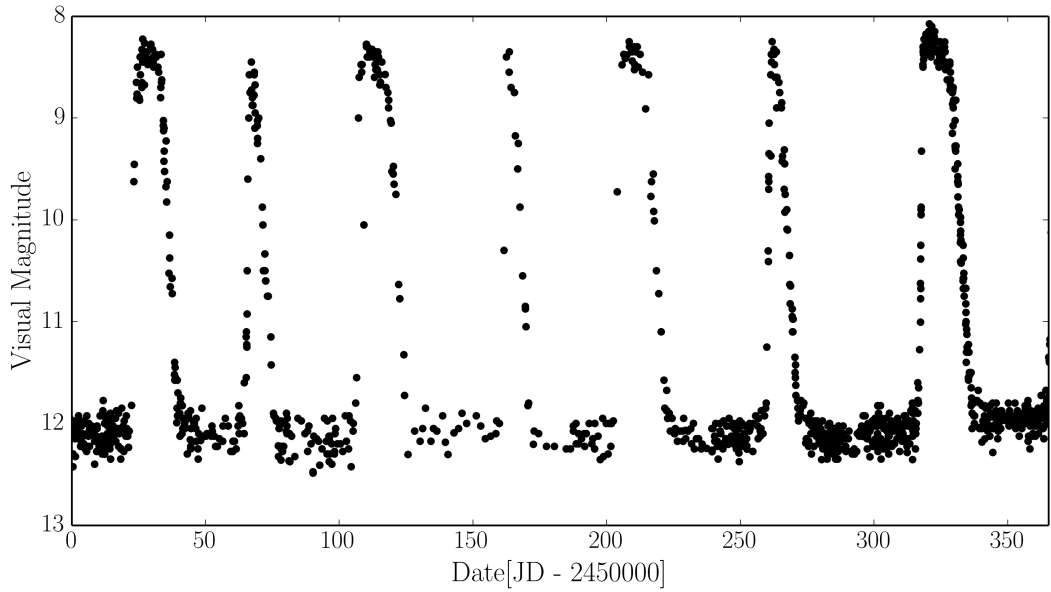


FIGURE 1.8: *Data: AAVSO.* A year in the life of SS Cyg, showing the characteristic repeated outbursts and periods of quiescence typical of a DN. SS Cyg has been undergoing this activity since it was first observed in 1896.

### 1.2.2.2 Nova-like Variables

Nova-like variables (NLs) are similar to DNe, except that the disc is always in a relatively high-accretion-rate state ( $\dot{M} \sim 10^{-8} M_{\odot} \text{ yr}^{-1}$ ). NLs are therefore one of the best ‘laboratories’ for testing the steady-state accretion disc theory described in section 1.1.2.1. In the optical, NLs generally exhibit a series of H and He emission lines superposed on a blue continuum. In many cases, and particularly in the SW Sex subclass of NLs (Honeycutt et al. 1986; Dhillon & Rutten 1995), these lines are single-peaked. This is contrary to theoretical expectations for lines formed in accretion discs, which are predicted to be double-peaked (Smak 1981; Horne & Marsh 1986). *Low-state* CVs (dwarf novae in quiescence) do, in fact, exhibit such double-peaked lines (Marsh & Horne 1990).

The UV spectra of NLs also show strong emission lines, and at low to intermediate inclinations dramatic blue-shifted absorption lines can be seen in some objects. The emission line equivalent widths in both the optical and the UV show clear correlations with inclination (Hessman et al. 1984; Echevarria 1988; Noebauer et al. 2010). This can be seen clearly in figure 1.11, and is connected to the correlation between line strength and absolute magnitude found by Patterson (1984); that is, the decrease in equivalent width at low inclination is caused by an *increase* in continuum flux. This is discussed further in chapters 4 and 6, but also has relevance to AGN and quasar unification

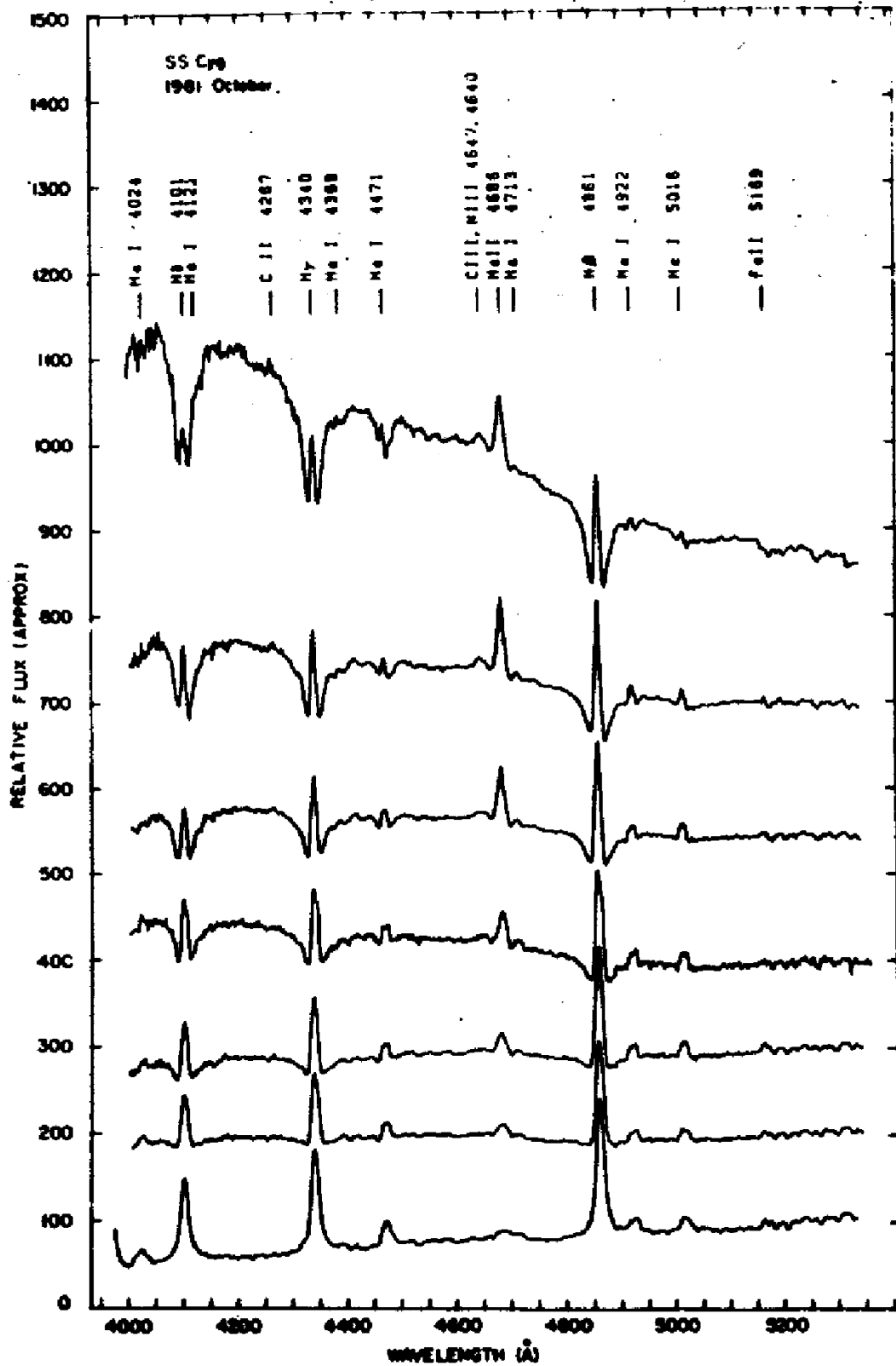


FIGURE 1.9: Credit: Hessman et al. 1984 / Dhillon et al. 1996. Spectra of SS Cyg during an outburst cycle, showing the evolution from minimum to maximum light. The rise is characterised by the appearance of an optically thick accretion disc spectrum. The flux scale is approximate.

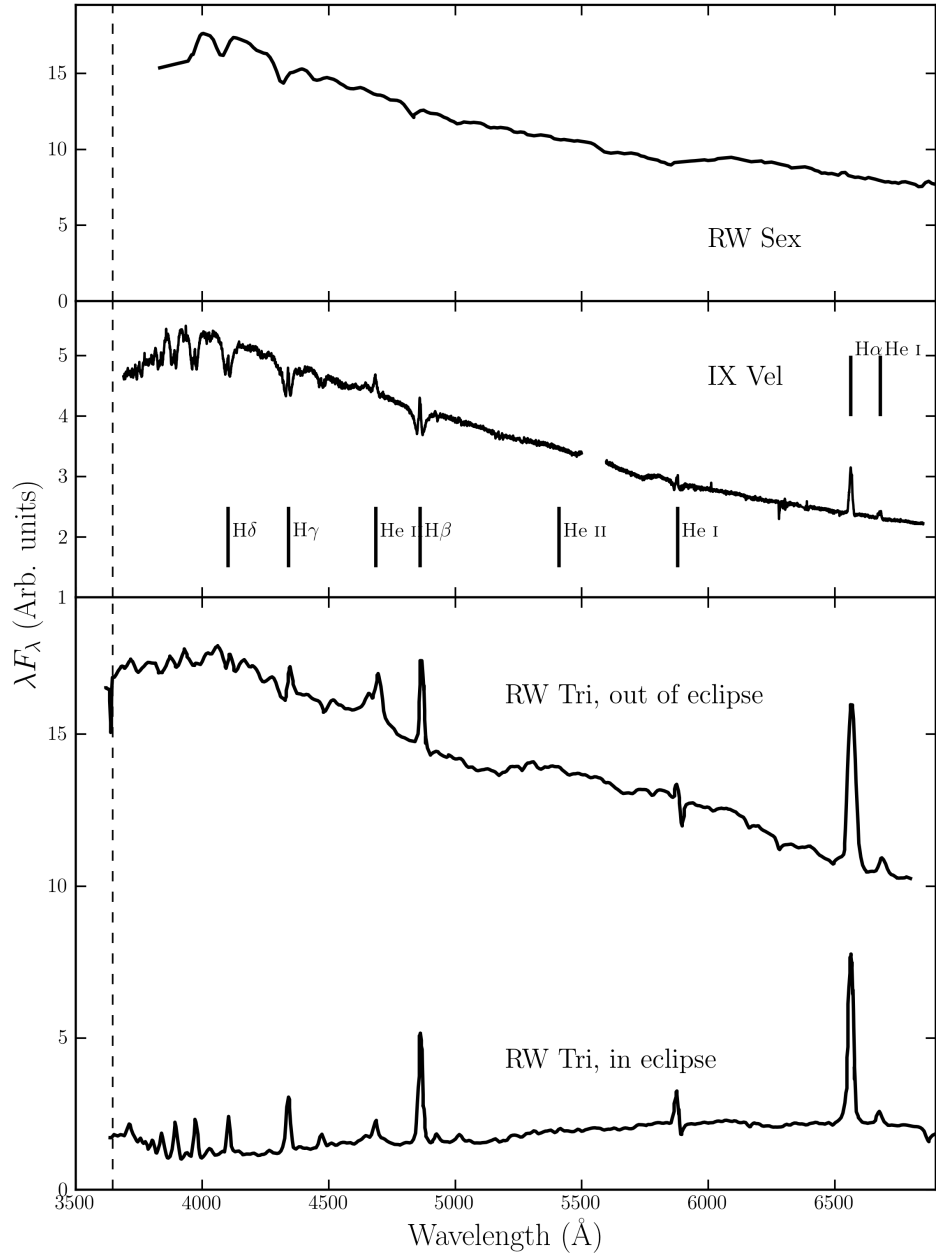


FIGURE 1.10: Optical spectra of three nova-like variables: RW Sex (top; Beuermann et al. 1992), IX Vel (top middle; A. F. Pala & B. T. Gaensicke, private communication) and RW Tri in and out of eclipse (bottom two panels; Groot et al. 2004). The data for RW Sex and RW Tri were digitized from the respective publications, and the IX Vel spectrum was obtained using the XSHOOTER spectrograph on the Very Large Telescope on 2014 October 10. These systems have approximate inclinations of  $30^\circ$ ,  $60^\circ$  and  $80^\circ$  respectively. The trend of increasing Balmer line emission with inclination can be seen. In RW Tri strong single-peaked emission in the Balmer lines is seen even in eclipse, indicating that the lines may be formed in a spatially extensive disc wind, and there is even a suggestion of a (potentially wind-formed) recombination continuum in the eclipsed spectrum. I have attempted to show each spectrum over a similar dynamic range.

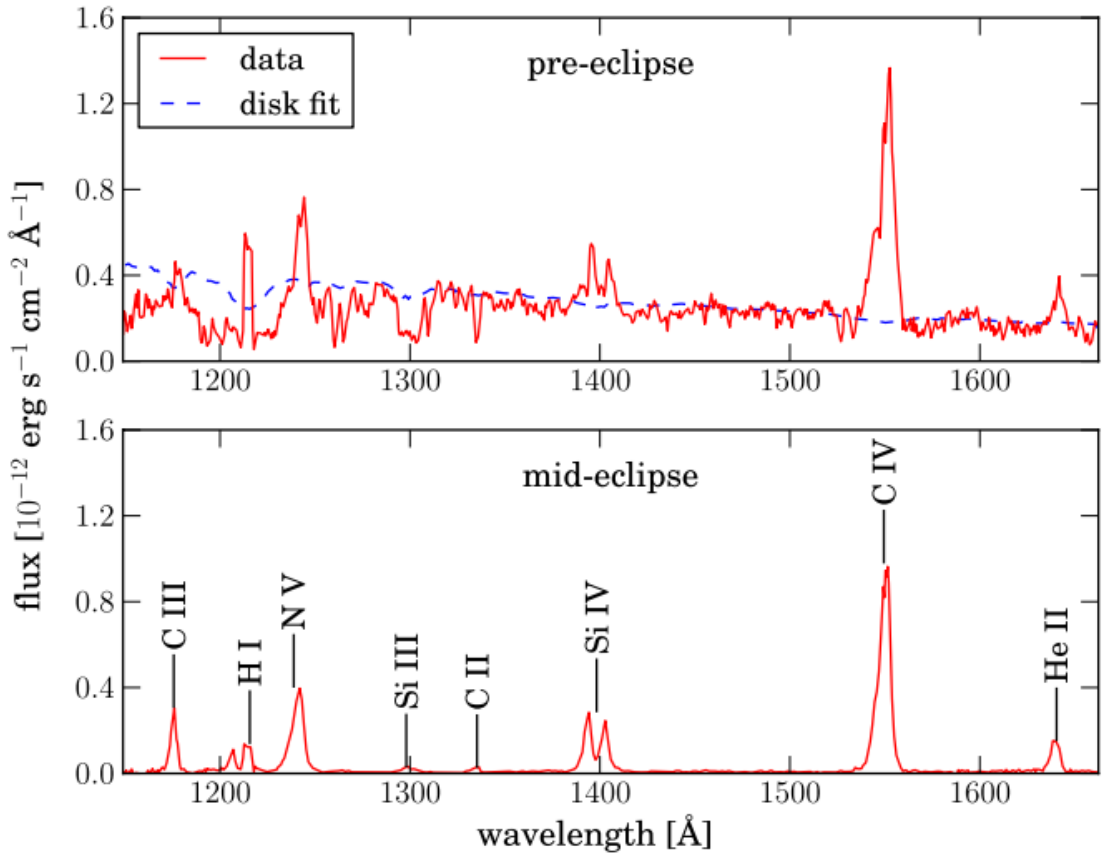


FIGURE 1.11: Credit: Noebauer et al. 2010. UV spectrum of RW Tri in and out of eclipse, showing strong lines in C IV  $\lambda$ 1550 and Ly $\alpha$ , among others.

schemes mentioned later in this introduction. The optical and UV spectra of NL CVs are discussed further in the context of winds in chapter 2.

### 1.2.3 Low Mass X-ray Binaries

Low-mass X-ray binaries (LMXBs) are similar to CVs in structure (see figure 1.6), but the compact object is either a neutron star (NS) or black hole (BH). The accretion disc emits in the soft X-ray regime, and an additional hard X-ray power law is also seen in the spectrum. This hard component is normally attributed to Compton up-scattering of seed disc photons by some kind of ‘corona’ of hot electrons close to the BH (e.g. White et al. 1988; Mitsuda et al. 1989; Uttley et al. 2014). Although I do not study LMXBs directly in this thesis, it is instructive to briefly discuss of their observational appearance as it is relevant to the links between accretion and outflow. The discovery that XRBs and CVs follow similar tracks on a hardness-intensity diagram (Körding et al. 2008) is particularly interesting in this regard, especially since Ponti et al. (2012) showed that

broad Fe absorption lines are only seen in the soft-state high-inclination systems (see section 2.1.2). This implies that equatorial outflows are intrinsic to the accretion process. Although the driving mechanism is probably different to CVs (e.g. [Díaz Trigo & Boirin 2015](#)), the similarity in general structure to models for CVs and quasars is striking.

### 1.3 Quasars and Active Galactic Nuclei

Spectra of AGN have now been studied for over 100 years, and we have known that they exhibit strong, broad emission lines since the first spectrum was taken by [Fath \(1909\)](#). However, it wasn't until the work of [Seyfert \(1943\)](#) that the systematic classification of AGN really began, leading to the phrase ‘Seyfert galaxy’. This label was applied to galaxies possessing a bright nucleus, spectroscopically characterised by a blue continuum and a series of strong emission lines. The first real physical insight into the extraordinary nature of AGN was provided by [Woltjer \(1959\)](#), who noted that (i) the nuclei must have sizes  $< 100$  pc, based on the fact that they were unresolved, and (ii) the mass of the nucleus must be very high, based on virial estimates. While both of these observations were based on simple arguments, the fact that these ultra-luminous celestial objects are both *compact* and *supermassive* is perhaps the defining insight into the nature of AGN.

Although the study of AGN was established in the optical waveband, radio astronomy also significantly furthered our understanding of AGN in the mid-20th century. A number of surveys, such as the Cambridge ([Edge et al. 1959](#)), Parkes ([Ekers 1969](#)) and Ohio ([Ehman et al. 1970](#)) surveys discovered a great many bright radio point sources distributed isotropically across the sky. These sources eventually became known as ‘quasi-stellar radio sources’, or *quasars*, and were soon found to be coincident with bright optical sources or ‘quasi-stellar objects’ (QSOs) at high redshifts ([Schmidt 1963, 1965a,b](#)). Nowadays, the term quasar normally has very little to do with radio emission and is often used interchangeably with QSO. Indeed, throughout this thesis I shall refer to a quasar as simply a bright, massive AGN; one with sufficiently high luminosity that it dominates the emission from its host galaxy.

One of the main classification schemes for AGN is a spectroscopic one, based on whether an object possesses broad emission lines in its spectrum, such as C IV broad H $\beta$  and Ly $\alpha$ , in addition to the narrow lines that are always present. If these broad lines are

seen, then the AGN is classed as type I; if not, it is classed as type II (figure 1.12). These designations were originally applied to Seyfert galaxies (Seyfert 1943), but can also be used to classify the more luminous quasar class, despite the apparent difficulty in finding the expected number of type II sources (Zakamska et al. 2003). This classification scheme is complicated somewhat by the existence of two unusual types of AGN: narrow line Seyfert Is (NLSIs), which may be explained by super-Eddington accretion (Done & Jin 2015) or perhaps simply an orientation effect (Baldi et al. 2016), and so-called ‘true type II’ AGN, in which the broad line region is absent (Tran 2001; Shi et al. 2010) rather than obscured (see next section). Despite this muddying of the waters, what was originally a clear dichotomy in spectral type provided a profound motivation for attempting to *unify* AGN via geometric arguments.

### 1.3.1 AGN Unification and the dusty Torus

Although Seyfert had identified type 1 and 2 AGN, a physical explanation for this dichotomy was not forthcoming until a study by (Antonucci & Miller 1985, AM85). They showed unambiguously that the nearby Seyfert 2 NGC 1068 is simply an obscured type 1 AGN, by finding that broad emission lines appeared in the spectrum of *polarised* flux. This provided the basis for the first successful attempt to unify AGN behaviour, as it elegantly explained the apparent disconnect between the two types of AGN as simply a viewing angle effect; at one angle, an observer could look directly into the broad line region (BLR) near the nucleus, but at Type 2 angles this region was hidden from view. The obscuring structure became known as the ‘torus’ (Krolik & Begelman 1986), due to its proposed geometry, and it was soon realised that this structure may be made of dust, in which case it could also be responsible for the infra-red (IR) bump in AGN (Neugebauer et al. 1979).

(Urry & Padovani 1995, UP95) went further than the original unification model proposed by AM85, as they also tried to account for the dichotomy in AGN radio properties (radio-loud/radio-quiet). The picture they proposed is shown in figure 1.13. This model attempts to explain all of the types of AGN merely as a function of viewing angle and presence, or absence, of a radio jet. Models such as this also describe the series of ‘bumps’ observed in AGN – the portions of the spectrum that dominate the luminosity, shown in figure 1.14. In most models, the ‘Big Blue Bump (BBB)’ is ascribed to thermal emission

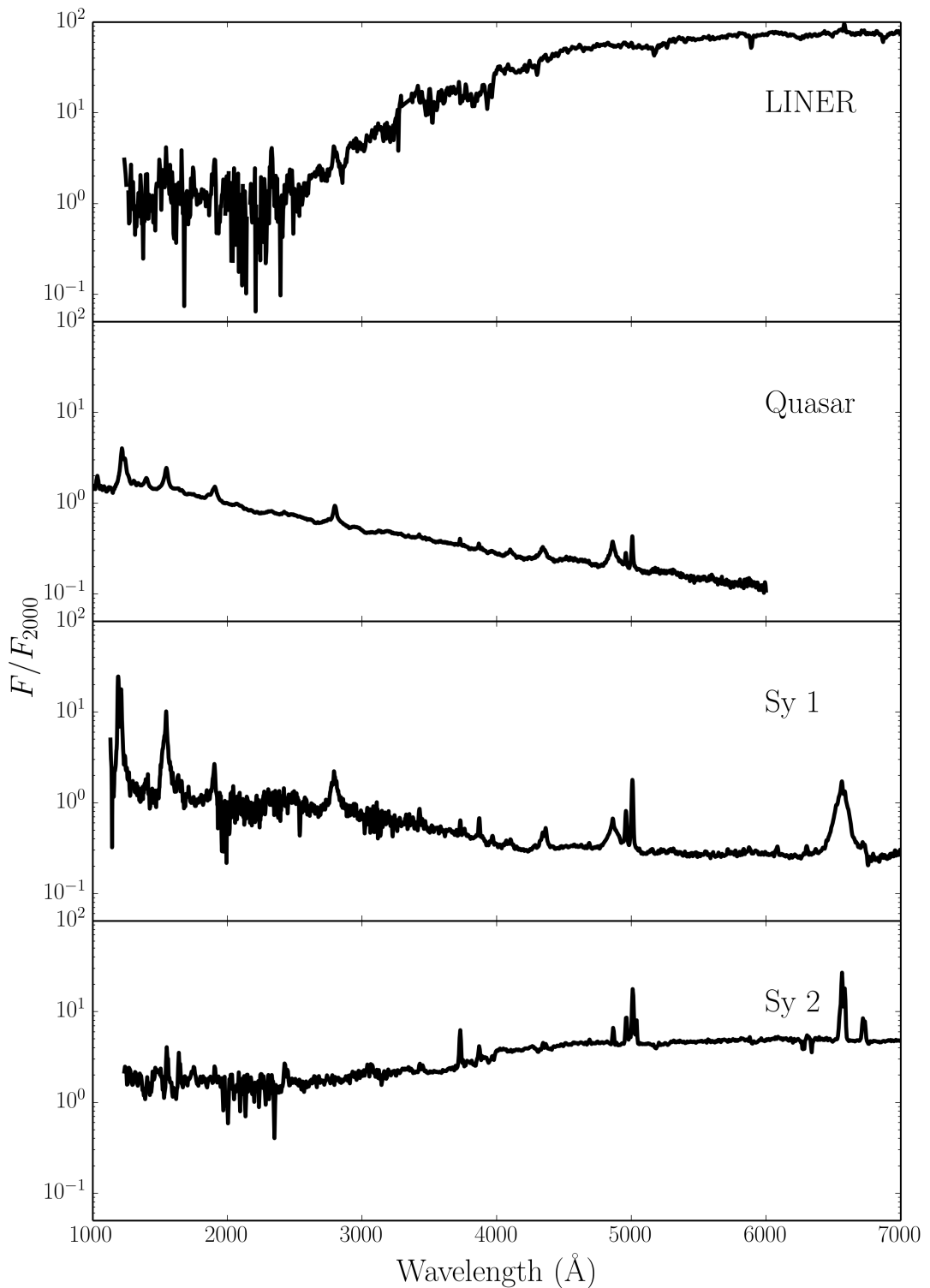


FIGURE 1.12: Template spectra, from the AGN atlas, for four common types of AGN.  
Obtained from [http://www.stsci.edu/hst/observatory/crds/cdbs\\_agn.html](http://www.stsci.edu/hst/observatory/crds/cdbs_agn.html).

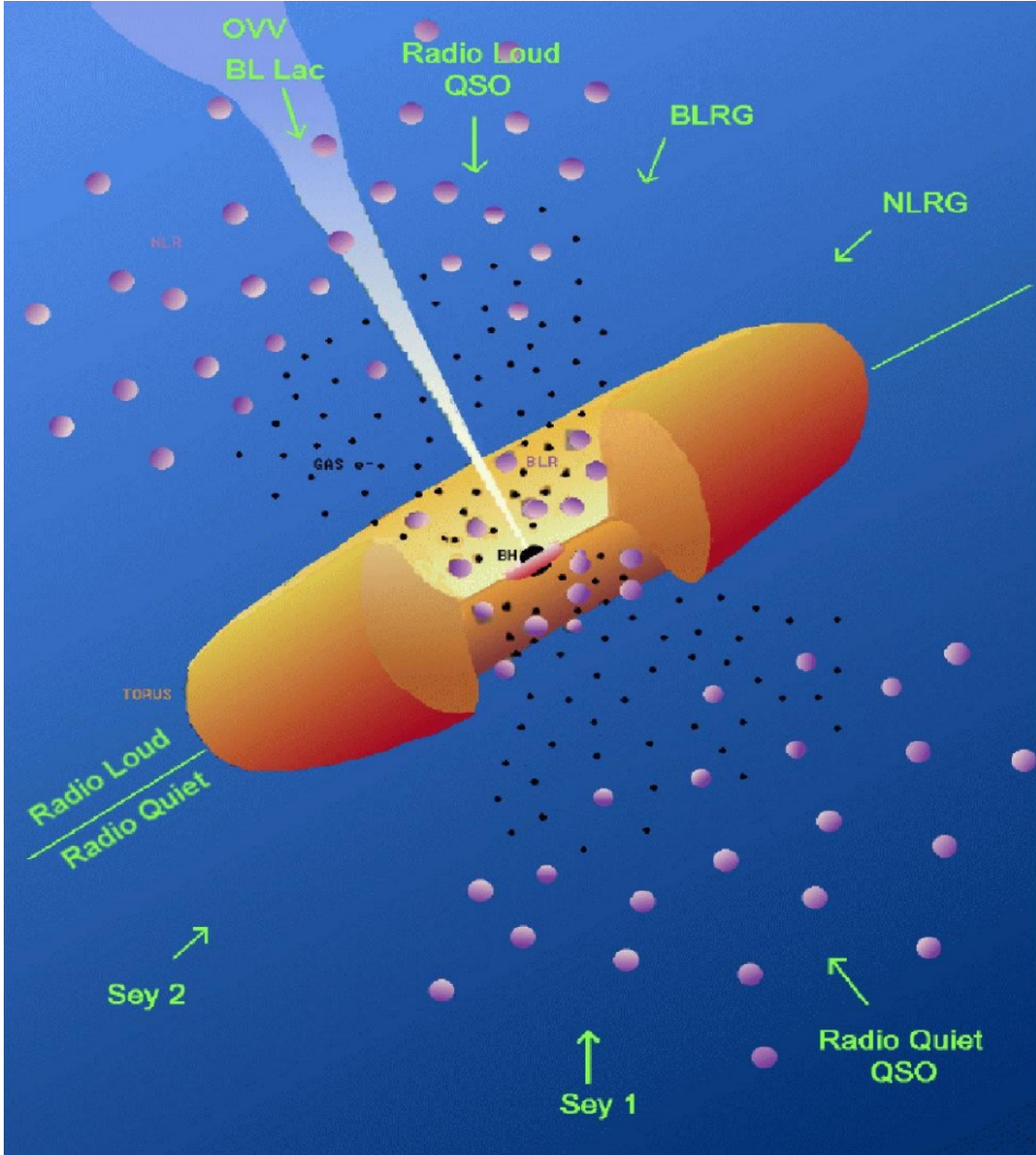


FIGURE 1.13: A unified scheme for AGN.

from an accretion disc, and the ‘Small Blue Bump’ to optically thin Balmer continuum and Fe II emission from the BLR. The latter can just be seen between  $\sim 2000\text{\AA}$  and  $\sim 4000\text{\AA}$  in the Seyfert 1 and quasar templates in figure 1.12. Our understanding of the BBB is still unsatisfactory (see section 1.4).

Since the seminal works by AM85 and UP95, the picture has become somewhat more complicated. Variable X-ray absorption has been detected in so-called ‘changing look’ AGN (Matt et al. 2003; Puccetti et al. 2007), including even NGC 1068 itself (Marinucci et al. 2016). Changes in type have also been seen in the optical lines; the broad

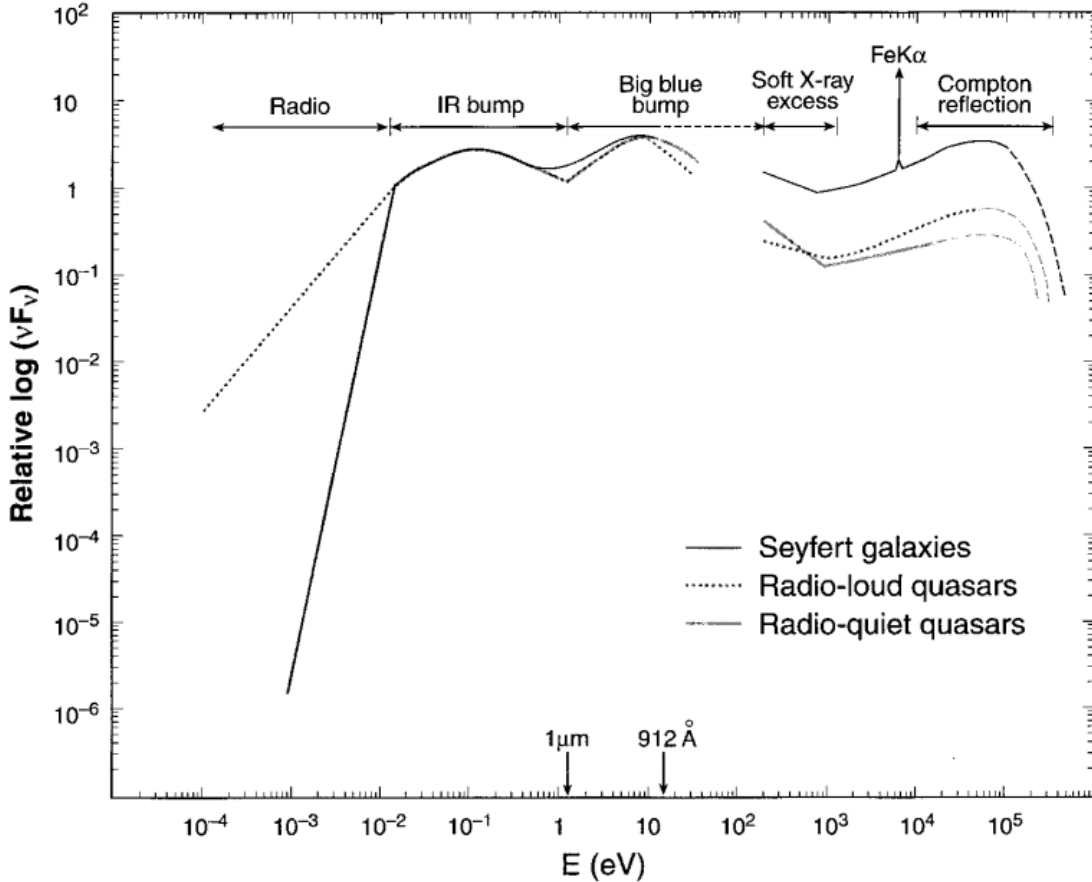


FIGURE 1.14: Credit: Koratkar & Blaes 1999 Approximate average broadband SEDs for a few types of AGN. The series of characteristic bumps can be clearly seen. The Soft-X-ray excess is also visible (see section 1.3.2.1).

$H\beta$  component in some AGN can dramatically disappear or reappear (e.g. Tohline & Osterbrock 1976; Cohen et al. 1986; Denney et al. 2014). The explanation for this could be variable absorption (Elitzur 2012) or a change in the accretion state of the disc. In the latter case, it has even been suggested that a disc wind could be directly responsible for this switch (Elitzur et al. 2014). Furthermore, dusty *polar* outflows have been found to be important IR emitters (Hönig et al. 2013), implying that, even when it comes to dust, the torus is not the whole picture. Despite these complications, the AGN torus unification picture still explains a lot of AGN phenomenology, and represents a useful framework that can be tested with observations.

### 1.3.2 X-ray Properties of AGN

Approximately 10% of the bolometric luminosity of AGN comes out in the X-ray band, between  $\sim 0.1$  and  $\sim 100$  keV. Thus, AGN dominate the cosmic X-ray background

(Madau et al. 1994). The hard X-ray emission typically follows a power law shape with spectral index -0.9 (e.g. Koratkar & Blaes 1999), widely considered, as in LMXBs, to come from a hot ‘corona’ of electrons close to the BH that upscatters disc seed photons (e.g. Haardt & Maraschi 1991). The compactness of this X-ray corona has been confirmed by microlensing (Chartas et al. 2009; Dai et al. 2010) and variability studies (Green et al. 1993; Crenshaw et al. 1996; Risaliti et al. 2007). Indeed, X-rays in AGN can be highly variable, both in terms of their intrinsic X-ray emission, but also due to changes in the absorption characteristics (Risaliti et al. 2002; Miller et al. 2008; Connolly et al. 2014). I discuss X-ray absorption in more detail, particularly with respect to disc winds, in chapter 2.

The hard X-ray spectra AGN also tend to exhibit a number of reflection features. Typically, these consist of a strong Fe K $\alpha$  emission line and a ‘Compton hump’ at high energies. The latter is produced by Compton down-scattering of high energy photons (Pounds et al. 1989; Nandra & Pounds 1994). It is still unclear exactly where these features originate, but a common interpretation is that they are caused by reflection off the inner parts of the accretion disc (Fabian et al. 1995; Iwasawa et al. 1996a; Reynolds 1999). If this is the case, and the broadening of the iron line is relativistic, this would allow for measurements of the BH spin (Laor 1991; Iwasawa et al. 1996b; Dabrowski et al. 1997). This hypothesis is somewhat controversial. Multiple authors have found that many of the relativistic features supposedly imprinted by BH spin can in fact be explained by Comptonisation or absorption (e.g. Misra & Kembhavi 1998; Miller & Turner 2013), and radiative transfer modelling has shown that an outflow can naturally produce the characteristic broad red Fe K $\alpha$  wing (Sim et al. 2010a).

In Compton-thick AGN, the intrinsic continuum is heavily absorbed with columns of  $N_H \sim 10^{24}$  cm $^{-2}$  – this absorption is normally attributed to the dusty torus, but disc winds could also contribute. Compton-thick AGN are required in large numbers in order to explain the cosmic X-ray background (Setti & Woltjer 1989). In these sources, reflection features can actually dominate the X-ray spectrum (Alexander et al. 2011; Gandhi et al. 2013), but the Fe line is formed from low ionization stages of Fe on  $\sim 0.1$  pc scales (Gandhi et al. 2015).

### 1.3.2.1 The Soft X-ray Excess

If one interpolates between the  $\nu^{1/3}$  law from the BBB in the UV, and the power law in the hard X-rays, a curious excess of flux is often found in type 1 AGN (see figure 1.14, and Koratkar & Blaes 1999). This is known as the soft X-ray excess (SXSS), which is too hot to be explained by thermal disc emission, as a thin disc around an AGN should never approach the temperatures required. Many models have been proposed to explain this excess, including relativistically smeared photoabsorption (Gierliński & Done 2004, 2006), relativistically smeared line and free-free emission (Ross & Fabian 2005) and a variety of cool Comptonised component geometries such as an inner accretion flow (Magdziarz et al. 1998; Done et al. 2012) and thin layer on top of the disc (Janiuk et al. 2001). While the SXSS poses a challenge to the simplest pictures of AGN, it may also solve some of the issues, as some of the geometries proposed may help to explain the accretion disc size problem discussed in section 1.4 (Gardner & Done 2016).

### 1.3.3 The Broad Line Region: Connection to winds and unification

In the UP95 unification model, the broad emission lines come from a series of virialised clouds close to the disc plane. As noted by (Murray et al. 1995, hereafter MCGV95), there are a number of problems with the BLR ‘cloud’ model, perhaps most notably that there is no obvious physical origin for such virialised clouds. Testing alternative models for the BLR is therefore important. Indeed, MCGV95 proposed a disc wind model in order to explain both BALs and BELs in quasars. A disc wind model was also discussed by Elvis (2000), who proposed a structure for quasars that attempted to explain much of the behaviour of luminous AGN merely as a function of viewing angle. Outflow models are discussed further in section 2. The philosophy of these models is that, before invoking additional degrees of freedom in a model, we should first test if known quasar phenomenology (disc winds) can explain other aspects of their observational appearance. I have illustrated this general principle with the ‘Occam’s quasar’ cartoon shown in figure 1.15. This is the picture that I will quantitatively test in the latter, quasar-focused sections of this thesis. The same general principle can also be applied to cataclysmic variables and other accreting objects.

OCCAM'S QUASAR: THE PRINCIPLE THAT IN EXPLAINING A QUASAR NO MORE ASSUMPTIONS SHOULD BE MADE THAN ARE NECESSARY.

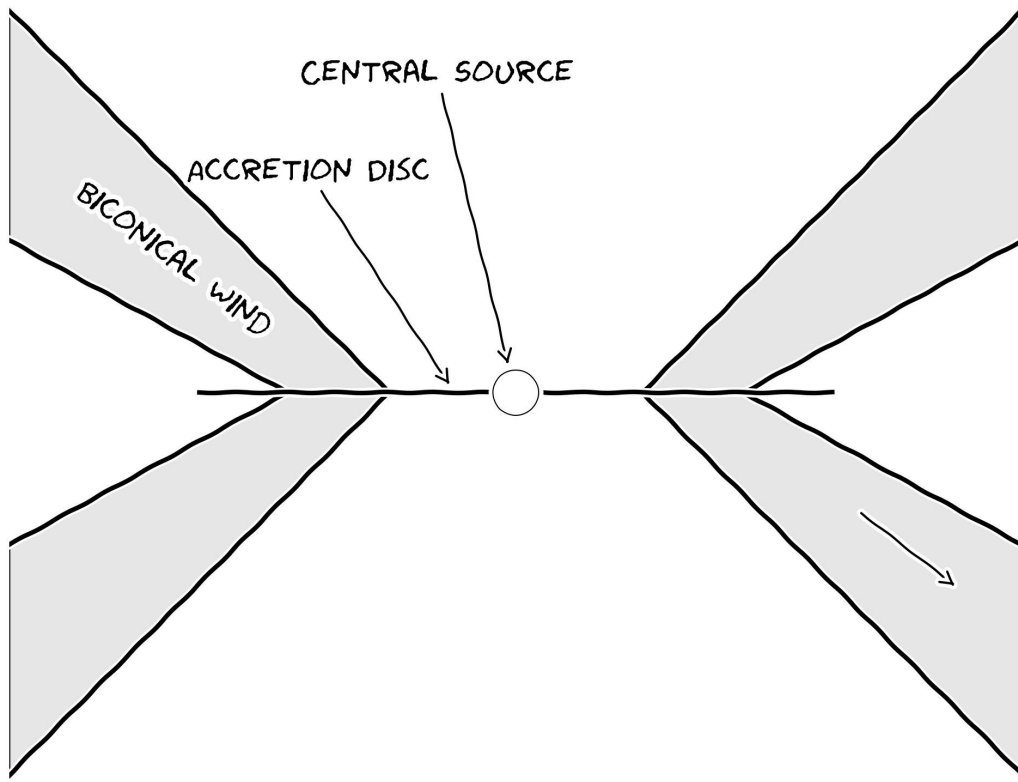


FIGURE 1.15: Occam's quasar. How far can this general picture take us when trying to explain the behaviour of quasars and other accreting compact objects?

## 1.4 The Current Understanding of the Disc Continuum

The SS73 model is still the most common way to fit accretion disc spectra and infer information about the underlying physics. However, a number of issues have been raised with the thin-disc model and its applicability to accreting systems.

### 1.4.1 The Spectral shape of CV discs

Attempts to fit the observed SEDs of high-state CVs with simple disc models have met with mixed success. In particular, the SEDs predicted by most stellar/disc atmosphere models are too blue in the UV (Wade 1988; Long et al. 1991, 1994; Knigge et al. 1998a) and exhibit stronger-than-observed Balmer jumps in absorption (Wade 1984; Haug 1987; La Dous 1989; Knigge et al. 1998a). One possible explanation for these problems is that

these models fail to capture all of the relevant physics. Indeed, it has been argued that a self-consistent treatment can produce better agreement with observational data (e.g. Shaviv et al. 1991; but see also Idan et al. 2010). However, an alternative explanation, suggested by Knigge et al. (1998b; see also Hassall et al. 1985), is that recombination continuum emission from the base of the disc wind might fill in the disc’s Balmer absorption edge and flatten the UV spectrum.

Alternatively, it may just be that CV disks are never really in a steady state, and so we should only expect the  $R^{-3/4}$  temperature profile to hold in a limited portion of the disc. From eclipse mapping, it has been shown that the inferred accretion rate increases with radius in NLs (Rutten et al. 1992; Horne 1993). These results suggest that a non-radiative form of energy loss is present in the inner regions of the disc, of which potential forms would be advection or mass loss. This is yet another piece of evidence that the understanding of accretion and outflow are intertwined, although hopefully not inextricably.

### 1.4.2 The Big Blue Bump in AGN

Does the SS73 model apply well to AGN spectra? There are contrasting views on the matter. On the one hand, Antonucci (2013) claims that “most of the AGN community is mesmerized by unphysical models that have no predictive power”. Yet a recent spectral fitting study by Capellupo et al. (2015) concludes that “altogether, these results indicate that thin ADs are indeed the main power houses of AGN”. So, what are the current problems when confronting thin disc models with observation?

#### 1.4.2.1 The Accretion Disc Size Problem

One of the most interesting results of recent years relating to AGN and accretion discs is the discovery that the continuum emission region size appears to be a factor  $\sim 3$  larger than predicted by standard thin disc theory. This result has been found independently in both microlensing (Morgan et al. 2010; Dai et al. 2010) and reverberation (Edelson et al. 2015) studies, and poses a challenge to the current best-bet model for the big blue bump in AGN. One proposed solution is that the discs in AGN are inhomogenous, consisting of individual clumps with independently varying temperatures (Dexter & Agol 2011),

but this is very much still an active area of research. It is worth noting that the impact of winds on these results has not yet been properly quantified, something our team is currently trying to address ([Mangham et al. 2016](#)).

#### 1.4.2.2 Fitting AGN Spectra and the 1000Å Break

One of the *successes* of the thin disc model, when applied to AGN, is that we do observe a slope in the UV of  $\alpha_{UV} = 0.32$ , confirming the theoretical prediction of  $\nu^{1/3}$ . However, AGN spectra do not exhibit the *overall* spectral shape (e.g. [Davis et al. 2007](#); [Shankar et al. 2016](#)) or colour-mass scalings ([Bonning et al. 2007](#)) expected from theoretical predictions. This can be seen clearly in figure 1.12, where both the quasar and Seyfert spectra tend to peak in the UV, rather than the EUV. Furthermore, there is a characteristic break in AGN spectra at around 1000 Å ([Lusso et al. 2015](#)), which does not scale with BH mass or luminosity, as one might expect for a break associated with an accretion disc. There is also no evidence in AGN of the expected polarisation signatures from an optically thick disc atmosphere ([Stockman et al. 1979](#); [Antonucci 1988](#); [Antonucci et al. 1996](#)).

Despite these problems, recent work suggests that the thin disc model still has some potential. [Capellupo et al. \(2015\)](#) were able to fit a number of AGN spectra in the UV and optical with thin disc models, although successful fits were only found once they included effects such as Comptonisation and mass-loss, as well as correcting for extinction. BH spin also had a reasonable effect on the spectral fits, although it is somewhat difficult to constrain from spectral fitting alone. The 1000 Å break has also been explained with a mass-losing disc ([Laor & Davis 2014](#)), and [Lusso et al. \(2015\)](#) suggested that incorrect IGM corrections may be exacerbating the effect. So, while many problems exist, it may not quite be time to abandon the Shakura-Sunyaev ship just yet.

## 1.5 The Universality of Accretion

Accretion appears to be an important physical processes across  $\sim 10$  orders of magnitude in mass. But is this process the same on all scales? Does any behaviour manifest in all accreting systems?

### 1.5.1 The RMS-flux relation

Broad-band variability is common in all types of accretion disc. It has been known for some time that there exists a linear relationship between the flux and absolute root-mean-square (rms) amplitude of this variability. This was discovered first in XRBs and AGN (Uttley & McHardy 2001; Uttley et al. 2005; Heil et al. 2012), but it has been shown more recently that the relationship extends to CVs and even YSOs (Scaringi et al. 2012, 2015). The relationship is also not limited to just one type of CV but is present in both NLs and DNe (Van de Sande et al. 2015).

The model that best reproduces this behaviour is the so-called ‘fluctuating accretion disc’ model (Lyubarskii 1997; Kotov et al. 2001; Arévalo & Uttley 2006; Hogg & Reynolds 2015). More generally, additive processes cannot reproduce this behaviour, and a multiplicative mechanism is required (Uttley et al. 2005). Regardless of the mechanism, the rms-flux relation is one of the most clear-cut examples of a universal accretion phenomenon. It tells us that at least some of the behaviour in CV discs is also present in AGN and XRBs, strengthening the argument that CVs can be used as ‘accretion laboratories’.

### 1.5.2 Accretion states and disc-jet coupling

Variable and transient sources are common in astrophysics, particularly when the sources are accreting. I have already mentioned the DIM and its applicability to LMXBs and CVs; it turns out that when one plots the colour and luminosity evolution over the course of an outburst cycle then they follow very similar tracks [see figure 1.16, kordingDNjet2008]. The detection of radio jets is also intrinsically linked to the accretion state of the system (disc-jet coupling), as jets only appear in the ‘hard’ accretion state, to the right of the so-called ‘jet line’ (Fender 2001; Fender et al. 2004). Körding et al. (2008) showed that this behaviour also occurs in CVs, as radio emission in the DSS Cyg is also detected in the same region of colour-luminosity space. There is also a well-known correlation between radio and X-ray luminosities in low-hard states (Gallo et al. 2003).

This clear correlation with accretion state on HIDs has natural parallels with AGN.

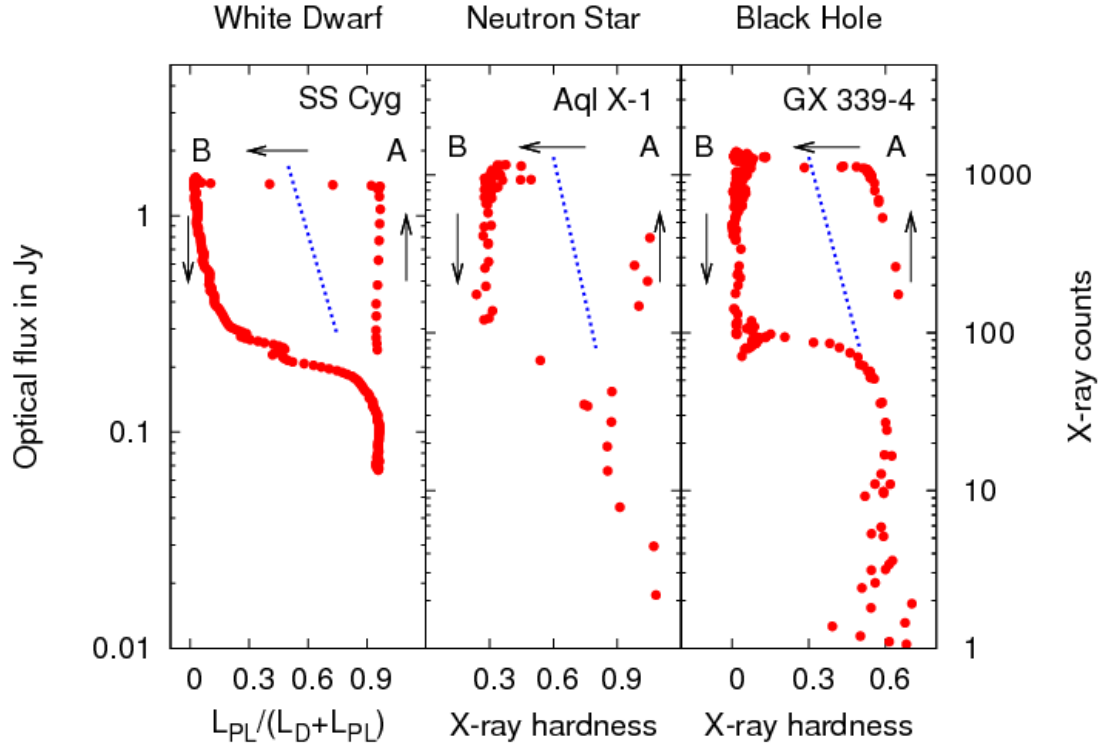


FIGURE 1.16: Credit: Kording et al. 2008. Caption.

The jet production mechanism in BHs in general is not well known. Theoretical work suggests that radio jets should be correlated with BH spin ([Penrose & Floyd 1971](#); [Blandford & Znajek 1977](#)), but whether such a correlation exists in LMXBs is controversial ([Fender et al. 2010](#); [Narayan & McClintock 2012](#)). This has significant implications for AGN; if powerful radio jets are associated exclusively with rotating BHs then the number of radio-loud AGN would imply a large fraction of them must be rapidly spinning, with high radiative efficiencies. Further evidence that radio jets are not simply produced by RIAFs onto spinning BHs is found when one considers that NLs show evidence of synchrotron radio emission ([Coppejans et al. 2015](#)). This important result suggests that our understanding of jets is incomplete, and that the links between accretion state and jet production are fundamental, but unsolved. Disc winds may complicate, or simplify, matters, depending on one's outlook (see chapter 2).

### 1.5.3 A Global Picture

Clearly, accretion physics is relevant to a plethora of astrophysical phenomena, and at least some of the physics of accretion is applicable to *all* classes of accreting object.

It would also appear that the outflowing material observed in accreting systems has a profound effect on the accretion process itself, and possibly significantly affects the observational appearance of disc-accreting systems (c.f. Elvis unification model). Hence, in the next chapter, I will review the evidence for winds and discuss some of the relevant background theory.

# Chapter 2

## Accretion Disc Winds

“A view of space, with an elephant  
obstructing it”

*Mike Vennart, Silent/Transparent*

### 2.1 Observational Evidence

The observational evidence for mass-loaded outflows or winds is widespread across the entire astrophysical mass range and most of the electromagnetic spectrum. Before detailing the more compelling aspects of this evidence, it is pertinent to briefly discuss the ‘smoking gun’ used to unambiguously detect winds – the presence of blue shifted BALs or ‘P-Cygni’ profiles in an objects spectrum.

Figure 2.1 shows how a spherical outflow of significant opacity will cause these characteristic line profile shapes to form, as scattering out of the line of sight causes a dip in the blue wing of the line, while scattering into the line of sight from other portions of the outflow causes an increase in flux in the red wing of the line. The situation is much more complex in most astrophysical situations; for example, the geometry is rarely spherically symmetric, and the line is rarely a pure scattering case. Indeed, the potential for complicated radiative transfer effects and variety in line formation mechanisms is one of the reasons why 3D Monte Carlo radiative transfer simulations are necessary to effectively model disc winds (see section 3).

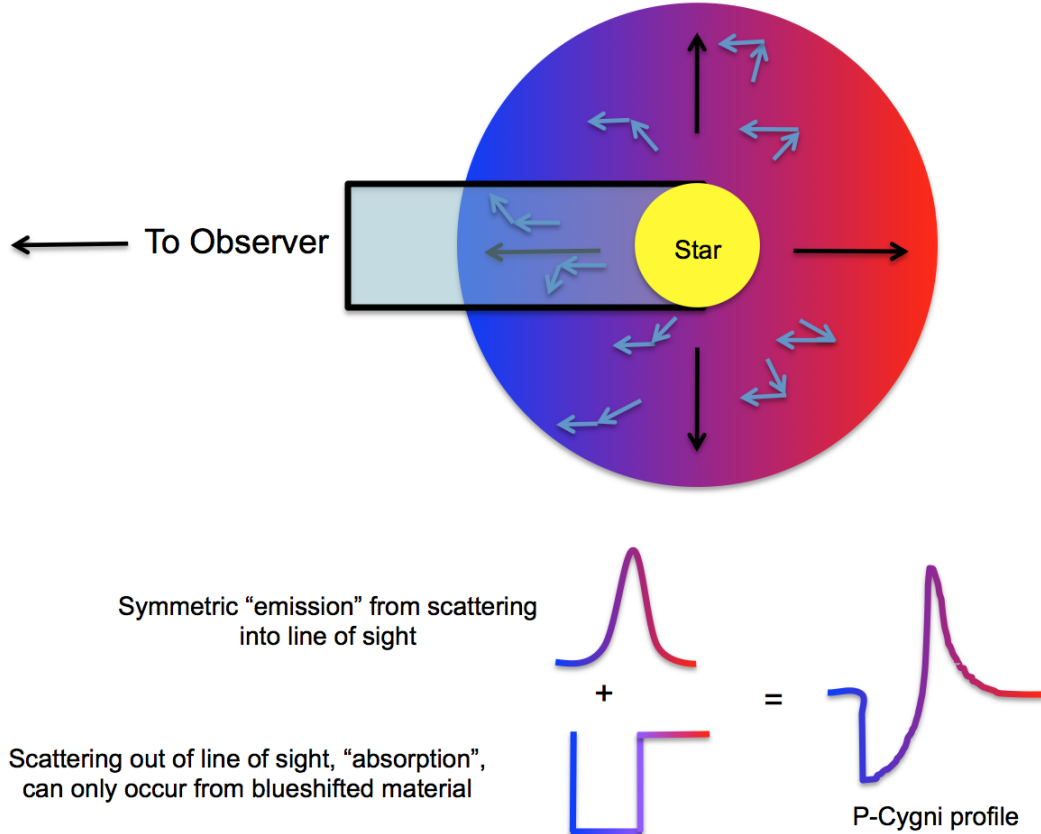


FIGURE 2.1: Diagram showing how an expanding envelope or wind with significant line opacity around a continuum source leads to the formation of P-Cygni profiles. The black arrows denote the outflow direction and the blue arrows typical scattering interactions.

### 2.1.1 Cataclysmic Variables

It has been known for a long time that winds emanating from the accretion disc are important in shaping the ultraviolet (UV) spectra of high-state CVs (Heap et al. 1978; Greenstein & Oke 1982). The most spectacular evidence for such outflows are the P-Cygni-like profiles seen in UV resonance lines such as C IV  $\lambda 1550$  (Cordova & Mason 1982, see Fig. 2.2)). Considerable effort has been spent over the years on understanding and modelling these UV features (e.g. Drew & Verbunt 1985; Mauche & Raymond 1987; Shlosman & Vitello 1993; Knigge et al. 1995; Knigge & Drew 1997; Knigge et al. 1997; Long & Knigge 2002; Noebauer et al. 2010; Puebla et al. 2011). The basic picture emerging from these efforts is of a slowly accelerating, moderately collimated bipolar outflow that carries away  $\simeq 1\% - 10\%$  of the accreting material. State-of-the-art simulations of line formation in this type of disc wind can produce UV line profiles that are remarkably similar to observations, as shown in Fig. 2.3.

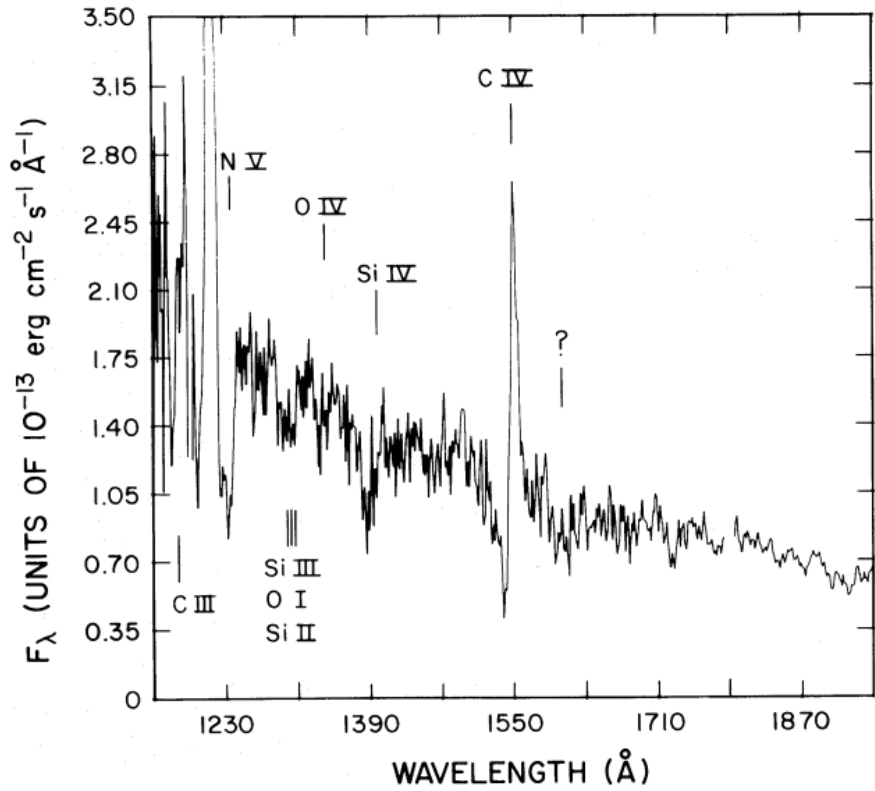


FIGURE 2.2: Credit: Cordova & Mason 1982. UV spectrum of the DN TW Vir during outburst. The P-Cygni profiles can be seen clearly, demonstrating that a strong, fast outflow is present in the system.

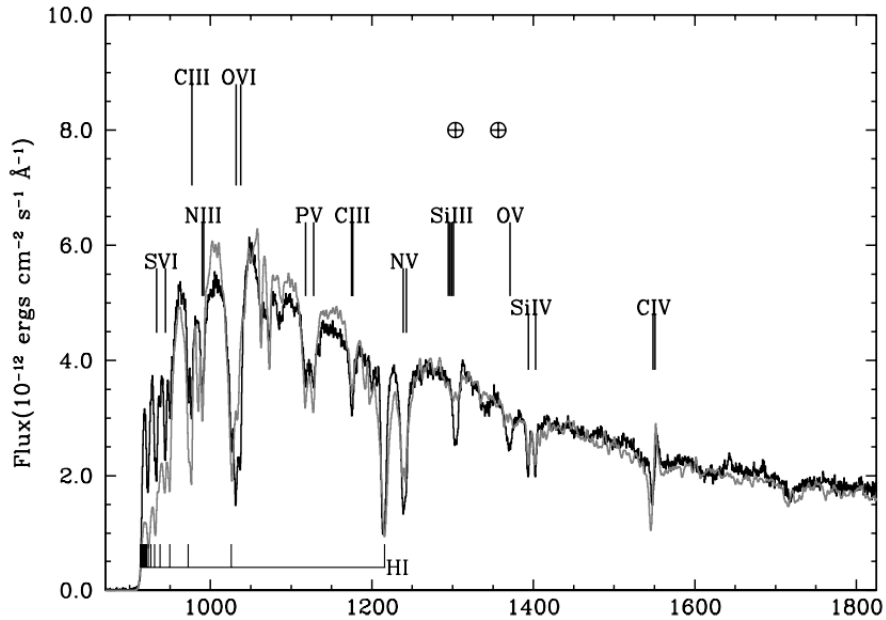


FIGURE 2.3: Credit: Long & Knigge 2002. UV spectrum of Z Cam, compared to a synthetic spectrum from MCRT simulations.

Much less is known about the effect of these outflows on the optical spectra of high-state CVs. Direct evidence of wind-formed lines comes from isolated observations of P-Cygni-like line profiles in H $\alpha$  and He I  $\lambda$ 5876, (Patterson et al. 1996; Ringwald & Naylor 1998; Kafka & Honeycutt 2004). However, the effect on the *emission* aspects of the optical spectrum is not well known. Murray & Chiang (1996, 1997) have shown that the presence of disc winds may offer a natural explanation for the single-peaked optical emission lines in high-state CVs, since they can strongly affect the radiative transfer of line photons (see Fig. ??). Stronger support for a significant wind contribution to the optical emission lines comes from observations of eclipsing systems. There, the single-peaked lines are often only weakly eclipsed, and a significant fraction of the line flux remains visible even near mid-eclipse (e.g. Baptista et al. 2000; Groot et al. 2004). This points to line formation in a spatially extended region, such as a disc wind (see section ??). It is also possible that a wind may affect the continuum emission of CVs, as described in section ???. The effect of an accretion disc wind on the optical line and continuum emission of CVs is addressed directly, via radiative transfer modelling, in chapter 4.

### 2.1.2 X-ray Binaries

Like CVs, evidence for fast outflows in LMXBs is not constrained to a single waveband. UV absorption in outflows was detected when Ioannou et al. (2003) observed C IV  $\lambda$ 1550 P-Cygni profiles with blueshifts of  $\sim 1500 \text{ km s}^{-1}$ . Shortly after, a series of papers found highly ionized Fe absorption with similar blueshifts and FWHM of around  $1500 \text{ km s}^{-1}$  (REFs). These absorption features tended to be detected in high-inclination, ‘dipping’ LMXBs, and this was confirmed in more sources by Ponti et al. (2012), who proposed an equatorial geometry based on this (see Fig. 2.4). The same study demonstrated (Fig. 2.5) that the winds only appeared in the soft, disc dominated accretion state, on the opposite side of the HID to the region where jets are common. This exciting result demonstrated how important winds are to our understanding of accretion, and required that we expand the discussion of accretion states from ‘disc-jet’ coupling to also include winds.

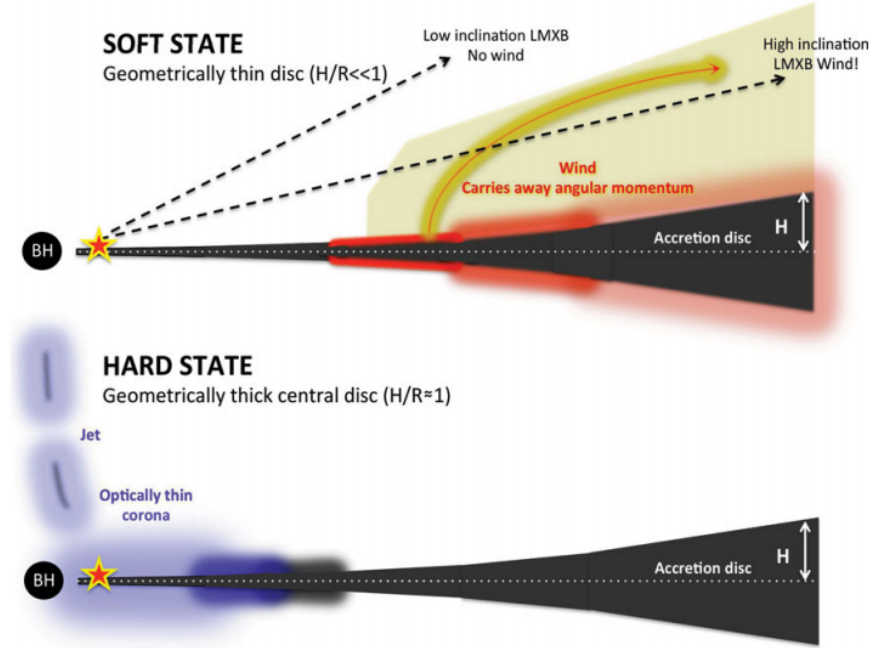


FIGURE 2.4: Credit: Ponti et al. 2012. A cartoon illustrating the expected geometry of soft-state LMXB winds.

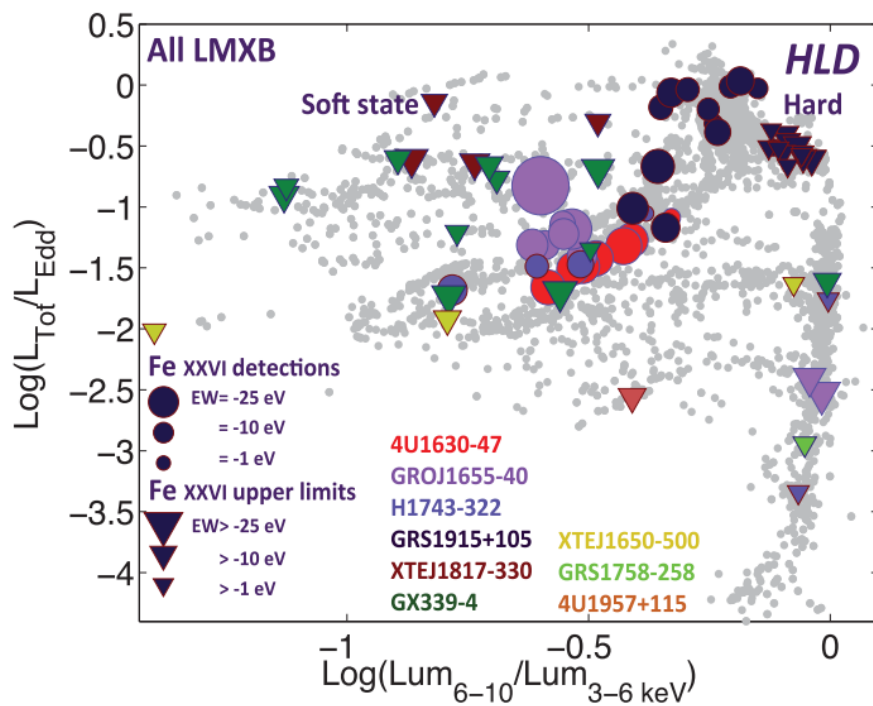


FIGURE 2.5: Credit: Ponti et al. 2012. Hardness-intensity diagram for four dipping LMXBs, demonstrating that winds appear only in the soft state.

### 2.1.3 AGN and Quasars

#### 2.1.3.1 Broad Absorption Line Quasars

Perhaps the clearest evidence of outflows in AGN is the blueshifted ( $\sim 0.1 c$ ) broad absorption lines (BALs) in the ultraviolet seen in approximately 20 – 40% of quasars (Weymann et al. 1991; Knigge et al. 2008; Dai et al. 2008; Allen et al. 2011). Five example spectra of BAL quasars from the HST and SDSS archives are shown in Fig. 2.6. In addition to the most common high-ionization BAL quasars (HiBALs), approximately 10% of BALQSOs show absorption in lower ionization species such as Mg II and Al III (LoBALs; Voit et al. 1993; Gibson et al. 2009) and an even smaller subset also show absorption in Fe II and III (FeLoBALs; Becker et al. 2000; Hall et al. 2002).

The simplest explanation for the incidence of BAL quasars (BALQSOs) is in terms of an accretion disc wind viewed from different angles. This principle of geometric unification is very similar to the idea behind the UP95 and AM95 models discussed in Chapter 1. According to this paradigm, a biconical wind rises from the accretion disc and the BALQSO fraction is associated with the covering factor of the outflow. This fraction has been estimated by various authors using different selection criteria, with values ranging between 10 and 40% depending on corrections and the classification scheme used (Weymann et al. 1991; Trump et al. 2006; Knigge et al. 2008; Dai et al. 2008; Allen et al. 2011)

BAL quasars can also be interpreted in an *evolutionary* context, in which quasars spend a certain proportion of their life in the ‘BAL phase’. Models generally put this phase near the start of the quasar lifetime (Hazard et al. 1984; Surdej & Hutsemekers 1987; Boroson & Meyers 1992; Zubovas & King 2013), after a dust-enshrouded phase but before the main quasar period. It is perhaps more likely that *both* evolutionary and geometric effects are at work (Borguet & Hutsemékers 2010; Dai et al. 2012). One of the main problems with testing these two paradigms is that many of the properties of BAL quasars fit naturally into either picture, and so disentangling their true nature is challenging. The latter chapters of this thesis attempt to address this issue by testing the geometric unification model, or ‘Occam’s quasar’ (see Chapter 1), and establishing how close this simple picture can get to explaining the BAL phenomenon.

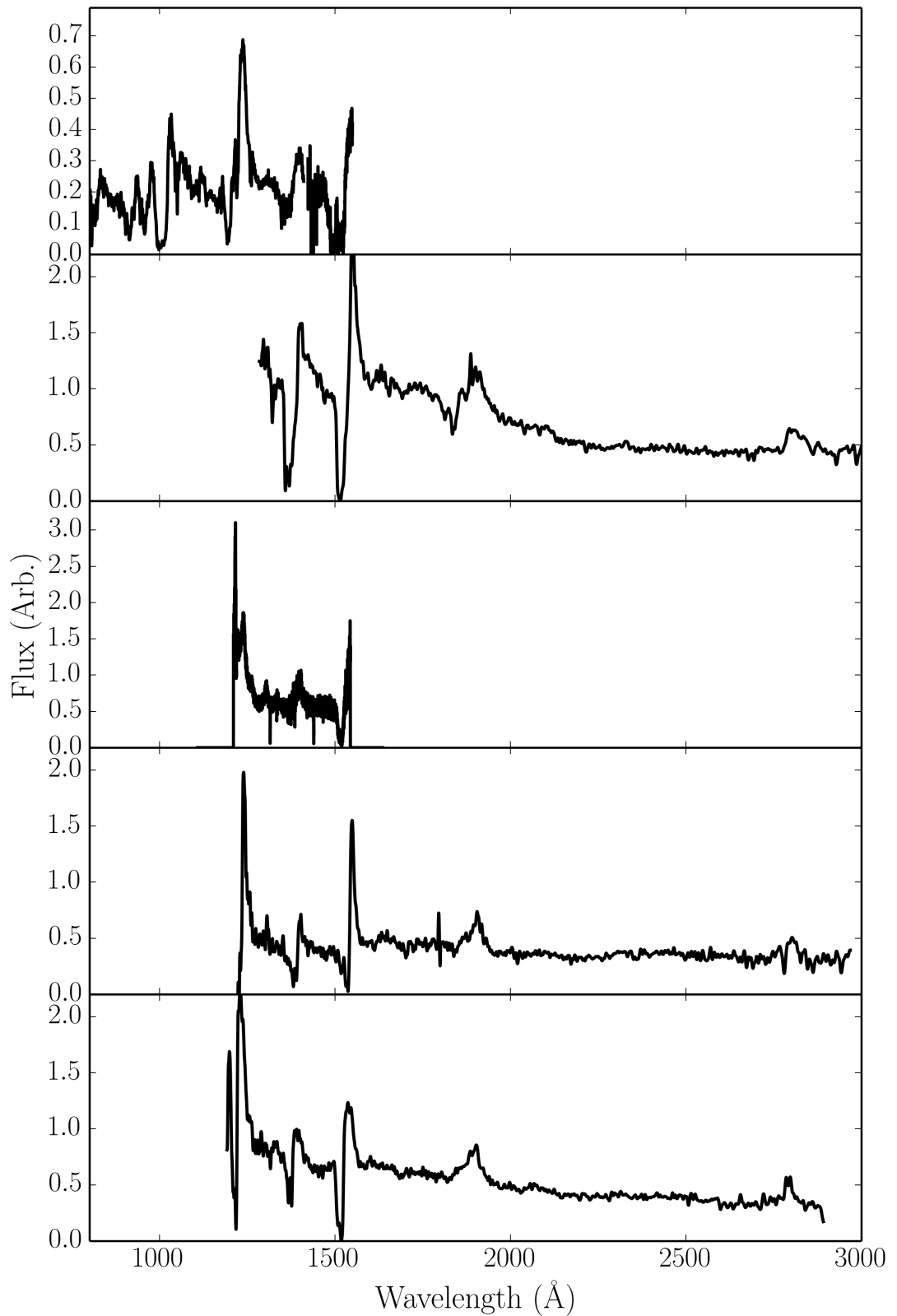


FIGURE 2.6: Five examples of BAL quasar spectra, from HST and SDSS.

While the BAL fraction,  $f_{BAL}$ , is a very useful number and must be at least related to the covering factor of the outflow, continuum selection effects (Goodrich 1997; Krolik & Voit 1998), as well as reddening (Allen et al. 2011), could significantly alter the true value of  $f_{BAL}$ . The degree of collimation of the BAL wind is also not well known. Polarisation studies suggest that the wind is roughly equatorial (Goodrich & Miller 1995; Cohen et al. 1995), as also found from hydrodynamical and radiative transfer simulations (Proga et al. 2000; Proga & Kallman 2004; Higginbottom et al. 2013), but there is also evidence for polar BAL outflows in radio-loud (RL) sources (Zhou et al. 2006; Ghosh & Punsly 2007). In addition to these uncertainties, the physical scale of the BAL phenomenon is also disputed, and may vary from object to object. If one assumes that the BAL region is on the same scale as the BLR then the radius of the absorbing material can be estimated as  $\sim 100 - 1000r_G$  from reverberation mapping and microlensing (e.g., for BLRs in BALQSOs, Sluse et al. 2015; O'Dowd et al. 2015). However, distances of  $\sim 0.1$  pc ( $\sim 10^4r_G$ ) have been measured in at least some objects from atomic physics arguments and ionization models (Borguet et al. 2013; Chamberlain et al. 2015).

BAL quasars display a variety of different trough shapes from object to object, as shown in Fig. 2.6. The line profiles themselves often show complex structure (Foltz et al. 1987; Ganguly et al. 2006; Simon & Hamann 2010) and can be time variable (Hall et al. 2011; Capellupo et al. 2011, 2012, 2014; Filiz Ak et al. 2012). Furthermore, there are a set of quasar absorption systems that show BAL-like absorption troughs with much smaller velocity widths. Depending on their width, these are known as narrow absorption lines (NALs) or ‘mini-BALs’ (Misawa et al. 2007, 2008; Nestor et al. 2008). While some of this behaviour can be explained once again as a viewing angle effect (e.g. Ganguly et al. 2001), the range of BAL profile shapes suggests that they are far from a homogenous population, and may also possess multi-scale substructures (clumps) in their flows. Clumping is discussed in more detail in sections 2.1.4 and 2.2.2, as well as in chapter 5.

Due to the connection between X-rays and photoionization / absorption, the X-ray properties of BAL quasars are particularly important. BALQSOs are universally X-ray weak when compared to non-BAL quasars (Gibson et al. 2009). The X-ray weakness of BALQSOs is often attributed to X-ray absorption with column densities of  $N_H \sim 10^{22-24} \text{ cm}^{-2}$  (Gallagher et al. 1999, 2002; Green et al. 2001; Grupe et al. 2003; Stalin et al. 2011),

although there is also evidence that BALQSOs are *intrinsically* X-ray weak (Sabra & Hamann 2001; Clavel et al. 2006; Morabito et al. 2013). The X-ray properties of BAL quasars are fundamentally coupled to the properties of the wind – the X-ray absorption may be caused by the outflow which in turn has its ionization state determined by the X-ray radiation. Furthermore, the true X-ray luminosities cannot be reliably inferred until inclinations of BALQSOs are constrained, as gravitational lensing will significantly alter the emergent angular distribution of X-ray emission even for an intrinsically isotropic source (Chen et al. 2013a,b).

Although the X-rays in BALQSOs are weaker than in similar mass quasars, they still possess strong ionizing power. This leads to what has become known as the ‘over-ionization problem’ in BALQSOs; how is the moderate ionization state of the BAL gas maintained in the presence of ionizing X-rays? A number of potential solutions have been proposed, which can be broadly separated into ‘shielding’ models (Murray et al. 1995; Proga & Kallman 2004) and ‘clumpy’ models (de Kool & Begelman 1995; Hamann et al. 2013). Some of these models are discussed further in section 2.3 and chapter 5.

### 2.1.3.2 Warm Absorbers

Warm absorbers (WAs) are regions of photoionized plasma responsible for some of the characteristic absorption features seen in the X-ray spectra of AGN (Reynolds & Fabian 1995). In particular, they produce photoelectric continuum absorption (e.g. Halpern 1984; Cappi et al. 1996; Kriss et al. 1996) and a series of narrow absorption lines in H-like and He-like ions of C, N, O, Si, Ne, and Fe (Kaastra et al. 2000), that appear in the soft X-rays. A wind origin is a common hypothesis for WAs (e.g. Krolik & Kriss 2001). Clear evidence for this comes from the measured blueshifts of the lines, typically on the order of  $\sim 100 \text{ km s}^{-1}$ . X-ray absorption and WAs are often variable (Fabian et al. 1994; Otani et al. 1996), which may be interpreted in terms of changing kinematics of an accretion disc wind (Connolly et al. 2014). There is also evidence of contemporary UV and X-ray absorption in NGC 5548 (Kaastra et al. 2014) and mini-BALs (Giustini et al. 2011), and as mentioned above BALQSOs are often absorbed in the X-rays. This suggests that the outflow phenomenon across a large range of ionization states and line energies is linked.

WAs can, in some cases, be modelled well with single component models (Kaastra et al. 2000), but often require multiple ionization state absorbers (e.g. Kriss et al. 1996; Orr et al. 1997; Krolik & Kriss 2001; Connolly et al. 2014). If this is the case, then self-consistent ionization and radiative transfer models should really be used to model the spectrum (see e.g. chapter 3), as optically thin ionization parameter estimates will not capture the ionization and radiation physics. The collated observations point towards some kind of outflow with a stratified ionization structure, with  $\log \xi \sim 0 - 2$ , and densities on the order of  $10^8$  cm. These physical conditions or scales are not well constrained, and the connection to other outflows is unknown. Timing observations will help to shed light on the properties of the mysterious, but ubiquitous, AGN WAs (Silva et al. 2015).

### 2.1.3.3 Ultra-fast Outflows

As well as acting as WAs, winds also imprint clear absorption features in highly ionized Fe K $\alpha$  lines in AGN such as PDS 456 (Reeves et al. 2003; Gofford et al. 2014; Matzeu et al. 2016), MCG-5-23-16 (Braito et al. 2007) and PG 1211+143 (Pounds & Reeves 2009; Fukumura et al. 2015). These features are fairly common in Seyfert galaxies (Tombesi et al. 2010; Gofford et al. 2013). An example of such a feature is shown in Fig. 2.7 with a simply spherical outflow model fit, from (Nardini et al. 2015). The high velocities ( $\sim 0.1c$ ) inferred from the line blueshifts have lead to these winds becoming known as ultra-fast outflows, or UFOs.

UFOs are characterised by ionization parameters of  $\log \xi \sim 3 - 4$ , and column densities of  $N_H > 10^{22}$  cm $^{-2}$ . Their high mass-loss rates and large energy budgets mean that they are natural candidates for AGN feedback (see section 2.5). Measurements of their kinetic luminosities suggest that UFOs do have sufficient energy to affect their host galaxy (Gofford et al. 2015), and a recent observation showed a molecular outflow in a UFO host galaxy, possibly driven by the UFO itself (Tombesi et al. 2015). As with WAs, many of the models used to constrain physical parameters are simplistic, and assume single ionization parameters, large covering factor and thin expanding shells of outflow. Under these assumptions, the mass loss rate can be estimated using

$$\dot{M} \sim \Omega N_H m_p v_{out} R_{in} \quad (2.1)$$

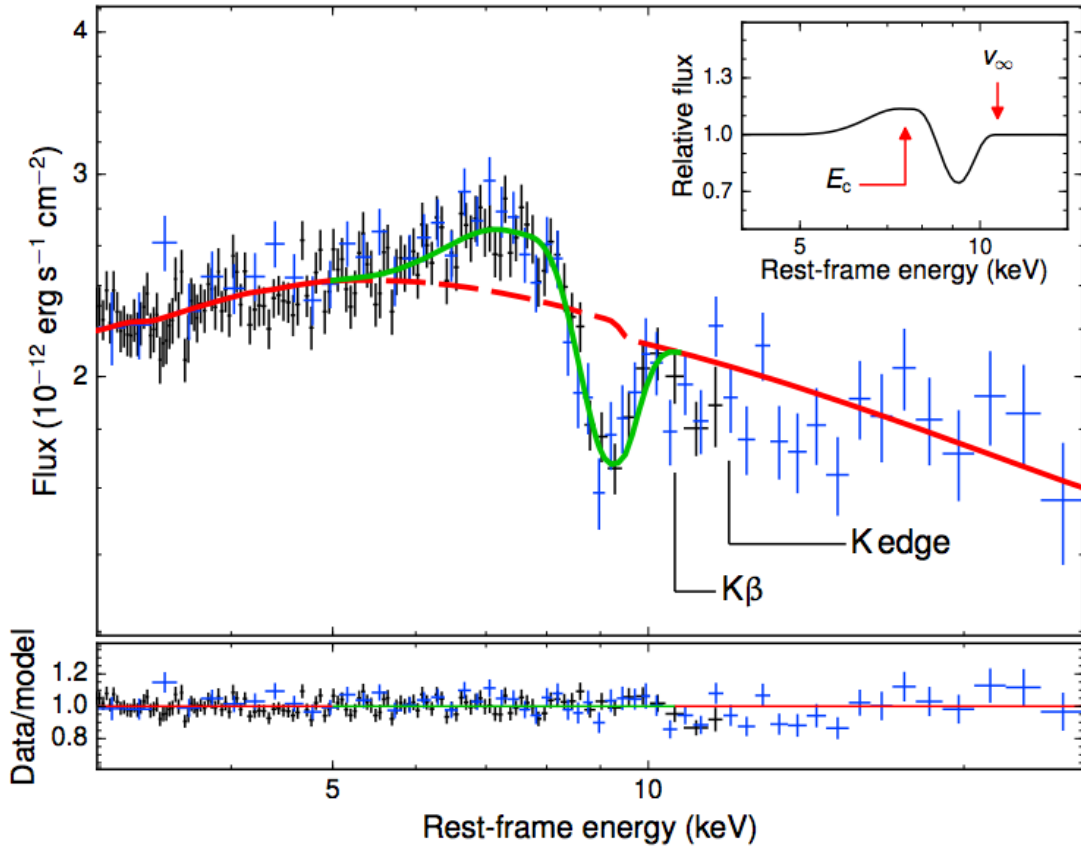


FIGURE 2.7: Credit: Nardini et al. 2015. X-ray spectrum of PDS 456 fitted with a P-Cygni profile from a spherical outflow model. *XMM-Newton* data is shown in black with two combined *NuStar* observations in blue.

In reality, the absorber is probably much more complex, and full RT and photoionization simulations are required. In a series of papers, Sim et al. (2008, 2010a,b) carried out such calculations, and found reasonable verisimilitude with Fe line profiles could be achieved. However, as with many models for AGN, a holistic, broad wavelength range fit is still required.

#### 2.1.4 Stellar Winds

Although stellar winds are clearly not accretion disc winds, they provide a useful, and better understood, testing ground for much of the physics of radiatively-driven outflows. Wolf-Rayet (WR) stars and O-stars possess strong outflows with mass-loss rates of up to  $10^{-5} M_{\odot} \text{ yr}^{-1}$ , thought to be driven by radiation pressure mediated by spectral lines (see section 2.2.3). Over the typical lifetime of a massive star ( $\sim 10^6$  yr), this can have a significant impact on the overall mass, causing losses of around  $10 M_{\odot}$  of material.

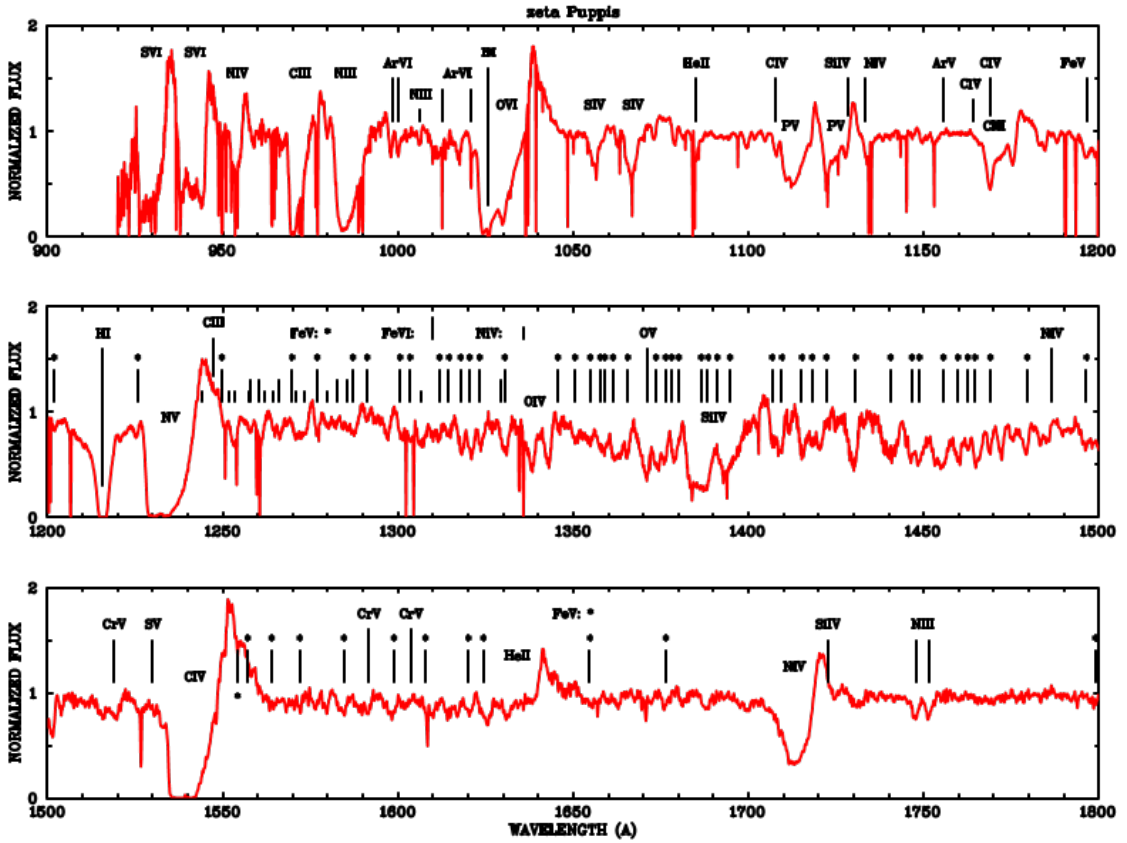


FIGURE 2.8: Credit: Pauldrach et al. 1994. UV spectrum of one of the brightest massive O stars, the O4 supergiant  $\zeta$  Puppis. The spectrum is merged from Copernicus and IUE UV observations, and the prominent lines are marked.

As with the systems described previously, the P-Cygni profiles in spectra from hot, massive stars are the main pieces of evidence that a strong wind is present (see Fig. 2.8). Mass-loaded winds are also thought to be responsible for the emission lines seen in hot star spectra (e.g. Pauldrach et al. 1994). Indeed, emission line diagnostics have been particularly important in determining the mass-loss rates of stellar winds, and have been used to demonstrate that line-driven stellar winds are expected to be clumpy.

#### 2.1.4.1 Clumping in stellar winds

Evidence for clumping in hot star winds comes from a wide range of sources. Perhaps the most conclusive evidence comes from electron scattering wings in emission lines; homogenous models overestimate the strength of these wings, whereas clumpy models produce good agreement with data (Hillier 1984, 1991; Hamann et al. 1992, 1994; Schmutz 1997). Further evidence for clumping comes from line variability (Prinja & Smith 1992) and polarisation (Brown et al. 1995). Clumping is theoretically expected

in line-driven winds (see section 2.2.3 and the review by Owocki 2014), and is directly dealt with in this thesis. I describe the treatment of clumping I have implemented in our radiative transfer code in section 3.8, before presenting results from a clumpy AGN wind model in chapter 5.

### 2.1.5 Outflow Physics

The spectra in figures 2.2, 2.6 and 2.8 show striking similarities – characteristic broad, P-Cygni-like absorption features in UV resonance lines extending to high blueward velocities – despite vast differences in mass. Furthermore, some of the phenomena observed in e.g. stellar winds may naturally solve some of the unanswered questions in other systems; for example, clumping may prevent over-ionization in AGN outflows. It would seem that at least some of the physics of outflows, like accretion, is universal, and that lessons learned from smaller scale systems may be scaleable to AGN and quasars. To understand if the similarity extends beyond a cosmetic one, I will discuss some of the underlying physical mechanisms that may be responsible for accelerating these outflows.

## 2.2 Driving Mechanisms

Let us consider a parcel of ideal gas. By imposing nothing more than conservation of mass, energy and momentum on that parcel we can write down three equations of hydrodynamics <sup>1</sup>

$$\frac{D\rho}{Dt} + \rho\nabla \cdot \vec{v} = 0 \quad (2.2)$$

$$\rho \frac{Dv}{Dt} = -\nabla P + \frac{1}{4\pi}(\nabla \times \vec{B}) \times \vec{B} + \rho \vec{F}_{rad} + \rho \vec{g} \quad (2.3)$$

$$\rho \frac{D}{Dt} \left( \frac{e}{\rho} \right) = P \nabla \cdot \vec{v} + \rho \mathcal{L} \quad (2.4)$$

---

<sup>1</sup>I stress that these equations are not used in hydrodynamic simulations in this thesis (see chapter 5, for example); they are discussed here because they provide a natural reference point for exploring potential driving mechanisms for winds in accreting systems.

Here  $D$  denotes a derivative within the comoving frame of the gas parcel,  $\vec{v}$  is the velocity,  $\rho$  is the gas density,  $\vec{B}$  is the local magnetic field,  $\vec{F}_{rad}$  is the radiation force per unit mass and  $\vec{g}$  denotes the gravitational acceleration vector. Equation 2.2 is the *continuity equation* and describes conservation of mass. Equation 2.3 is the *equation of motion* and describes conservation of momentum. Equation 2.4 is the *equation of energy conservation*. Equation 2.3 can be used to neatly demonstrate how an outflow can be driven. I have deliberately written the equation so that all the force terms lie on the RHS. For an outflow to be driven from an accreting object one of terms on the RHS must dominate over gravity,  $\rho\vec{g}$ . These terms thus signify three potential driving mechanisms.

- Magnetic Forces,  $\frac{1}{4\pi}(\nabla \times \vec{B}) \times \vec{B}$ .
- Radiative Forces,  $\rho\vec{F}_{rad}$ .
- Thermal Pressure,  $-\nabla P$ .

We can now examine under what physical conditions (and in which corresponding astrophysical objects) we might expect these forces to overcome gravity and cause a parcel of mass to escape to infinity. In other words: *what might drive a wind?*

### 2.2.1 Thermal Winds

In hydrostatic equilibrium (HSE), thermal pressure balances gravity and no other forces are present, meaning that the equation of motion can be written as

$$\rho \frac{Dv}{Dt} = -\nabla P + \rho\vec{g} = 0 \quad (2.5)$$

Clearly, if the thermal pressure is then significantly increased then this equilibrium condition no longer holds. This can occur in accretion discs at temperatures in excess of  $\sim 10^7$  K – where other forces are negligible compared to thermal pressure – and where the escape velocities are relatively low (i.e. far out in the disc). Due to the temperature and gravity scalings, this means that XRBs are natural candidates for showing evidence of thermally driven winds. The outer disc can be heated to the Compton temperature by the central X-ray source, potentially driving relatively high mass-loss rate outflows

([Begelman et al. 1983](#); [Woods et al. 1996](#)). This driving mechanism has been proposed as a natural explanation for the ever-present equatorial outflows in soft state XRBs ([Ponti et al. 2012](#)). However, they are much less likely candidates in CVs and AGN, because the escape velocity tends to greatly exceed the thermal velocity.

### 2.2.2 Radiatively Driven Winds

Under spherical symmetry, one simply obtains the Eddington limit discussed in section [1.1.1](#) when  $\rho\vec{F}_{rad} = \rho\vec{g}$ . Hence, sources must be fairly close to the Eddington luminosity in order to drive an outflow purely from radiation pressure on electrons. There are a number of accreting systems that may drive super-Eddington (or close to Eddington) outflows, such as AGN with UFOs (e.g. [Reeves et al. 2002](#); [Pounds et al. 2016](#)), NLSIs ([Done & Jin 2015](#)) and ultra-luminous X-ray sources (ULXs; [Walton et al. 2013](#)). However, high-state CVs are certainly significantly below the Eddington limit (REF), and at least some BALQSOs have low Eddington fractions ([Grupe & Nousek 2015](#)). Despite this, line opacity may mean that radiation is still responsible for the powerful outflows in these systems even at  $L/L_{Edd} \sim 10^{-3}$ .

### 2.2.3 Line-driven Winds

Under the right ionization conditions, radiation pressure mediated by spectral lines can be a significant acceleration term in a partially ionized plasma ([Castor et al. 1975](#), hereafter CAK). The most common way to parameterise the cumulative effect of lines on the radiation force is via the *CAK force multiplier*,  $\mathcal{M}(t)$ , which modifies the equation for the radiation force to give ([Castor 1974](#), CAK, )

$$\vec{F}_{rad} = \frac{\sigma_e F}{c} \mathcal{M}(t), \quad (2.6)$$

where  $t = \beta\tau_L$  for a given line and  $\mathcal{M}(t)$  can be approximated by

$$\mathcal{M}(t) = t^{-\alpha} \left( \frac{n_e}{10^{11} \text{ cm}^{-3}} \right)^\delta W^{-\delta}. \quad (2.7)$$

Here  $W$  is the dilution factor, and  $k$ ,  $\alpha$  and  $\delta$  are constants with values of 0.28, 0.56 and 0.99 respectively in O-star winds ([Abbott 1982](#)). It is possible to show (CAK,

Owocki et al. 1988) that the maximum force multiplier is around 2000 – 4000. This is already an interesting result, as it tells us that line-driven outflows can be accelerated when accretion rates / luminosities are much lower than the Eddington limit. Indeed, using equation 2.6 we can see that a radiatively driven wind can be accelerated when  $L_{UV} > L_{Edd}/M_{UV}(t)$ , where the UV subscript pertains to the UV region of the spectrum and  $M_{UV}(t)$  will thus depend on the lines in this region and their relative ionization and excitation fractions. Line-driven winds are present in O-stars and Wolf-Rayet stars and the theory produces good matches with observations (REFs). It is also a strong candidate for driving the strong winds seen in high-state CVs when the accretion disc is UV bright (e.g. Pereyra et al. 1997; Proga et al. 1998; Proga 2005, see also section 2.3.4).

Line driving is also a promising candidate to explain BAL outflows, as the strong UV resonance lines seen in absorption in O stars are also present in BALQSOs. The presence of ‘line-locked’ features (Bowler et al. 2014) and the ‘ghost of Ly $\alpha$ ’ (Arav et al. 1995; Arav 1996; North et al. 2006) in the spectra of some BALQSOs also gives clearer evidence that line-driving is at least partially contributing to the acceleration of the wind (but see also Cottis et al. 2010). However, the presence of an X-ray source complicates matters. We have already briefly touched on the ‘over-ionization’ problem in AGN outflows, but it now has another consequence. Not only will strong X-rays prevent the right features forming in the spectrum, but, if the outflow is line-driven, they will prevent the wind existing in the first place. Despite these problems, potential solutions exist and hydrodynamic simulations have been successful in producing high mass-loss rates (see section 2.3.4).

#### 2.2.4 Magnetic Winds

Magnetic fields are one of the main proposed mechanisms for transporting angular momentum outwards in the disc via the MRI. This would imply that magnetic fields are important in shaping accretion discs and makes them attractive as a driving mechanism for disc winds.

There are two main ways in which magnetic forces can drive an accretion disc wind. Historically, the most popular idea has been the ‘bead on a wire’ mechanism proposed by (Blandford & Payne 1982). In this model, the *poloidal* magnetic field is dominant, and the wind is driven by magnetic *tension*.

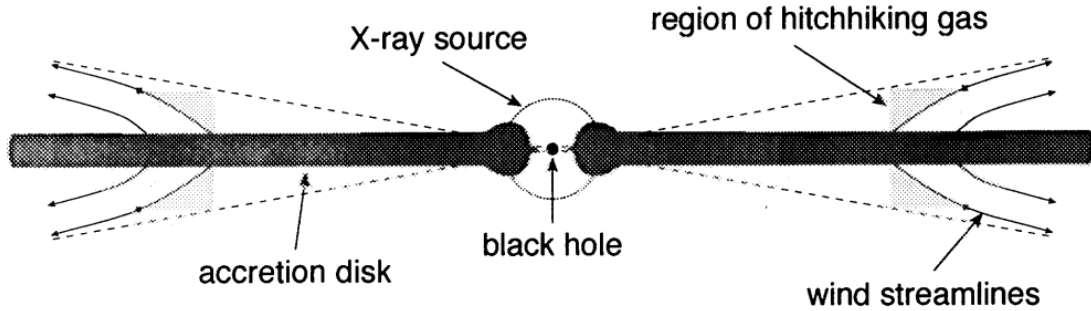


FIGURE 2.9: Credit: Murray et al. 1995. Cartoon showing the geometry of the MCGV95 model.

In alternative magnetic models the magnetic pressure ( $B/8\pi$  in CGS units) is responsible for driving the outflow (REFs and explanation).

## 2.3 Accretion Disc Wind Models

A number of different wind models have appeared in the literature over the years, each attempting to explain the different observational characteristics of quasars with a mixture of conceptual frameworks and underlying physics. Typically, the models attempt to explain the origins of BLR and BAL gas, although some extend their remit into the infra-red, radio and X-ray regimes. I will briefly discuss a few examples that have gained traction over the years, before outlining the kinematic prescription I have used in the modelling that forms part of this thesis.

### 2.3.1 MCGV95: A Line-driven Wind Model for AGN

In the MCGC95 model, a smooth wind rises from an accretion disc with a launch radius of around  $10^{16}$  cm. The wind is equatorial, with an opening angle of  $5^\circ$ , and is accelerated by line forces up to a terminal velocity of  $0.1c$ . A diagram of the geometry is shown in Fig. 2.9. One of the key features of the models is the presence of a ‘shield’ of hitchhiking gas, which protects the outflow from X-ray over-ionization and allows radiation pressure on UV resonance lines to efficiently accelerate the flow.

MCGV95 found that BAL profiles were seen for an observer looking into the wind cone, and significant line *emission* emerged at low inclinations. This line emission came from a relatively small BLR ( $r_{BLR} \sim 10^{16}$  cm) at the base of the wind, where densities

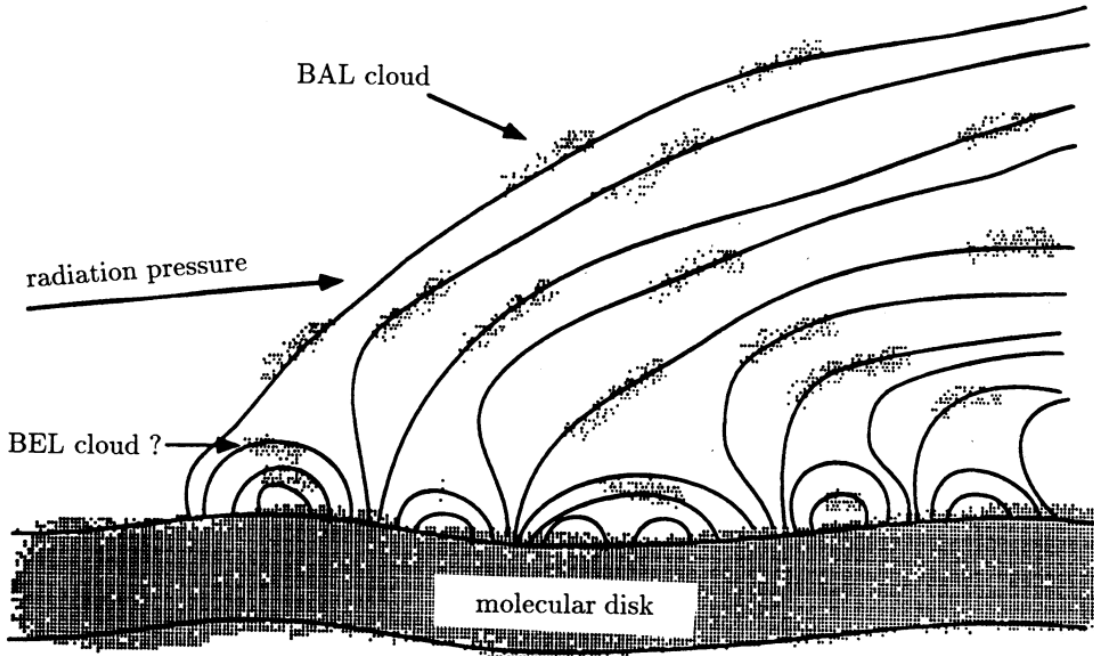


FIGURE 2.10: Credit: De Kool & Begelman 1995.

were high ( $n_e \approx 10^{10} \text{ cm}^{-3}$ ). The MCGV95 model was one of the first successful disc-wind unification models, and is especially impressive as it includes photoionization calculations and quantitative estimates of the resultant line EWs. However, the effects of multiple scattering and complex radiative transfer effects could not be included in their calculations (see chapter 5).

### 2.3.2 De Kool & Begelman: A Radiatively Driven, Magnetically Confined Wind

It is of course possible that radiation and magnetic fields are both important in determining the outflow characteristics. In the [de Kool & Begelman \(1995\)](#) model, radiation pressure drives an outflow from an accretion disc, and also compresses the magnetic field lines that are dragged along with the flow. This causes the magnetic field strength in certain regions to be comparable to the gas pressure, meaning that clouds can be magnetically confined in the flow. A diagram is shown in Fig. 2.10. The authors find that such a model would naturally emerge at a fairly equatorial angle with a covering factor of around 10%, and that lower ionization material would be intercepted when the system was viewed from higher inclinations, potentially explaining some of the properties of LoBALQSOs.

### 2.3.3 Elvis 2000: A Structure for Quasars

[Elvis \(2000\)](#) expanded on the work of MCGV95 by proposing a simple biconical model, empirically derived to explain as much of quasar phenomenology as possible within one unifying framework. The geometry of the Elvis model is shown in Fig. 2.11. As in the two previous models, observers looking into the wind cone will see a BALQSO, whereas observers looking down onto the wind will see a type 1 quasar. Initially, the wind rises vertically, so that observers looking underneath the flow will see NALs due to the small range of velocities intercepted by their line of sight.

The flow conserves angular momentum, such that the initial Keplerian velocities determine the BEL widths, before accelerating to BAL-like velocities of  $\sim 0.1c$ . The wind is assumed to be two-phase, with BEL and BAL clouds embedded in a warm, highly ionized medium (WHIM). This WHIM is responsible for WA-like absorption and the X-ray scattering phenomena seen in AGN. It is also responsible for confining the BAL and BEL clouds, allowing high densities and cooler temperatures to exist within the flow. The ionization structure for the wind is stratified, such that the material further out along the disc plane is somewhat shielded from the inner disc and X-rays. This allows the lower ionization BEL profiles to form in the right locations, and also means that LoBAL profiles would be seen at a subset of inclinations.

### 2.3.4 Proga et al.: Line-driven Hydrodynamic Models for AGN and CVs

Around the turn of the century, Daniel Proga and collaborators published a series of important papers in which they conducted hydrodynamic simulations of accretion disc winds in AGN and CVs. In the first of these, the problem considered was that of disc winds in CVs ([Proga et al. 1998](#)). In their model, the disc was assumed to radiate according to the  $\alpha$ -disc model, and the central WD was also included as a radiating source. They found that when the disc had an Eddington fraction of greater than  $\approx 1/\mathcal{M}_{max}(t) = 0.001$ , then strong, line-driven outflows were driven from a few WD radii with bending angles of  $\sim 45^\circ$ . This result agreed qualitatively with outflows in CVs and later efforts to compute synthetic line profiles produced promising results ([Proga et al.](#)

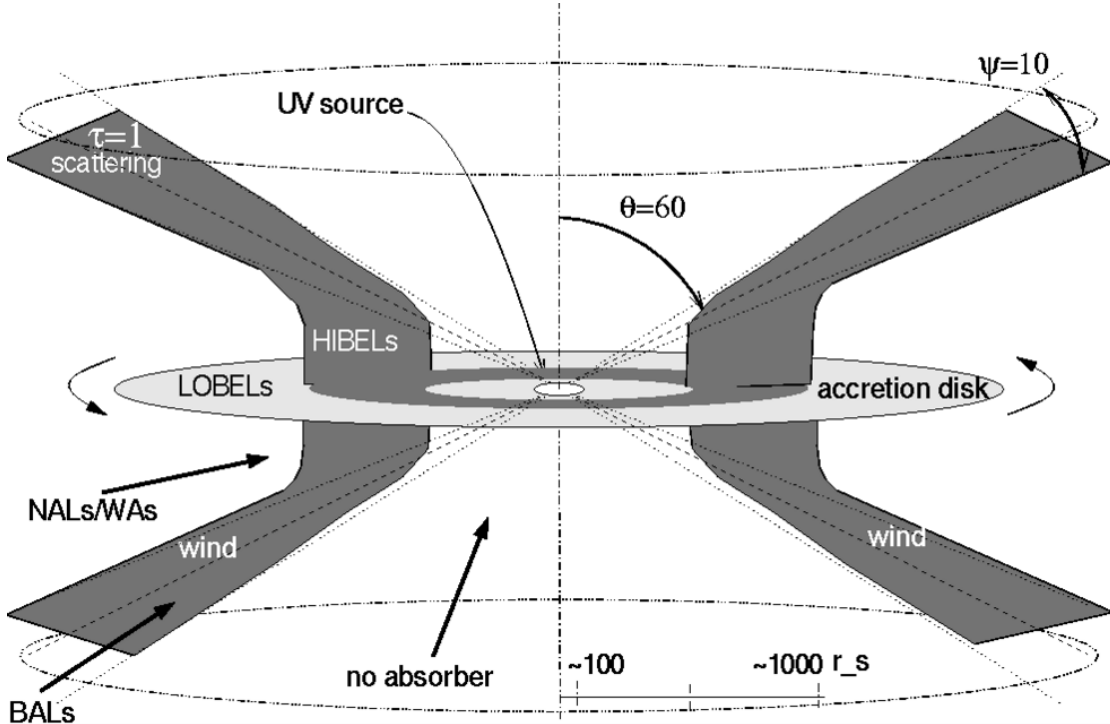


FIGURE 2.11: Credit: Martin Elvis. A schematic showing the main features of the Elvis model. A biconical wind rises from an accretion disc, and the observed spectrum is determined purely by the viewing angle of the observer.

2002). This was the first successful demonstration of line-driving in a full hydrodynamic simulation.

The same principle was then applied to the problem of AGN outflows, with the additional complication of an ionization X-ray source now included (Proga et al. 2000; Proga & Kallman 2004, hereafter PK04). A density snapshot from the PK04 model is shown in Fig. 2.12. An inner ‘failed’ wind formed in this simulation, which initially rose up from the disc before being over-ionized by the central X-rays. Crucially, this acted as a shield, similarly to the hitchhiking gas proposed by MCGV95, and allowed a line-driven wind to be accelerated further out in the disc. This outflow can be seen clearly in Fig. 2.12.

One of the interesting results of the Proga-led simulations is that they tended to produce somewhat unsteady, clumpy flows. In the CV case, this was caused by the interaction between the line force and gravity, as both force terms varied differently with height. In the AGN case, it was instead due to the critical importance of the ionization state on the line force. Parcels of gas could only be accelerated when they were of the right ionization state, and this depended critically on their density and the radiation field they see. This caused a complicated interaction between the dynamics of the flow and the

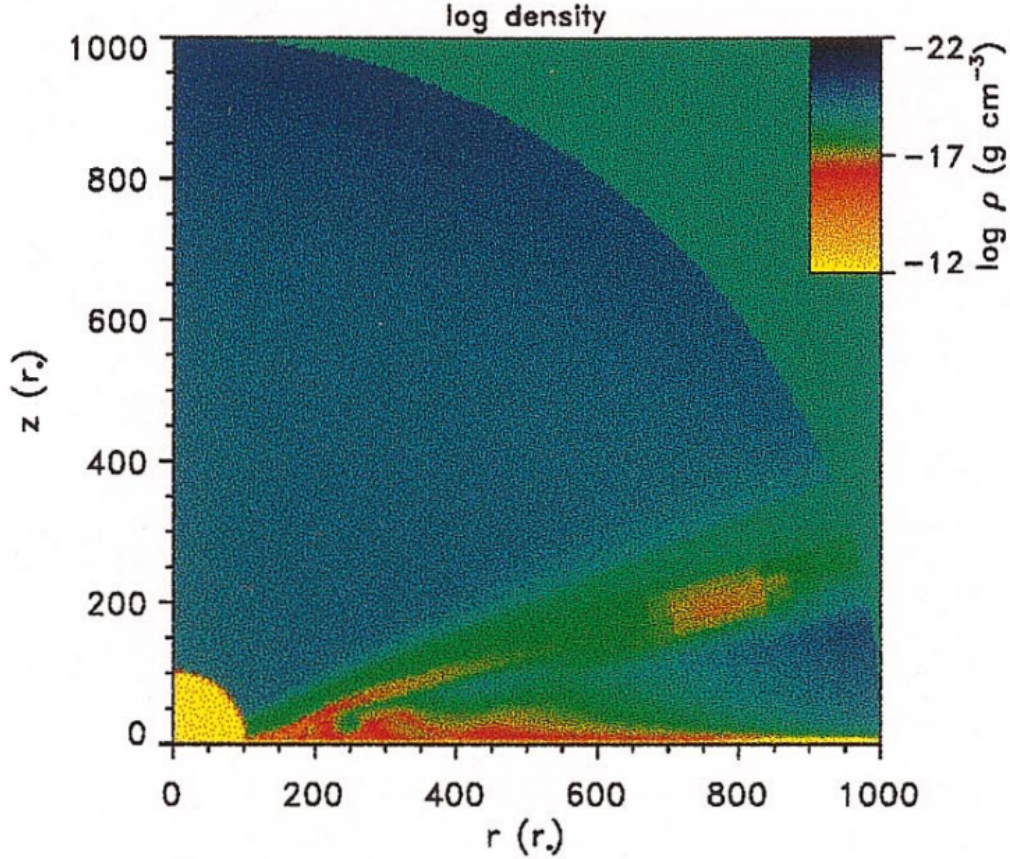


FIGURE 2.12: Credit: Proga & Kallman 2004. Density snapshot of the PK04 model.

path of ionizing radiation, which are coupled. The radiation field also helped determine the geometry of the outflow, as increasing the strength of the radiation interior to the launch radius tends to flatten out the wind and lead to more equatorial outflows ([Proga 2005](#)). This is particularly important when considering quasars and unification, as it means the viewing angles of BALQSOs can tell us about where the wind is launched.

It is worth noting that the smaller scale LDI could not be included in this model, partly for computational reasons and partly because of the approximations used to treat the radiation field. Indeed, in a subsequent study ([Higginbottom et al. 2014](#), hereafter H14) showed that treating the radiation transport properly is crucially important, as in this particular geometry multiple scattering means that the shielding region is ineffective, and radiation will simply find its way around the failed wind to over-ionize the flow beyond. Ideally, full radiative transfer and hydrodynamical simulations would be used to estimate the viability of line-driven winds. Our team is currently working on this problem (see H14 for the first step); however, much can also be learned from simpler, kinematic

prescriptions for outflows, which can then be treated with full radiative transfer and ionization treatments.

## 2.4 A Kinematic Prescription

([Shlosman & Vitello 1993](#), hereafter SV93) expanded on the work of the stellar wind community (e.g. [Abbott & Lucy 1985](#)) in proposing a kinematic prescription for an accretion disc wind. Unlike hydrodynamical models, this model has no real predictive power in terms of velocities and mass-loss rates. Instead, one sets these quantities in advance and examines the resultant properties of the flow and emergent spectra. The SV93 prescription is the most common wind model used in the radiative transfer code PYTHON (see chapter 3), and has been used to simulate spectra for CVs ([Long & Knigge 2002](#); [Matthews et al. 2015](#), chapter 4), AM CVn systems ([Kusterer et al. 2014](#)) and AGN/quasars ([Higginbottom et al. 2013](#); [Matthews et al. 2016](#); [Yong et al. 2016](#), chapter 5). A similar philosophy applied to the model of [Knigge et al. \(1995\)](#), and which has been used with similar applications ([Long & Knigge 2002](#); [Sim et al. 2008, 2010a](#)), as well as young-stellar objects (YSOs; [Sim et al. 2005](#)). Kinematic prescriptions have thus been a useful tool in providing quantitative tests of conceptual models, and assessing their ability to reproduce the observed spectra of a variety of disc wind systems.

In the SV93 parametrization a smooth, biconical disc wind emanates from the accretion disc between radii  $r_{min}$  and  $r_{max}$ . A schematic is shown in Fig. ???. The covering fraction of the outflow is also controlled by the inner and outer opening angles of the wind,  $\theta_{min}$  and  $\theta_{max}$ , and the launch angle of the other streamlines is given by

$$\theta(r_0) = \theta_{min} + (\theta_{max} - \theta_{min}) \left( \frac{r_0 - r_{min}}{r_{max} - r_{min}} \right)^{\gamma}, \quad (2.8)$$

where  $r_0$  is the launch radius of the streamline.

The poloidal (non-rotational) velocity field of the wind,  $v_l$ , is given by

$$v_l = v_0 + [v_{\infty}(r_0) - v_0] \frac{(l/R_v)^{\alpha}}{(l/R_v)^{\alpha} + 1}, \quad (2.9)$$

where  $l$  is the poloidal distance along a particular wind streamline. The terminal velocity along a streamline,  $v_{\infty}$ , is set to a fixed multiple of  $v_{esc}$ , the escape velocity at the

launch point. The terminal velocity will therefore be higher for streamlines closer to the inner disc edge. The launch velocity from the disc surface,  $v_0$ , is assumed to be constant (set to 6 km s<sup>-1</sup>). Once the wind is launched, it accelerates, reaching half of its terminal velocity at  $l = R_v$ . The velocity law exponent  $\alpha$  controls how quickly the wind accelerates. Larger values of  $\alpha$  cause the main region of acceleration to occur close to  $R_v$ , whereas smaller values correspond to fast acceleration close to the disc (see Fig. 2.13). The rotational velocity  $v_\phi$  is Keplerian at the base of the streamline and the wind conserves specific angular momentum, such that

$$v_\phi r = v_k r_0, \quad (2.10)$$

where  $v_k = (GM_{WD}/r_0)^{1/2}$ .

The mass loss rate per unit surface area,  $\dot{m}'$  can be controlled by a free parameter  $\lambda_m$  such that

$$\dot{m}' \propto \dot{M}_W r_0^{\lambda_m} \cos[\theta(r_0)], \quad (2.11)$$

where  $\dot{M}_W$  is the total mass loss rate in the wind. This equation is normalised so that when integrated over both sides of the disc the correct  $\dot{M}_W$  emerges. I have adopted  $\lambda = 0$  throughout this thesis, which corresponds to uniform mass loss across the disc. The density at a given point can then be calculated by imposing mass conservation and using the velocity law. At the base of the wind the density is given by

$$\rho(r_0) = \frac{\dot{m}'(r_0)}{v_z(r_0)}, \quad (2.12)$$

and at a coordinate  $(r, z)$  the density will be

$$\rho(r, z) = \frac{r_0}{r} \frac{dr_0}{dr} \frac{\dot{m}'(r_0)}{v_z(r, z)} \quad (2.13)$$

where the corresponding  $r_0$  is found by considering the streamline that passes through  $(r, z)$ . I have now specified the equations that govern the kinematics and densities in the wind for the SV93 prescription. This prescription is used to describe the outflow in the radiative transfer code PYTHON. The radiative transfer procedure and ionization calculation is described in section 3.2. The radiation sources must also be described, but this is discussed in chapters 4 and 5 as it is specific to the object being modelled.

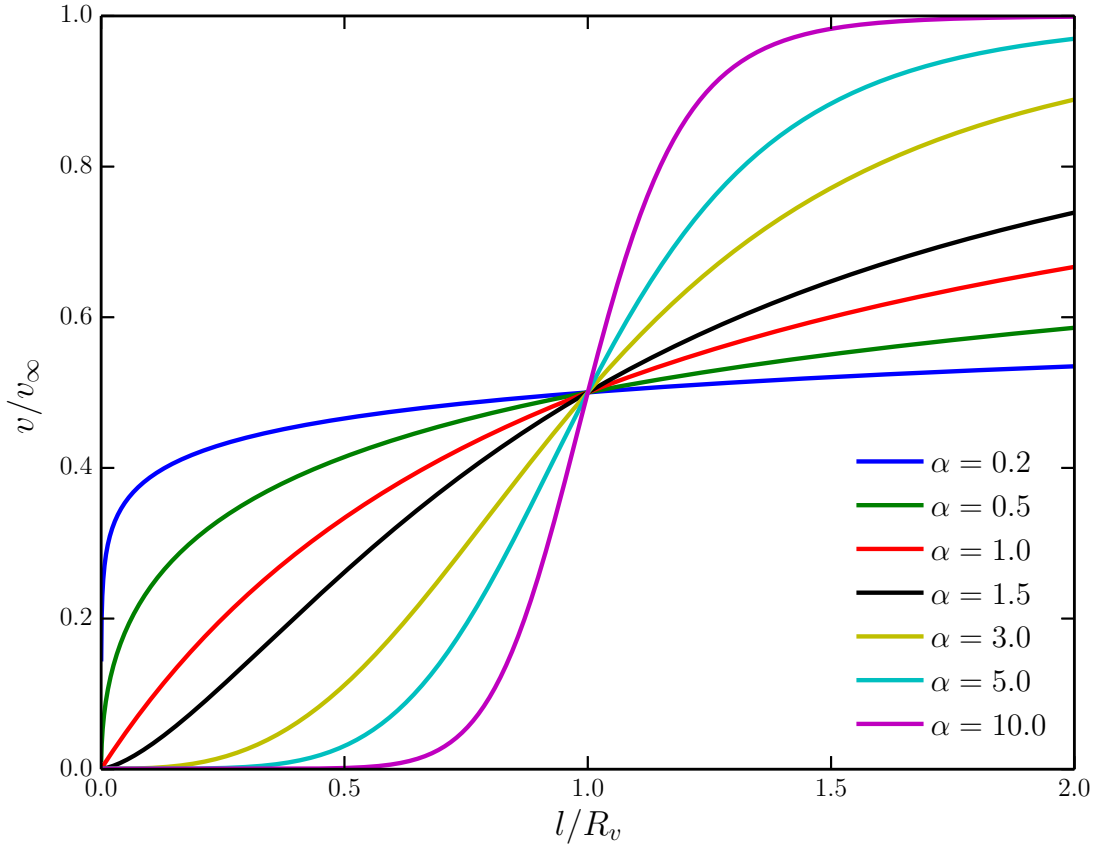


FIGURE 2.13: The SV93 velocity law for various values of the acceleration exponent,  $\alpha$ .

## 2.5 The big picture: AGN Feedback

The event horizon of a  $10^9 M_\odot$  BH is approximately  $10^{15}$  cm across, a billionth of the size of a typical galactic bulge. This is roughly the difference in size between a small coin and the Earth. Even the sphere of gravitational influence of the BH is roughly 1000 times smaller than the size of the galactic bulge. Despite this vast difference in scale, there is evidence that the physics on the scale of the gravitational radius of the BH really does affect the evolution and dynamics of its host galaxy. When considering the *energetics* of accretion this becomes less surprising. The binding energy of a galactic bulge is

$$E_{\text{bulge}} \approx M_{\text{bulge}} \sigma_*^2, \quad (2.14)$$

while the energy released in growing a black hole to a mass  $M'_{BH}$  is (assuming  $\eta = 0.1$ )

$$E_{BH} \approx 0.1 M'_{BH} c^2. \quad (2.15)$$

By combining the above two equations, and putting in typical numbers of  $\sigma_* = 0.001c$  and  $M'_{BH}/M_{bulge} = 10^{-3}$  we can show that

$$\frac{E_{BH}}{E_{bulge}} \approx 10^{-4} \left( \frac{c}{\sigma_*} \right)^2 \sim 10. \quad (2.16)$$

In other words, the energy released when growing a BH can exceed the binding energy of the galactic bulge. This energetic argument is not alone sufficient to claim that the accreting BH must affect its host. For example, if the radiated energy never experienced an optical depth of  $\sim 1$  then it would clearly not couple to the galactic bulge. However, we have already seen that many outflows in AGN possess kinetic luminosities that are significant compared to the bolometric luminosity. Thus, outflows (and jets) may provide a mechanism by which the vast accretion energies can be transferred to the BH environment.

### 2.5.1 Observational evidence for feedback

Perhaps the most famous pieces of evidence for some kind of long-distance relationship between a central BH and its host galaxy are the  $M_{BH} - \sigma_*$  (Ferrarese & Merritt 2000; Gebhardt et al. 2000; Gültekin et al. 2009) and  $M_{BH} - M_{bulge}$  (Magorrian et al. 1998; Häring & Rix 2004; McConnell & Ma 2013) correlations, shown in Fig. 2.14 and Fig. 2.15 respectively. By itself, these correlations would not necessarily imply that the AGN is having an impact on its environment; indeed, there are many different theoretical models for the origin of these relations (e.g. Somerville et al. 2001; Adams et al. 2001; Burkert & Silk 2001; King 2003; Croton et al. 2006; Kormendy & Ho 2013). However, there are many other clues that outflows and jets from AGN can affect the host galaxy evolution and morphology.

The galaxy luminosity function describes the number of galaxies in each bin of luminosity, and is generally modelled with the Schechter (1976) function. Theories of galaxy evolution tend to overpredict the number of galaxies at the high luminosity end, which can be avoided by invoking quenching of star formation by the central AGN (e.g. Read & Trentham 2005; Bongiorno et al. 2016). Galaxies also show bimodality in their colour distributions (Strateva et al. 2001; Bell et al. 2003; Baldry et al. 2004), with a clear separation between a blue, star-forming main sequence, and a red sequence with lower

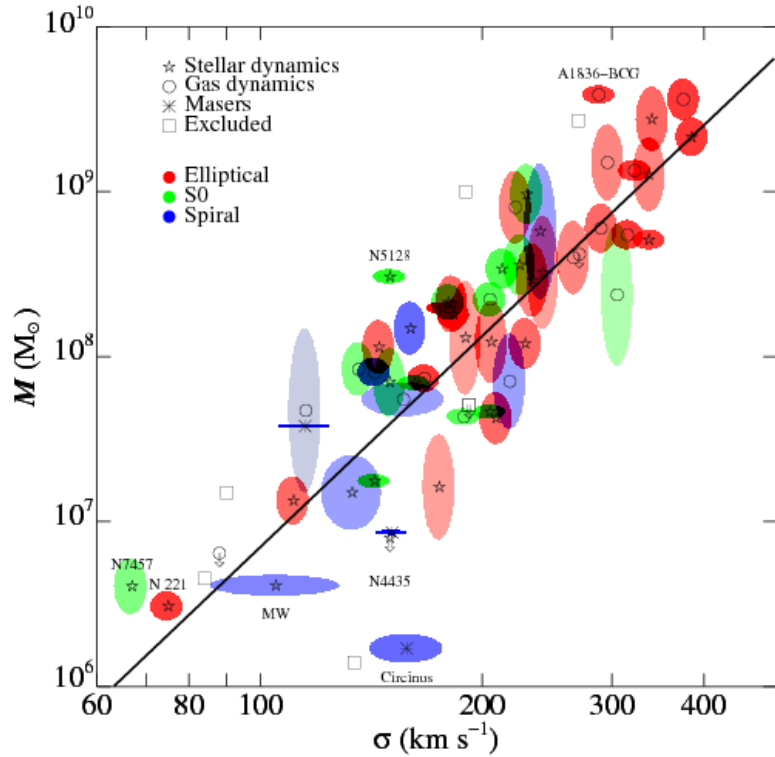


FIGURE 2.14: Credit: Gultekin et al. 2009. The  $M_{BH} - \sigma_*$  correlation.

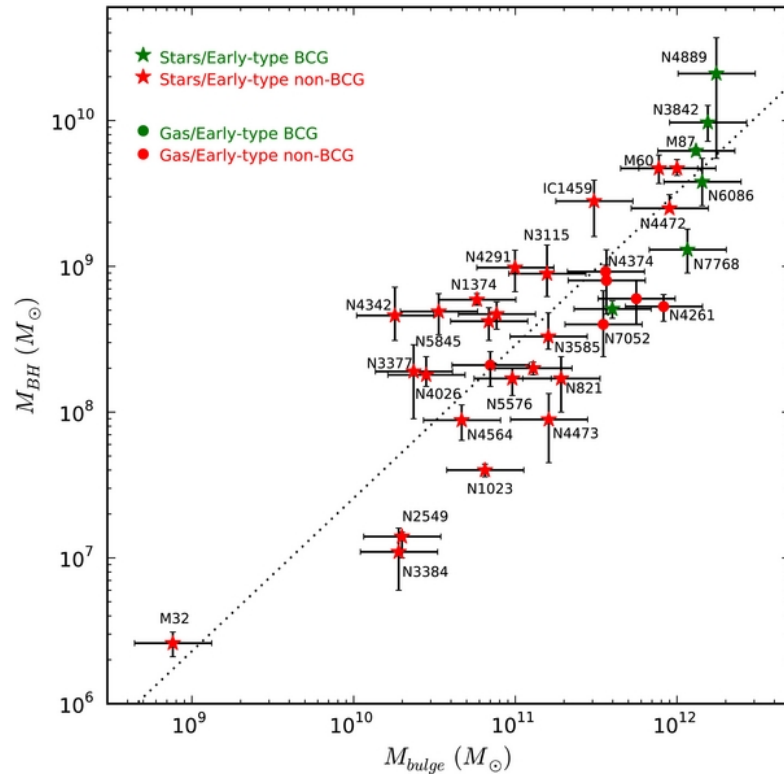


FIGURE 2.15: Credit: McConnell & Ma 2013. The  $M_{BH} - M_{bulge}$  correlation.

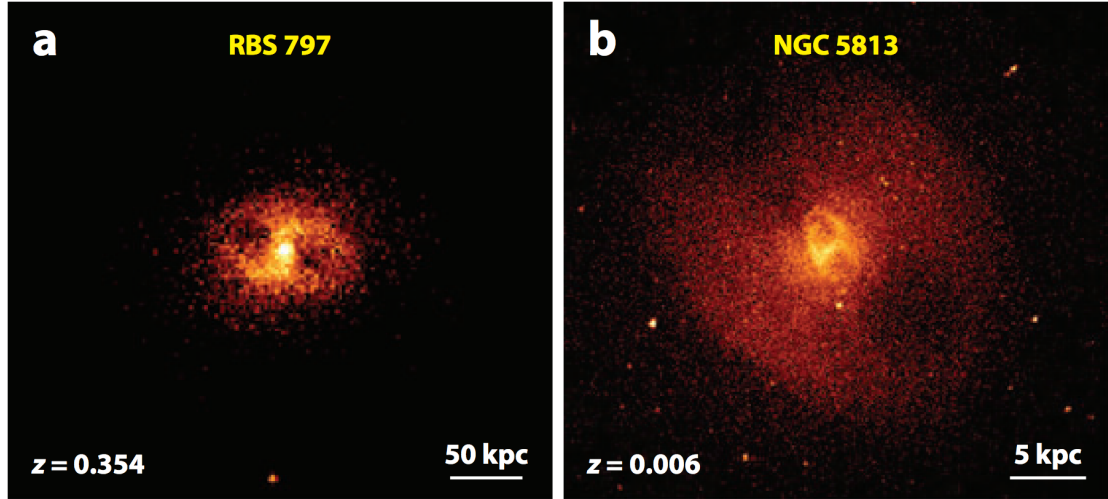


FIGURE 2.16: *Figure adapted from Fabian 2012.* Chandra X-ray images showing two examples of X-ray cavities, illustrating how a radio jet from an AGN can have a dramatic impact on its environment. a) The RBS 797 Cluster (Cavagnolo et al. 2011). b) elliptical galaxy NGC 5813 (Randall et al. 2011).

specific star formation rate (sSFR). Furthermore, these two sequences tend to lie in the same regions of colour space as the host galaxies of high and low Eddington fraction AGN respectively, implying that the AGN may be directly responsible for quenching the star formation and moving a galaxy onto the ‘red and dead’ branch. This has been demonstrated in various numerical simulations (e.g. Springel et al. 2005; Croton et al. 2006).

There is also more direct evidence that AGN are at least energetically significant when compared to the galactic bulge. X-ray observations of cool core clusters and elliptical galaxies can show dramatic X-ray cavities or bubbles on scales of up to 50 kpc, with a radio-loud AGN at the centre (Randall et al. 2011; Cavagnolo et al. 2011; Fabian 2012, Fig. 2.16). This shows how radio jets can significantly impact the surrounding gas, a flavour of feedback known as ‘radio’ or ‘kinetic’ mode. These cavities also provide an estimate of the kinetic power of a radio jet, as the volume of the bubble and surrounding gas pressure gives a rough estimate of the  $PV$  work done by the jet. This can be divided by an age estimate for the cavity, giving powers of up to  $10^{46}\text{erg s}^{-1}$ , which are weakly correlated with the radio luminosity of the source, and can be large for modest radio power (Bîrzan et al. 2008).

However, jets are not the most efficient way for AGN to interact with their environment. I have already briefly discussed in section 2.1.3.3 how fast AGN winds can drive larger-scale molecular outflows. This can be seen spectacularly in the FeLoBALQSO

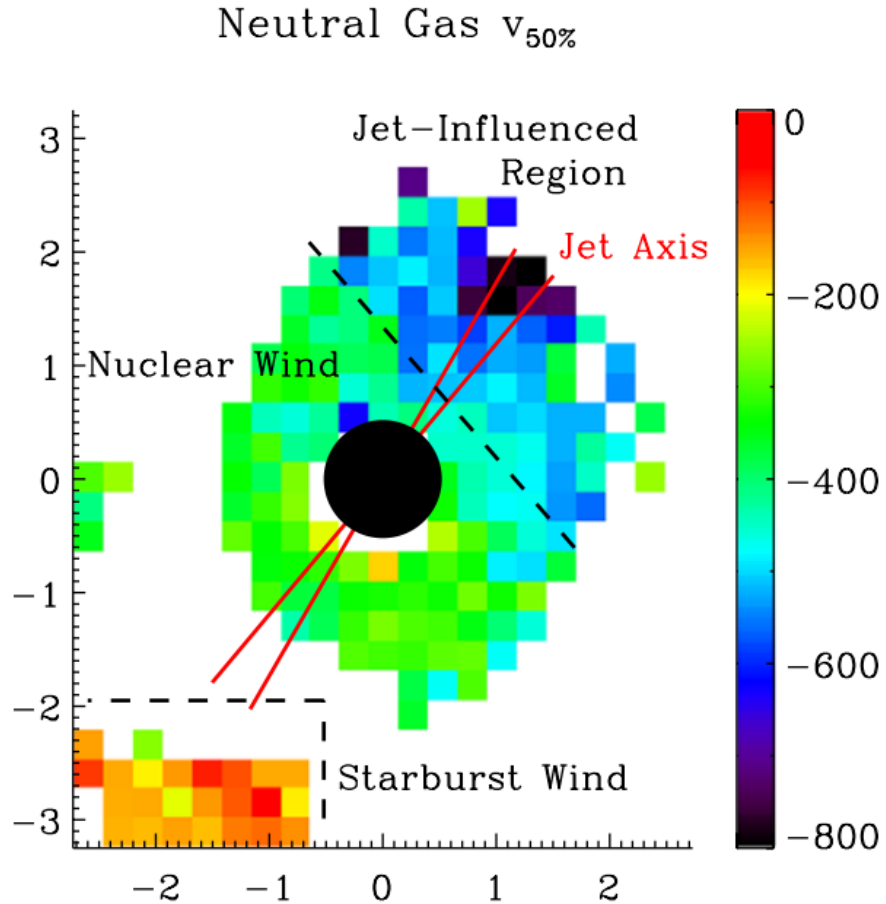


FIGURE 2.17: Credit: Rupke & Veilleux 2011. Results of Gaussian line profile fitting to integral field spectroscopy of Mrk 231. The quantity shown,  $v_{50\%}$ , corresponds to the centre of the fitted Gaussian profile and indicates that high outflow velocities are present in the neutral gas.

Mrk231, where integrated field spectroscopy shows kiloparsec-scale neutral gas outflows (see Fig. 2.17; Rupke & Veilleux 2011). King (2003) expanded on the ideas of Silk & Rees (1998) and considered a super-Eddington, momentum-driven outflow expanding into the surrounding gas. This model naturally reproduced the observed slope of the  $M_{BH} - \sigma_*$  relation. This line of argument was used to suggest that super-Eddington accretion must be common near the end of a quasar cycle, although it is worth noting that line-driving, or non-radiative driving, would mean that super-Eddington accretion rates are not required to drive such an outflow. Intriguingly, this means that understanding outflow physics has implications for the Soltan (1982) argument, SMBH spin and the accretion history of the Universe.

### 2.5.2 Alternative Explanations

It cannot yet be proven that AGN are the drivers of the observed galaxy colour evolution, high-end luminosity function discrepancy or BH-bulge correlations. Indeed, it is also possible that mergers are responsible for these phenomena; for example, major galaxy mergers may explain the colour ‘red and dead’ branch of the galaxy colour bimodality (e.g. [Somerville et al. 2001](#); [Baldry et al. 2004](#)). Regardless of the effect of mergers, AGN winds and jets are clearly energetically significant with respect to their host galaxies, and estimating their kinetic powers accurately is important in discriminating between in-situ and ex-situ scenarios.

Now the astrophysical importance of outflows has been established, I shall move on to discussing how we might go about accurately modelling the ionization states and emergent spectra from systems with accretion disc winds.

# Chapter 3

## Radiative Transfer and Ionization

“I’m splashing greys where once was  
glowing white”

Mike Vennart, *Silent/Transparent*

In the previous chapters I have given an introduction to the field and some relevant background relating to accretion discs and their associated outflows. Now it proves useful to discuss some of the specific *methods* I will use in order to answer some of the questions raised in the previous sections. In particular, I will discuss radiative transfer techniques and their potential applications.

*Notation:* This section contains a lot of algebraic quantities and sums over ions, levels, and so on. Throughout, I use  $N$  to denote fractional populations of ions and  $n$  to denote fractional populations of levels. The primed quantities  $\ell'$  and  $u'$  follow the convention of Lucy (2002) in that they denote sums over all lower/upper levels. The symbol  $\mathcal{R}$  denotes a total rate (radiative + collisional), and the symbol  $C$  is a collisional rate, whereas  $\mathcal{C}$  is a cooling rate. Starred quantities are evaluated at the stated temperature but in local thermodynamic equilibrium, following Mihalas (1982).

### 3.1 Fundamentals of Radiative Transfer

The most fundamental quantity of radiative transfer is the *specific intensity*,  $I_\nu$ , defined as

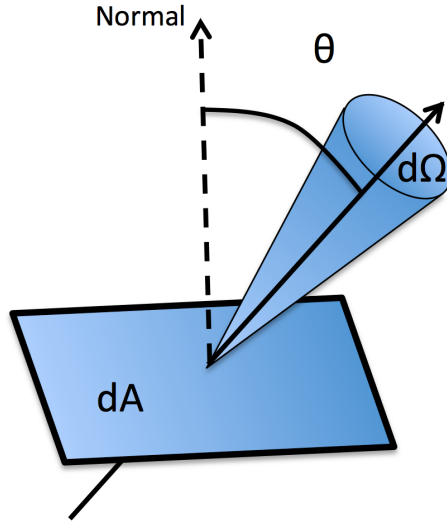


FIGURE 3.1: A schematic showing a ray obliquely incident on a surface of area  $dA$ . The labeled quantities are used in the definition of specific intensity.

$$I_\nu = \frac{dE}{d\Omega dt dA d\nu}, \quad (3.1)$$

which has units of  $\text{erg s}^{-1} \text{Hz}^{-1} \text{sr}^{-1} \text{cm}^{-2}$ . By successively multiplying by  $\cos \theta$  and integrating over solid angle we can obtain the first and second ‘moments’ of the radiation field. These are the flux,  $F_\nu$  and momentum flux,  $p_\nu$ , respectively, given by

$$F_\nu = \int I_\nu \cos \theta d\Omega, \quad (3.2)$$

$$p_\nu = \frac{1}{c} \int I_\nu \cos^2 \theta d\Omega \quad (3.3)$$

We can also define the *mean intensity*,  $J_\nu$ , as

$$J_\nu = \frac{1}{4\pi} \int I_\nu d\Omega \quad (3.4)$$

The mean intensity is particularly useful when one wants to ignore the solid angle dependence of the radiation, for example when considering the impact of an ionizing radiation field.

The equation describing the specific intensity change along a path element  $ds$  is the radiative transfer equation,

$$\frac{dI_\nu}{ds} = -\kappa_\nu I_\nu + j_\nu, \quad (3.5)$$

where  $\kappa_\nu$  and  $j_\nu$  are the absorption and emission coefficients respectively. If we define the optical depth  $d\tau_\nu = \kappa_\nu ds$  we can recast this as

$$\frac{dI_\nu}{d\tau_\nu} = -I_\nu + S_\nu \quad (3.6)$$

where  $S_\nu = j_\nu / \kappa_\nu$  is the source function. This equation is called the *formal radiative transfer equation*, and can be solved to give

$$I_\nu = I_{\nu,0} e^{-\tau_\nu} + \int_0^{\tau_\nu} S_\nu(\tau'_\nu) e^{\tau'_\nu - \tau_\nu} d\tau'_\nu. \quad (3.7)$$

A useful limit is when the source function is constant in the absorbing medium, in which case the integral can be easily evaluated to give

$$I_\nu = I_{\nu,0} e^{-\tau_\nu} + S_\nu(1 - e^{-\tau_\nu}). \quad (3.8)$$

### 3.1.1 Spectral Line Formation

From the above equations, it is trivial to show how emission and absorption lines form when the source function is approximately constant. Say we have a plasma illuminated by a blackbody of temperature  $T_0$ , such that  $I_{\nu,0} = B_\nu(T_0)$ . The plasma layer then has a different temperature,  $T$ , such that  $S_\nu = B_\nu(T)$  in that medium. By inspecting equation 3.8 we can see that if we are optically thick within the line, but optically thin in the continuum, then inside the line the source term is dominant and outside the line the first  $I_{\nu,0} e^{-\tau_\nu}$  term dominates. Therefore, if  $T > T_0$  we will see an emission line, and if  $T < T_0$  we will see an absorption line. This approach describes line emission in the blackbody limit; for more complicated SED shapes it is necessary to construct simple model atoms.

### 3.1.2 Local thermodynamic equilibrium

An important physical limit is that of local thermodynamic equilibrium (LTE). This is a first-order way to describe the physical conditions of a plasma, and assumes that all the properties of the plasma, such as the level populations and source function, are the same as those in thermodynamic equilibrium for local values of temperature and density. For this to be the case, the principle of *detailed balance* must also apply, in which every process by which electrons transition in state must be exactly balanced by its inverse process. LTE also assumes that  $T_e = T_R$ , and that the source function is given by a blackbody, i.e.  $S_\nu = B_\nu(T_R)$ . Three *microscopic* requirements of LTE also follow ([Mihalas 1982](#)):

- a) The velocities of the electrons and ions in the plasma obey Maxwellian distributions, such that

$$f(v) = 4\pi \left( \frac{m}{2\pi kT} \right)^{3/2} v^2 \exp \left( -\frac{mv^2}{2kT} \right) \quad (3.9)$$

- b) the ionization state of the plasma is governed by the *Saha equation*, which states that two adjacent ions have relative populations given by

$$\frac{N_{i+1}n_e}{N_i} = \frac{2g_{i+1}}{g_i} \left( \frac{2\pi m_e kT}{h^2} \right)^{3/2} \exp(-h\nu_0/kT) \quad (3.10)$$

- c) the excitation state of the plasma is governed by *Boltzmann statistics*. Two adjacent levels then have relative populations given by

$$\frac{n_j}{n_i} = \frac{g_j}{z_i(T_R)} \exp(-E_j/kT_R), \quad (3.11)$$

Although these three assumptions are often valid, in most astrophysical situations there can be large departures from LTE. A good example of these departures is when the SED is not a blackbody and is affected by absorption – as is the case in AGN and other accreting systems. The Maxwellian assumption is probably the most reliable, but even this may break down when high-energy photons create suprathermal electron distributions ([Humphrey & Binette 2014](#)).

### 3.1.2.1 Dilute approximation

A first step away from LTE is to introduce the dilute approximation. In this case, we relax the assumption that  $T_R = T_e$ , and assume that the mean intensity is given by a dilute blackbody, i.e.

$$J_\nu = WB_\nu(T_R), \quad (3.12)$$

where  $W$  is the dilution factor. We can then approximate the ionization state with a modified Saha equation ([Mazzali & Lucy 1993](#)),

$$\frac{N_{i+1}n_e}{N_i} = W[\xi + W(1 - \xi)] \left(\frac{T_e}{T_R}\right)^{1/2} \left(\frac{N_{i+1}n_e}{N_i}\right)_{T_R}^*, \quad (3.13)$$

where  $\xi$  is the fraction of recombinations that go directly to the ground state. The excitation state can be approximated with a dilute Boltzmann equation

$$\frac{n_{ij}}{n_i} = \frac{Wg_j}{z_i(T_R)} \exp(-E_j/kT_R), \quad (3.14)$$

where  $n_{ij}$  is the population of level  $j$  in ionic stage  $i$ ,  $E_j$  is the energy difference between level  $j$  and the ground state,  $g_j$  is the statistical weight of level  $j$  and  $z_i(T_R)$  is the partition function of ionic stage  $i$ .

### 3.1.3 The Two Level Atom

The two level atom formalism is well described by [Mihalas \(1982\)](#). Let us consider an atomic model consisting of two levels that are linked by radiative and collisional transitions, that can also interact with the continuum. Whilst this model is clearly a simplification, it nonetheless allows for a first step into non-LTE line transfer and proves useful for modelling the resonance lines briefly touched on in chapter 2.

To construct our simple model we must make a few assumptions. The first is the assumption of *statistical equilibrium*. This is the principle that the total rate into a given atomic level/state is equal to the total rate out of said state. This is clearly true whenever the timescale to establish this equilibrium is shorter than the timescale on which the ambient conditions change. The second is the assumption of *complete redistribution (CRD)*, which states that the emission and absorption line profiles are identical for a given transition. This assumption is somewhat analogous to the Sobolev approximation

(see section 3.1.4). These assumptions allow us to formulate rate equations and derive the Einstein relations.

### 3.1.3.1 Einstein coefficients and the two-level atom

Within the two level atom, the rate equation between the two levels in LTE can be written by invoking detailed balance, such that

$$B_{lu}\bar{J}_{ul}n_l = B_{ul}\bar{J}_{ul}n_u + A_{ul}n_u, \quad (3.15)$$

where  $B_{ul}$ ,  $B_{2ul}$  and  $A_{ul}$  are the *Einstein coefficients* for absorption, stimulated emission and spontaneous emission respectively. The ‘mean intensity in the line’,  $\bar{J}_{ul}$ , is given by

$$\bar{J}_{ul} = \int \phi(\nu) J_\nu d\nu. \quad (3.16)$$

In LTE, the level populations obey Boltzmann statistics, and thus we can also write

$$\frac{n_l}{n_u} = \frac{g_l}{g_u} \exp(h\nu_{ul}/k_B T) \quad (3.17)$$

We can then rearrange equation 3.15 in terms of the mean intensity, and use the fact that, in LTE,  $\bar{J}_{ul} = B_\nu(T)$  to write

$$\bar{J}_{ul} = (2h\nu_{ul}^3)/c^2. \quad (3.18)$$

Since this must be true at all values of  $T$  we can also show that

$$A_{ul}/B_{ul} = (2h\nu_{ul}^3) B_{lu}/B_{ul} = g_u/g_l \quad (3.19)$$

### 3.1.4 The Sobolev Approximation

The Sobolev approximation (SA) is a useful limit originally developed. It is used to treat line transfer in fast-moving flows. Originally the theory was mostly applied to Stellar winds, although since then a wide variety of astrophysical objects have been modelled using Sobolev treatments, such as accreting systems (this work) and Supernovae.

The Sobolev limit is when the local bulk velocity gradients in a flow dominate other any thermal broadening. In the presence of these steep velocity gradients, one can assume that the interaction of a ray with a bound-bound transition takes place over a small resonant zone, known as a ‘Sobolev surface’. The length of this zone is defined by

$$l_s = \frac{v_{th}}{dv/ds}. \quad (3.20)$$

It is important that the physical conditions of the  $c$  do not change on this scale. If this is the case, then we can assume that all line interactions for a given frequency will occur at a single ‘resonant’ point. The location at which a given photon will interact with a line of frequency  $\nu_{lu}$  is then given, in velocity space, by

$$v = c \left( \frac{\nu}{\nu_{lu}} + 1 \right). \quad (3.21)$$

The Sobolev optical depth is then

$$d\tau = \frac{\pi e^2}{mc} \left( n_l - n_u \frac{g_l}{g_u} \right) \frac{f_{lu} \lambda_{lu}}{c|dv/ds|}. \quad (3.22)$$

We can see that the physical quantities determining line opacity are therefore the level populations in the plasma, the velocity gradient and the atomic physics associated with the bound-bound transition.

### 3.1.4.1 Escape Probabilities

### 3.1.5 Monte Carlo approaches

Simple radiation transfer problems can be solved analytically, but with more complicated geometries it is necessary to use Monte Carlo techniques, which are easily solved with modern computing approaches and are intuitively parallelisable problems. I will describe one specific Monte Carlo radiative transfer (MCRT) code, which has been used for the majority of the work in this thesis.

## 3.2 PYTHON: A Monte Carlo Ionization and Radiative Transfer Code

PYTHON<sup>1</sup> is a confusingly named Monte Carlo ionization and radiative transfer code. The general philosophy of the code is to be able to produce synthetic spectra for astrophysical objects with outflows in 2.5D, using a self-consistent ionization treatment. The code is written in C, and has been in development since the mid-1990s. Throughout this time it has been used with application to CVs (Long & Knigge 2002; Matthews et al. 2015), YSOs (Sim et al. 2005), Supernovae (Kerzendorf & Sim 2014) and AGN/quasars (Higginbottom et al. 2013, 2014; Matthews et al. 2016). It is also capable of producing spectra for stellar winds and conducting simple photoionization balance calculations for comparison with codes such as CLOUDY. Some more detail on code testing and development can be found in sections 3.9 and 3.10 respectively. Although the operation of PYTHON is well-described by the above authors, it is central to this Thesis and I will thus provide substantial detail on its operation.

### 3.2.1 Basics

PYTHON operates in three distinct stages, shown in figure 3.2. First, the user specifies the photon sources, geometry and kinematics of the system, normally with a similar parameterisation to the SV93 model described in section 2.4. The code can operate with multiple coordinate systems (1D, spherical polar, cylindrical), but in this work I use cylindrical coordinates. In this case, the outflow is discretised into a  $n_x \times n_y$  logarithmic grid with user-specified dimensions. The co-ordinates,  $(x_i, z_i)$ , of the corner of the  $i$ th cell are then given by

$$x_i = L_x 10^{(i-1)\frac{\log(R_{max}/L_x)}{n_x}}, \quad (3.23)$$

$$z_i = L_z 10^{(i-1)\frac{\log(R_{max}/L_z)}{n_z}}, \quad (3.24)$$

where  $L_x$  and  $L_z$  are appropriately chosen (but hardwired) scale lengths. From these co-ordinates the poloidal distance can be calculated and the velocity set according to equation 2.9. The density is then calculated from equation 2.13. An initial temperature,  $T_{init}$  is set by the user. The ionization fractions throughout the wind are then to Saha

---

<sup>1</sup>Named c. 1995, predating the inexorable rise of a certain widely used programming language.

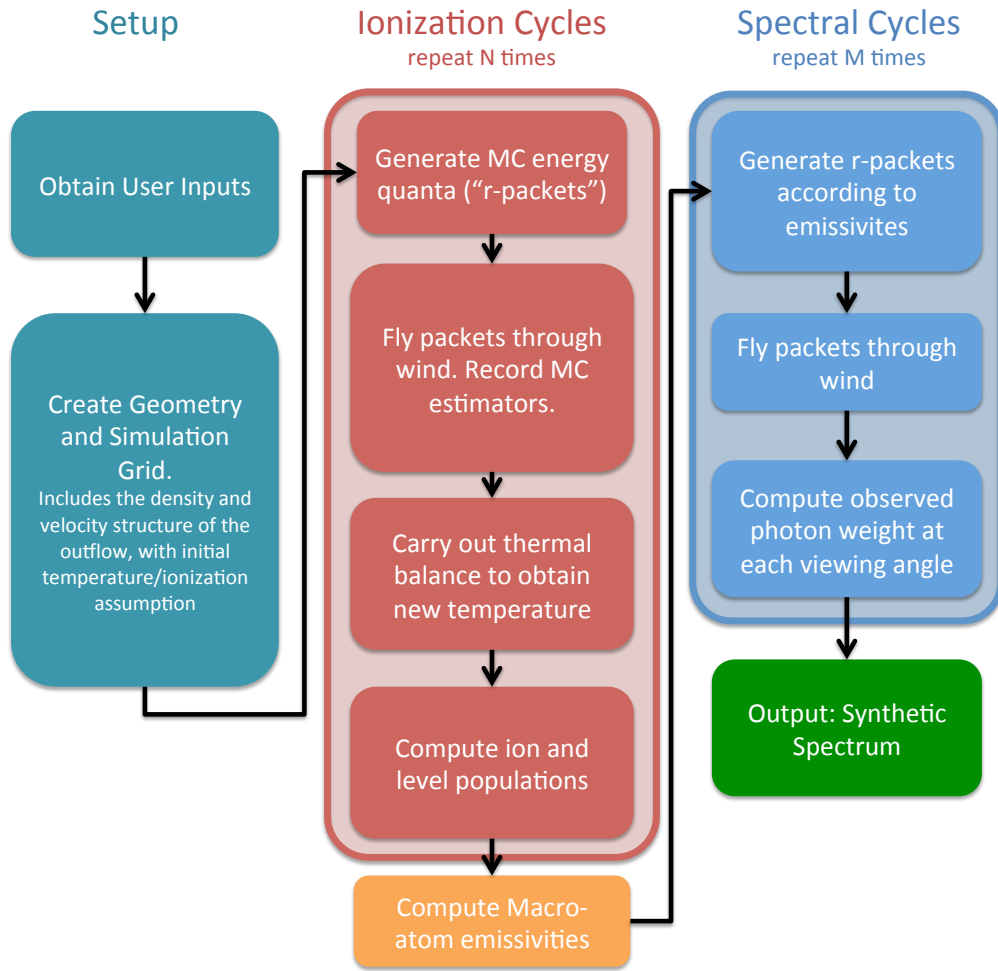


FIGURE 3.2: A flowchart showing the basic operation of PYTHON.

(LTE) abundances at  $T_{init}$ , and the level populations are set according to the Boltzmann formula.

Once the basic setup process has been carried out, the ionization state, level populations and temperature structure are calculated. This is done via an iterative process, by transporting several populations of Monte Carlo energy quanta ('photons' or 'r-packets') through the outflow. This process is repeated until the code converges. In each of these iterations ('ionization cycles'), the code records estimators that characterize the radiation field in each grid cell. At the end of each ionization cycle, a new electron temperature is calculated that more closely balances heating and cooling in the plasma. The radiative estimators and updated electron temperature are then used to revise the ionization state of the wind, and a new ionization cycle is started. The process is repeated until heating and cooling are balanced throughout the wind.

This converged model as the basis for the second set of iterations ('spectral cycles'), in order to compute the synthetic spectrum based on the MC estimators record during the ionization cycles. The emergent spectrum over the desired spectral range is synthesized by tracking populations of energy packets through the wind and computing the emergent spectra at a number of user-specified viewing angles.

### 3.2.2 Radiation Packets

Every energy packet in the simulation starts out as a radiation packet generated from one of  $N_S$  photon sources. To ensure that the frequency distribution of photons is adequately sampled in important frequency regimes, *stratified sampling* is used. A specified fraction,  $f_i$ , of photons must then emerge each band  $i$ , whose frequency boundaries can be adapted for the astrophysical situation considered. The weight,  $w_i$ , of the radiation packets in a given energy band  $i$ , with boundaries  $\nu_i$  and  $\nu_{i+1}$  is then given by

$$w_i = \frac{\sum_j^{N_S} \int_{\nu_i}^{\nu_{i+1}} L_{\nu,j} d\nu}{f_i N_p}, \quad (3.25)$$

where  $N_p$  is the *total* number of photons desired and  $L_{\nu,j}$  is the monochromatic luminosity of photon source  $j$ . The frequency of photons is calculated by constructing a cumulative distribution function (CDF),  $f_{C,i}(\nu)$  from the spectral energy distribution in each band  $i$ :

$$f_{C,i}(\nu) = \frac{\int_{\nu_i}^{\nu} L_{\nu} d\nu}{\int_{\nu_i}^{\nu_{i+1}} L_{\nu} d\nu}. \quad (3.26)$$

A photon frequency can then be generated by cycling through the bands. In each band, a random number is chosen between 0 and 1, and then the frequency is selected by interpolating on the sampled CDF. This process is repeated until each band has the specified number of photons, with the packet weights adjusted accordingly.

PYTHON can operate in two modes concerning the approach to energy packets. In the original mode described by LK02, continuum processes attenuate the weight of the radiation packets. This attenuation is accounted for by including the wind as an additional photon source. In the second mode, energy packets are indivisible and strict radiative equilibrium is enforced. From here on I will only be discussing this indivisible packet scheme, as it is required in order to be able to use macro-atoms to accurately treat recombination in H and He.

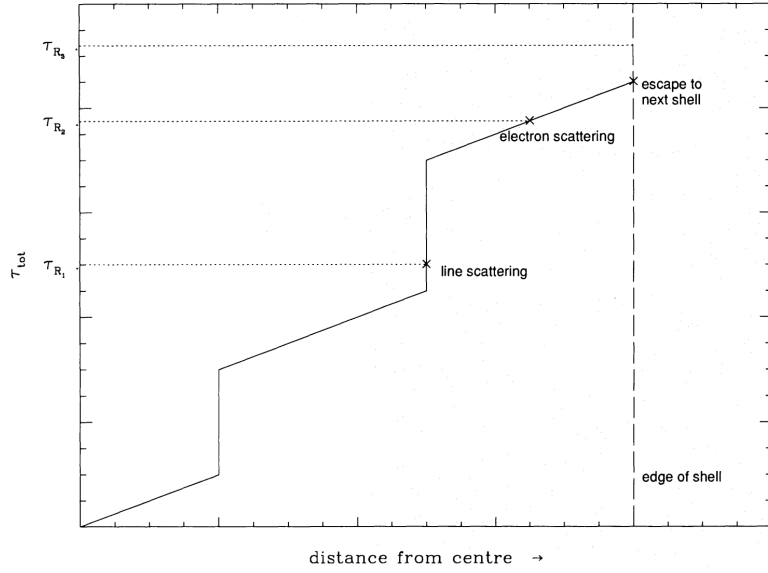


FIGURE 3.3: Credit: Mazzali & Lucy 1993. The process of choosing a scattering location in a cell.

### 3.2.3 Radiative Transfer procedure

As a photon travels through a plasma, it has a finite probability of interacting with the free or bound electrons and undergoing a scattering or absorption event. To deal with this in a Monte Carlo sense, a random optical depth is generated before an  $r$ -packet is moved,

$$\tau_R = -\ln(1 - \mathcal{Z}), \quad (3.27)$$

where  $\mathcal{Z}$  is a random number between 0 and 1. The  $r$ -packet is then gradually transported through a given cell. As it moves, the optical depth,  $\tau'$ , it experiences is incremented continuously, representing continuum processes. When the  $r$ -packet comes into resonance with a line, according to equation 3.21, then the Sobolev optical depth is calculated from equation 3.22 and added to  $\tau'$ . This process is shown in Fig. 3.3, and continues until  $\tau' \geq \tau_R$  or the  $r$ -packet leaves the cell. If the photon leaves the cell then the values of  $\tau_R$  and  $\tau'$  are preserved, and the process continues using the conditions in the new cell. If  $\tau' \geq \tau_R$ , then an interaction with the plasma has occurred, and the process governing this interaction must be identified. This is done by randomly picking an interaction process in proportion with their contributions to  $\tau'$ . If the process is an electron scatter then a new, isotropic direction is generated for the  $r$ -packet. Otherwise, the packet must interact with either the thermal pool or the excitation energy of the plasma.

### 3.3 Macro-atoms

The macro-atom scheme was created by Leon Lucy and is outlined in his 2002/03 papers. It was implemented in PYTHON by Stuart Sim, initially for the study of recombination lines in YSOs ([Sim et al. 2005](#))

[Lucy \(2002, 2003\)](#) has shown that it is possible to calculate the emissivity of a gas in statistical equilibrium without approximation for problems with large departures from LTE. His macro-atom scheme allows for all possible transition paths from a given level, dispensing with the two-level approximation, and provides a full non-LTE solution for the level populations based on Monte Carlo estimators. The macro-atom technique has already been used to model Wolf-Rayet star winds ([Sim 2004](#)), AGN disc winds ([Sim et al. 2008; Tatum et al. 2012](#)), supernovae ([Kromer & Sim 2009; Kerzendorf & Sim 2014](#)) and YSOs (SDL05). A full description of the approach can be found in L02 and L03.

The fundamental approach here requires somewhat of a philosophical shift. Normally MCRT is described in the most intuitive way- that is, we imagine real photons striking atoms and scattering, or photoionizing and depositing energy in a plasma. With Lucy's scheme we should instead reimagine the MC quanta as a packets of quantised energy flow, and the scheme as a *statistical* one. The amount of time a given energy quanta spends in a specific atomic level or thermal pool is then somewhat analogous to the absolute energy contained therein.

Following L02, let us consider an atomic species interacting with a radiation field. If the quantity  $\epsilon_j$  represents the ionization plus excitation energy of a level  $i$  then the rates at which the level  $j$  absorbs and emits radiant energy are given by

$$\dot{A}_j^R = R_{\ell j} \epsilon_{j\ell'} \quad \text{and} \quad \dot{E}_i^R = R_{j\ell'} \epsilon_{j\ell'} , \quad (3.28)$$

Where I have adopted Lucy's convention in which the subscript  $\ell'$  denotes a summation over all lower states ( $\ell' < j$ ), and  $u'$  will thus denote a summation over all states ( $u' > j$ ). Similarly, the rates corresponding to *kinetic* (collisional) energy transport can then be written as

$$\dot{A}_j^C = C_{\ell'j}\epsilon_{j\ell'} \quad \text{and} \quad \dot{E}_j^C = C_{j\ell'}\epsilon_{j\ell'} \quad , \quad (3.29)$$

If we now impose statistical equilibrium

$$(\mathcal{R}_{\ell'j} - \mathcal{R}_{j\ell}) + (\mathcal{R}_{uj} - \mathcal{R}_{ju}) = 0 \quad . \quad (3.30)$$

we can then obtain

$$\begin{aligned} & \dot{E}_j^R + \dot{E}_j^C + \mathcal{R}_{ju'}\epsilon_j + \mathcal{R}_{j\ell}\epsilon_{\ell'} \\ &= \dot{A}_j^R + \dot{A}_j^C + \mathcal{R}_{u'j}\epsilon_j + \mathcal{R}_{\ell'j}\epsilon_{\ell'}. \end{aligned} \quad (3.31)$$

This equation is the starting point for the macro-atom scheme. It shows that, when assuming only radiative equilibrium, the energy flows through a system depend only on the transition probabilities and atomic physics associated with the levels the energy flow interacts with. By quantising this energy flow into radiant ( $r$ -) and kinetic ( $k$ -) packets, we can simulate the energy transport through a plasma discretised into volume elements (“macro-atoms”), whose associated transition probabilities govern the interaction of radiant and kinetic energy with the ionization and excitation energy associated with the ions of the plasma.

Although equation 3.31 assumes strict radiative equilibrium, it is trivial to adjust it to include non-radiative source and sink terms. For example, in an expanding parcel of plasma, adiabatic cooling may be included with a simple modification to the RHS of equation 3.31.

### 3.3.1 Transition Probabilities

Having interpreted equation 3.31 in a *stochastic* way, we can now construct our Monte Carlo scheme, following Lucy (2002). A macro-atom in state  $j$  always has a finite probability of deactivating radiatively or collisionally:

$$p_j^R = \dot{E}_j^R/D_j \quad \text{and} \quad p_j^C = \dot{E}_j^C/D_j, \quad (3.32)$$

where I have defined

$$D_j = \dot{E}_j^R + \dot{E}_j^C + \mathcal{R}_{ju'}\epsilon_j + \mathcal{R}_{j\ell'}\epsilon_{\ell'} = (\mathcal{R}_{j\ell'} + \mathcal{R}_{ju'})\epsilon_j. \quad (3.33)$$

The corresponding jumping probabilities, which describe the probability that the macro-atom transitions to a different state while remaining active, are given by

$$p_{ju'} = \mathcal{R}_{ju'}\epsilon_j/D_j \quad \text{and} \quad p_{j\ell'} = \mathcal{R}_{j\ell'}\epsilon_{\ell'}/D_j. \quad (3.34)$$

Note that the jumping probability is always proportional to the energy of the lower level, whereas the emission probability is proportional to the energy *difference* between the levels, as  $\dot{E}_j^R = R_{j\ell'}(\epsilon_j - \epsilon_{\ell'})$ . We can also trivially show that the probabilities are correctly normalised, as

$$\begin{aligned} p_j^R + p_j^C + p_{j\ell'} + p_{ju'} &= (1/D_j)(\mathcal{R}_{ju'}\epsilon_j + \mathcal{R}_{j\ell'}\epsilon_{\ell'} + \dot{E}_j^R + \dot{E}_j^C) \\ &= 1. \end{aligned} \quad (3.35)$$

With these transition probabilities identified, a Monte Carlo calculation can proceed by formulating the normal statistical equilibrium rate equations that will depend on the ambient conditions of the plasma. The effect of these ambient conditions is expressed through the use of Monte Carlo *estimators*.

### 3.3.2 Rate equations

The macroscopic transition probabilities above depend on the traditional rate equations formulated according to statistical equilibrium. In the framework of the Sobolev escape probability formalism (Rybicki & Hummer 1978; L02; Sim 2004), the bound-bound excitation rate,  $\mathcal{R}_{lu}$ , in an ion is given by

$$\mathcal{R}_{lu} = B_{lu}n_l J_{est} + q_{lu}n_l n_e, \quad (3.36)$$

where  $u$  and  $l$  denote the upper and lower levels and  $q_{lu}$  is the collisional rate coefficient (see section 3.3.2.1).  $J_{est}$  is the Monte Carlo estimator for the mean intensity impinging on the Sobolev region, weighted by an angle-dependent escape probability, given by (Sim

2004)

$$J_{est} = \frac{c}{4\pi\nu_0 V} \sum_i w_i \frac{1 - e^{-\tau_{s,i}}}{\tau_{s,i}} \frac{1}{(dv/ds)_i}. \quad (3.37)$$

Here  $w$  is the photon weight (in luminosity units),  $\nu_0$  is the line frequency,  $dv/ds$  is the velocity gradient and  $\tau_s$  is the Sobolev optical depth. The sum is over all photons that come into resonance with the line, and thus represents an integral over solid angle. This is essentially the MC estimator form of  $\bar{J}_{ul}$ , and differs from the  $J_{ji}^b$  quantity in equation (20) of Lucy (2002) as there is no assumption of homologous flow or symmetric escape probabilities. The corresponding de-excitation rate is then

$$\mathcal{R}_{ul} = \beta_{lu} A_{ul} n_u + B_{ul} n_u J_{est} + q_{ul} n_u n_e. \quad (3.38)$$

The photoionization and collisional ionization rates between a lower level,  $l$ , and the continuum (or, in the case of ions with more than one bound electron, the ground state of the upper ion),  $\kappa$ , are

$$\mathcal{R}_{jk\kappa} = n_l \gamma_{l\kappa} + q_{l\kappa} n_l n_e. \quad (3.39)$$

Here,  $\sigma_\nu$  is the photoionization cross section, and  $J_\nu$  is the mean intensity.  $\gamma_{l\kappa}$ , the photoionization rate from  $l \rightarrow \kappa$ , is

$$\gamma_{l\kappa} = \int_{\nu_0}^{\infty} \frac{4\pi J_\nu \sigma_\nu}{h\nu} d\nu. \quad (3.40)$$

The corresponding recombination rate is given by

$$\mathcal{R}_{\kappa l} = \alpha_{\kappa l} n_\kappa n_e + q_{\kappa l} n_\kappa n_e, \quad (3.41)$$

where  $\alpha_{\kappa l}$  is the radiative recombination coefficient to level  $l$ , and is given by

$$\alpha_{\kappa l} = 4\pi \Phi_{l\kappa}^* \int_{\nu_0}^{\infty} \frac{\sigma_\nu}{h\nu} \frac{2h\nu^3}{c^2} \exp\left(\frac{-h\nu}{kT_e}\right) d\nu. \quad (3.42)$$

This treatment means that radiative and collisional rates to and from all levels are considered when calculating both the ionization state and the level populations, although we neglect ionization directly to excited levels of the upper ion.

### 3.3.2.1 Collision strengths

The bound-bound collisional rate coefficient  $q_{lu}$  is calculated from the [van Regemorter \(1962\)](#) approximation, given by

$$q_{lu} = 2.388 \times 10^{-6} \lambda_{ul}^3 A_{ul} g_u \bar{g} \quad (3.43)$$

and the inverse rate can just be calculated by considering detailed balance, such that

$$q_{ul} = q_{lu} \frac{g_u}{g_l} \exp\left(\frac{h\nu_{ul}}{kT_e}\right) \quad (3.44)$$

Using equation 3.43 means that collisions between radiatively forbidden transitions are not taken into account when one splits levels into  $l$ - and  $s$ -subshells, as well as principal quantum number,  $n$  (as we have done with He I; see section ??). Although this approximation is, in general, a poor one, the effect is second order in the physical regime where recombination lines are formed in our models. This is because bound-free processes are dominant in determining level populations and emissivities. We have verified that this is indeed the case in the He I emission regions in our models.

The bound-free collision strengths are calculated using equation (5.79) of [Mihalas \(1982\)](#).

The collisional ionization rate is

$$q_{lk} = 1.55 \times 10^{-13} n_e \bar{g}_i \sigma_{\nu_0} \frac{h\nu_0}{kT_e^{3/2}} \exp\left(\frac{-h\nu_{ul}}{kT_e}\right), \quad (3.45)$$

where  $\sigma_{\nu_0}$  is the photoionization cross-section at the threshold energy.  $\bar{g}_i$  is an effective gaunt factor for ion  $i$  and is approximately equal to 0.1, 0.2, 0.3 for  $Z = 1, 2$  and  $> 2$  respectively, where  $Z$  is the atomic number. The collisional (three-body) recombination rate is found using the Saha equation and given by

$$q_{kl} = q_{lk} \frac{n_l^*}{n_e^* n_k^*}, \quad (3.46)$$

For numerical reasons, the above two expressions are combined in PYTHON where possible, to avoid multiplying two exponentials together.

### 3.3.3 Macro-atom estimators

The heating and cooling rates for macro-atom bound-bound transitions are the rates of collisional excitations and de-excitations - i.e. the rate at which thermal energy is converted into bound-bound excitation energy and vice versa.

$$C_{bb} = \sum_{lines} q_{lu} n_l n_e h \nu_{ul} V \quad (3.47)$$

$$H_{bb} = \sum_{lines} q_{ul} n_u n_e h \nu_{ul} V \quad (3.48)$$

For bound-free transitions, we define the normal photoionization and recombination rate coefficients  $\gamma$  and  $\alpha$ , where  $\alpha$  includes stimulated recombination as we do in the code. Note this differs to the approach in Lucy (2003), where it is instead included as a negative photoionization term, hence the notation  $\tilde{\gamma}$ . We also need to define two ‘modified rate coefficients’ which are the rates at which b-f transitions add and remove energy to the radiation field. These are denoted  $\gamma^E$  and  $\alpha^E$ , and given by

$$\gamma^E = \sum_i^{photons} \frac{w_i ds \sigma_{\nu_0}}{h \nu V} \quad (3.49)$$

$$\alpha^E = 4\pi \Phi_{i\kappa}^* \int_{\nu_0}^{\infty} \frac{\sigma_{\nu}}{h \nu_0} \frac{2h\nu^3}{c^2} \exp\left(\frac{-h\nu}{kT_e}\right) d\nu \quad (3.50)$$

$$\alpha_{st}^E = . \quad (3.51)$$

The rate at which recombinations convert thermal *and* ionization energy into radiant energy is then  $\alpha^E h \nu_{kl} n_{\kappa} n_e$ , where  $h \nu_{kl}$  is the potential of the b-f transition, or the energy difference between continuum  $\kappa$  and the level  $l$  we are recombining too. The amount of this energy which is removed from the actual thermal pool therefore needs a quantity  $\alpha h \nu_{kl} n_{\kappa} n_e$  subtracted from it, giving

$$C_{bf} = \sum_{bfjumps} (\alpha^E - \alpha) n_e n_{\kappa} \nu_{kl} V \quad (3.52)$$

where here I have also included stimulated recombination as we do in the code. Note this differs to the approach in Lucy (2003), where it is instead included as a negative photoionization term, hence the notation  $\tilde{\gamma}$ . For photoionizations, we write a similar expression. The rate at which a level  $l$  absorbs energy by b-f transitions is given by  $\gamma^E h\nu_{kl} n_\kappa n_e$ , but the amount  $\gamma h\nu_{kl} n_l$  goes into ionization energy, giving

$$H_{bf} = \sum_{bf\ jumps} (\gamma^E - \gamma) n_l h\nu_{kl} V \quad (3.53)$$

as the rate at which radiant energy heats the plasma via b-f transitions.

### 3.3.4 $k$ -packets

$k$ -packets represent quantised kinetic or thermal energy, and any interaction chain involving a  $k$ -packet thus represents interaction with the thermal pool of ions and electrons.  $k$ -packets can be produced either directly via a continuum heating process ( $r \rightarrow k$ ), or by the collisional de-activation of a macro-atom ( $r \dots \rightarrow A^* \rightarrow k$ ) according to equation 3.32.

Once they are produced,  $k$ -packets never move, as they represent the quantised thermal energy flow in a finite volume element. Hence, when they are produced, their destruction path is decided according to the different cooling mechanisms in the plasma. A  $k$ -packet then has a probability of being destroyed by process  $i$  of

$$p_{i,destruct} = C_i / (C_{bf} + C_{ff} + C_{bb} + C_{comp} + C_a). \quad (3.54)$$

### 3.3.5 Putting it all together

### 3.3.6 Ionization Fractions and Level Populations

In section 3.1.2 I described how it is possible to calculate the ionization and excitation of a plasma under LTE or dilute approximations. Macro-atoms are not approximated – their level and ion populations are calculated by solving the rate equations formulated in section ???. This is done via matrix inversion. For an element with  $n$  ions and  $m_i$  levels in each ion, we construct a square matrix with dimensions  $m = \sum_i^n m_i$ . This element then has a total number density of  $N_{elem} = \sum_i^n N_i$ . To turn the system of rate equations

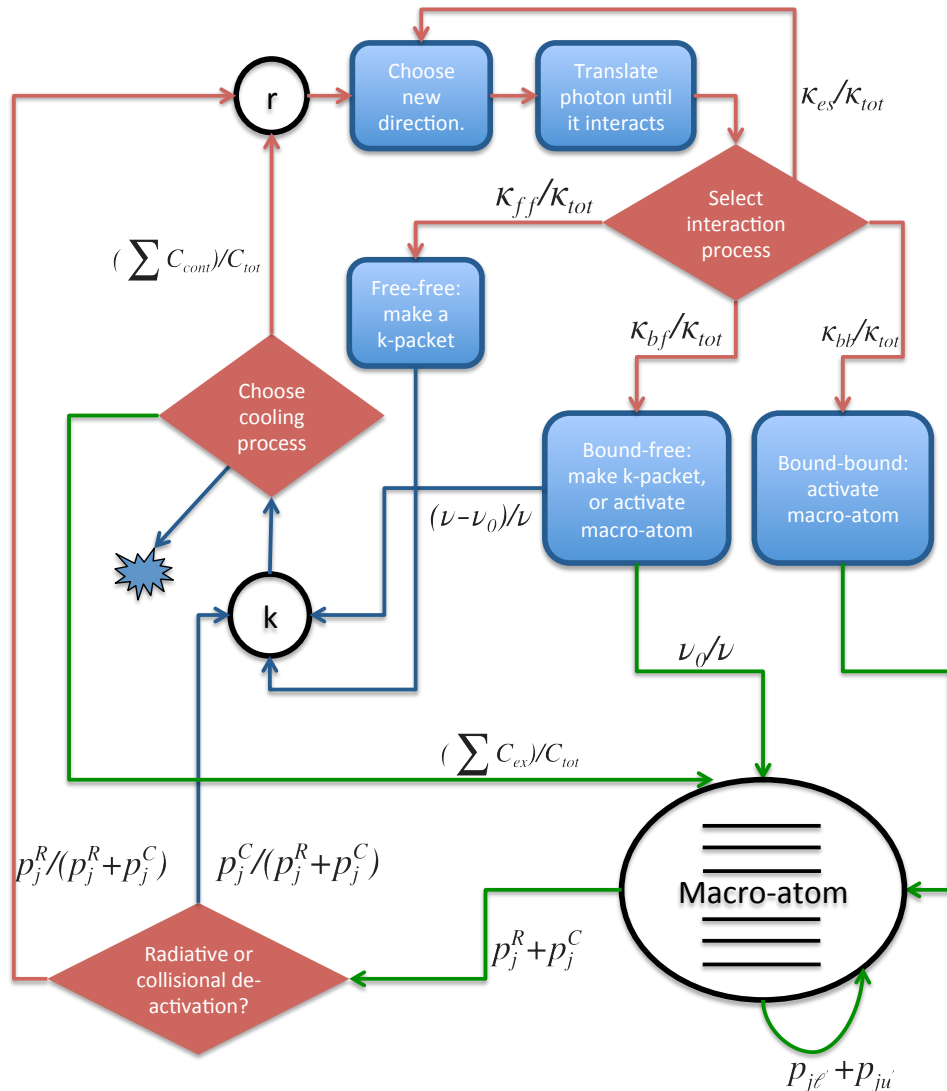


FIGURE 3.4: The decision tree traversed by an energy packet in macro-atom mode, depicting the interaction between radiation ( $r$ -packets), the thermal pool ( $k$ -packets), and ionization and ionization/excitation energy (macro-atoms). The probabilities at each decision point are marked, and are defined in the text. The red, blue and green coloured arrows represent radiant, kinetic and ionization/excitation energy respectively.

for this element into matrix form, we populate the  $j$ th diagonal of the matrix with the negative of the rate out of level  $j$ ,  $-(\mathcal{R}_{j\ell'} + \mathcal{R}_{ju'})$ , and populate the off-diagonals  $(j, k)$  with the positive rate  $\mathcal{R}_{jk}$ . These are then multiplied by a vector of the fractional level populations, and must equal a vector of zeros, due to statistical equilibrium. Our matrix equation is then

$$\begin{bmatrix} -\mathcal{R}_{1u'} & \mathcal{R}_{21} & \mathcal{R}_{31} & \dots & \mathcal{R}_{m1} \\ \mathcal{R}_{12} & -(\mathcal{R}_{2\ell'} + \mathcal{R}_{2u'}) & \mathcal{R}_{32} & \dots & \mathcal{R}_{m2} \\ \mathcal{R}_{13} & \mathcal{R}_{23} & -(\mathcal{R}_{3\ell'} + \mathcal{R}_{3u'}) & \dots & \mathcal{R}_{m3} \\ \vdots & \vdots & \vdots & \ddots & \vdots \\ \mathcal{R}_{1m} & \mathcal{R}_{2m} & \mathcal{R}_{3m} & \dots & -\mathcal{R}_{m\ell'} \end{bmatrix} \begin{bmatrix} n_1/N_{elem} \\ n_2/N_{elem} \\ n_3/N_{elem} \\ \vdots \\ n_m/N_{elem} \end{bmatrix} = \begin{bmatrix} 0 \\ 0 \\ 0 \\ \vdots \\ 0 \end{bmatrix}. \quad (3.55)$$

This problem is not yet soluble, as a valid solution is that all levels could simply have occupation numbers of 0. To close the problem, we must impose the boundary condition, that the sum of the fractional populations is 1, i.e.

$$\sum_i \frac{N_i}{N_{elem}} = 1. \quad (3.56)$$

In matrix form, this is equivalent to replacing the entire first row of the rate matrix with 1, and the first entry of the RHS vector with a 1, so that we have

$$\begin{bmatrix} 1 & 1 & 1 & \dots & 1 \\ \mathcal{R}_{12} & -(\mathcal{R}_{2\ell'} + \mathcal{R}_{2u'}) & \mathcal{R}_{32} & \dots & \mathcal{R}_{m2} \\ \mathcal{R}_{13} & \mathcal{R}_{23} & -(\mathcal{R}_{3\ell'} + \mathcal{R}_{3u'}) & \dots & \mathcal{R}_{m3} \\ \vdots & \vdots & \vdots & \ddots & \vdots \\ \mathcal{R}_{1m} & \mathcal{R}_{2m} & \mathcal{R}_{3m} & \dots & -\mathcal{R}_{m\ell'} \end{bmatrix} \begin{bmatrix} n_1 \\ n_2 \\ n_3 \\ \vdots \\ n_m \end{bmatrix} = \begin{bmatrix} 1 \\ 0 \\ 0 \\ \vdots \\ 0 \end{bmatrix}. \quad (3.57)$$

This matrix equation can now be solved. To do the actual matrix manipulation, the code uses the GNU scientific libraries (GSL; [Gough 2009](#)) implementation of LU decomposition ([Turing 1948](#)). This is a fast and reliable way of inverting large matrices that includes error handling and enables checking of, for example, singular rate matrices.

### 3.4 A hybrid line transfer scheme: including simple-atoms

I have now described in detail how the macro-atom approach is implemented in PYTHON. A pure macro-atom approach can be easily used for some situations – for example, in the YSO application described by Sim et al. (2005), which uses a H-only model. However, in accretion disc winds the densities can be very high and higher  $Z$  elements must be included. To include all these elements as macro-atoms is not currently computationally feasible in PYTHON for anything but the simplest models. I will thus describe a ‘hybrid scheme’, which treats H and He under the macro-atom approach but models all other atoms as ‘simple-atoms’.

#### 3.4.1 Line Transfer

Simple-atoms still interact with  $r$ - and  $k$ -packets, but do not possess internal transition probabilities. As a result, they are analogous to the two-level atom treatment, as any excitation is immediately followed by a deactivation into an  $r$ - or  $k$ -packet. This hybrid approach allows us to preserve the fast treatment of, for example, UV resonance lines, while accurately modelling the recombination cascades that populate the levels responsible for H and He line emission. As a result of this hybrid scheme, a separate set of estimators must be recorded, and the ionization and excitation of the plasma is calculated in a different manner.

In order to include simple-atoms, we must add in a few extra pathways to Fig. 3.4, so that energy packets can also undergo excite simple-atoms, through either bound-free or bound-bound processes. This is done in proportion with the simple-atom opacities.

This approach does necessitate a few approximations.

#### 3.4.2 Estimators

In simple-ions it is in some ways a little more complicated. First we define  $q$  which will be different for each b-b transition, following Nick’s thesis, which is given by (NB: I don’t actually know how to derive this)

$$q = \frac{q_{ul}n_e(1 - e^{-h\nu/kT_e})}{\beta_{ul}A_{ul} + q_{ul}n_e(1 - e^{-h\nu/kT_e})} \quad (3.58)$$

where  $\beta_{ul}$  is the angle-averaged escape probability.  $q$  represents *the probability that an excited bound electron will collisionally de-excite*. Our b-b heating rate is computed during the photon propagation and is a sum over photons which come into resonance with each line, given by

$$H_{bb, simple} = \sum_{photons} \sum_{lines} (1 - q)(1 - e^{-\tau_s}) w_{photon} \quad (3.59)$$

And our bound bound cooling rate is given by

$$C_{bb, simple} = \sum_{lines} q \left( n_l \frac{g_u}{g_l} - n_u \right) q_{ul} n_e \frac{(1 - e^{-h\nu/kT_e})}{(e^{h\nu/kT_e} - 1)} h\nu_{ul} \quad (3.60)$$

The bound-free heating rate is given by

$$H_{bf, simple} = \sum_{photons} \sum_{bf jumps} w_{photon} e^{-\tau} \frac{\nu - \nu_0}{\nu} \quad (3.61)$$

where  $\nu$  here is the frequency of the photon in question, and  $\nu_0$ . The bound-free cooling rate is then

$$C_{bf, simple} = ?? \quad (3.62)$$

### 3.4.3 Ionization and Excitation

## 3.5 Heating And Cooling Balance

I have already given the estimators used to calculate heating and cooling rates in the plasma. These are not only used in the creation and elimination of  $k$ -packets, but also in the heating and cooling balance carried out in PYTHON to achieve a self-consistent temperature structure in the wind.

At the end of each ionization cycle, the code has stored a new set of MC estimators for radiative heating of the plasma. We then assume that each cell is in thermal equilibrium then the appropriate electron temperature is simply the value of  $T_e$  that is a solution to the equation

$$H_{tot} - C_{tot}(T_e) = 0, \quad (3.63)$$

where  $H_{tot}$  and  $C_{tot}$  are the total heating and cooling rates in the plasma. A number of checks are in place to ensure numerical stability, namely a maximum temperature and a maximum change in temperature from cycle to cycle. This is especially important in cases where the initial guess at wind temperature is far from the true value.

### 3.5.1 Convergence

PYTHON always runs a fixed number of ionization cycles, rather than terminating when a convergence criterion is reached. As a result, it is up to the user to check that the simulation is converged. An individual cell is considered converged when a) the temperature stops changing significantly, i.e. both  $T_R$  and  $T_e$  satisfy

$$\frac{|T_{new} - T_{old}|}{T_{new} + T_{old}} < 0.05, \quad (3.64)$$

and b) the heating and cooling rates are well balanced such that

$$\frac{|H_{tot} - C_{tot}|}{H_{tot} + C_{tot}} < 0.05. \quad (3.65)$$

These criteria could doubtless be improved, but they are nonetheless a good way of ensuring that thermal and radiative equilibrium holds in the plasma. An example of how the average temperature and fraction of converged cells changes over the course of the ionization cycles in a typical CV model is shown in Fig. 3.5.

## 3.6 Spectral Cycles

The primary output from PYTHON is a synthetic spectrum across a range of viewing angles. The code utilises a variance reduction technique in order to minimise the amount of time spent in the portion of the code. This technique is based on a similar method implemented by (Woods 1991).

A comparison between the two methods is shown in figure 3.6.

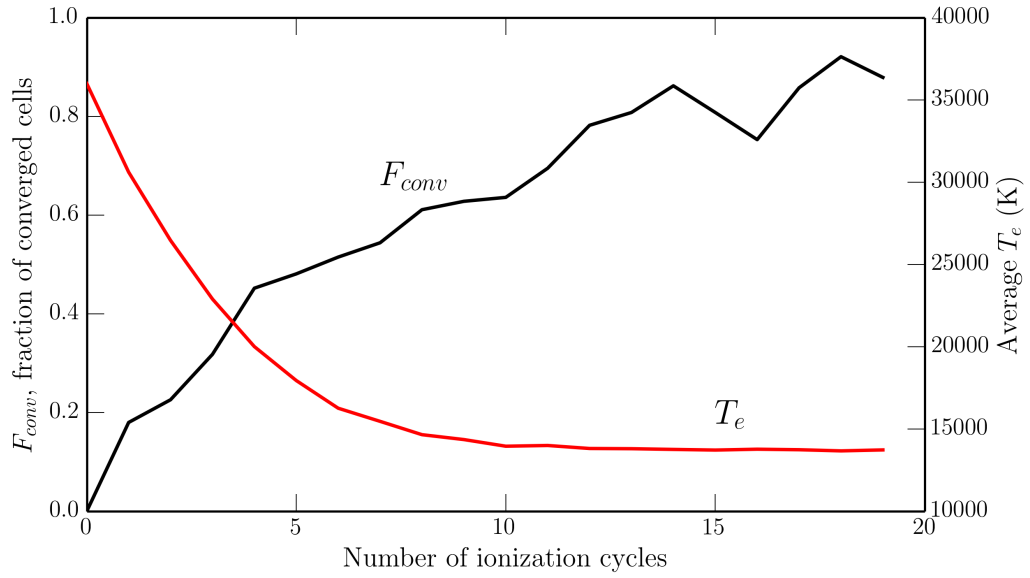


FIGURE 3.5: The average temperature and fraction of converged cells in a typical CV model, shown as a function of the number of ionization cycles completed.

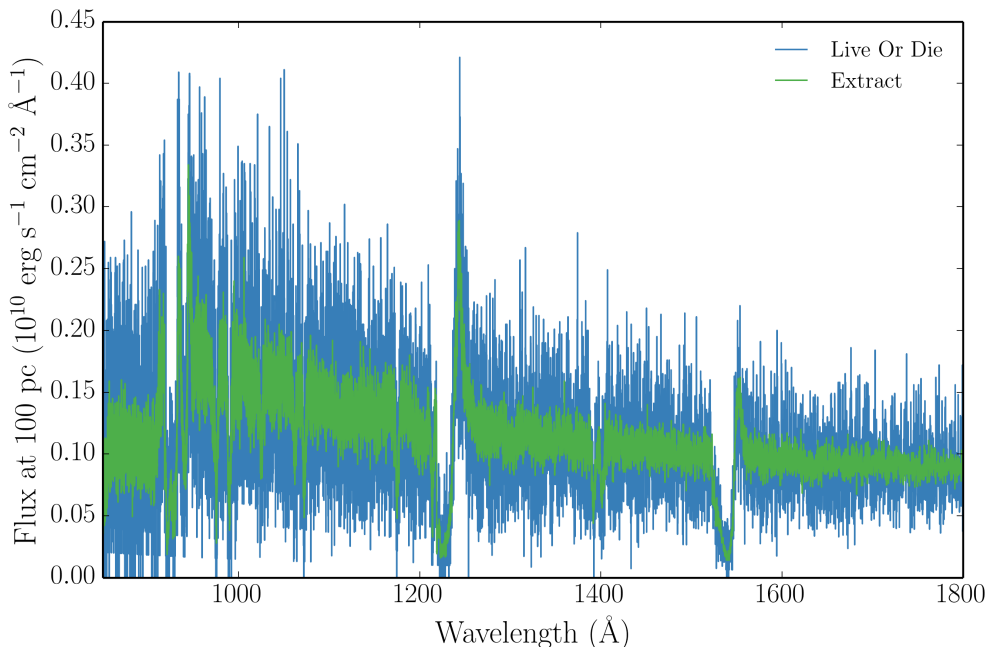


FIGURE 3.6: A Synthetic spectrum after 30 spectral cycles with 100,000 photons from simple CV wind model at a 60° viewing angle. Spectra produced with both the extract and live or die modes are shown. The effectiveness of the extract variance reduction technique can be clearly seen, and we can see that the spectral shape is unaltered.

## 3.7 Atomic Data

One of the big challenges in building reliable photoionization and radiative transfer lies in the acquisition of accurate and complete atomic datasets. All of the rates described so far contain a term, such as the oscillator strength or dimensionless collision strength, that is dependent purely on the atomic physics associated with the transition. These quantities can be measured in laboratory experiments, or predicted from atomic structure codes which derive the atomic physics from quantum theory.

Photoionization cross-sections are obtained from two sources. Where possible, we use TOPBASE photoionization cross-sections. For macro-atoms, these cross-sections are partial and represent the cross-section for a photoionization from a given *level*. We neglect photoionizations to excited configurations of the upper ion. For simple-atoms they are from the ground state. The TOPBASE cross-sections have two major drawbacks in that

## 3.8 Clumping

### 3.8.1 Motivation

As described in section ??, observational evidence for inhomogeneities in outflows is widespread. Clumping a plasma can have a significant effect on its ionization, emission and absorption characteristics. Clearly, the interplay between these effects will be somewhat complex

A number of different implementations of clumping have been explored in previous studies, mostly in the stellar winds community. Perhaps the simplest method is when one assumes that the individual clumps are both optically and geometrically thin; this is known as *microclumping* (e.g. Hamann & Koesterke 1998; Hillier & Miller 1999; Hamann et al. 2008). This technique has been particularly successful in reconciling discrepant mass-loss estimates. It was found that one would obtain different mass-loss rates depending on whether they were calculated from (i) UV resonance scattering of continuum photons (which scales linearly with density; a ‘ $\rho$ -diagnostic’) or (ii) recombination and free-free emission process (which scale with the square of density; ‘ $\rho^2$ -diagnostics’). A

clumped outflow would have enhanced densities in certain regions, and would thus mean that  $\rho^2$ -diagnostics tend to overestimate the total mass-loss rates. Microclumping has helped verify this hypothesis with radiative transfer modelling (REFs). These clumpy models also provide better fits to the electron scattering wings of emission lines in stellar winds (?).

The second-generation of stellar wind codes went on step further by addressing the issue of *porosity*; that clumps will have a finite size, and thus gaps between the clumps may affect the emergent radiation field. This approach is known as *macroclumping*.

### Describe macroclumping with references.

Implementing a treatment of clumping in accretion disc wind models is challenging, for two main reasons. First, the physical scale lengths and density contrasts in disc winds are not well-constrained from observations, especially in AGN. Second, there are significant computational difficulties associated with adequately resolving and realistically modelling a series of small scale, high density regions with a MCRT code. Given the lack of knowledge about the actual type of clumping, we incorporated the simpler microclumping approach into our code. This is partly because our primary concern was the ionization and emission characteristics of the flow, and porosity was a secondary concern.

### 3.8.2 Microclumping

To take account of clumping in our outflow we adopt a simple parameterization used in stellar wind modelling. The key assumption here is that typical clump sizes are much smaller than the typical photon mean free path, and thus the clumps are both geometrically and optically thin. This approach is typically known as microclumping and allows one to introduce a ‘filling factor’,  $f$ , which is the fraction of the volume of the plasma filled by clumps. We can then introduce the ‘density enhancement’,  $D$ , which is simply

$$D = \frac{1}{f} \quad (3.66)$$

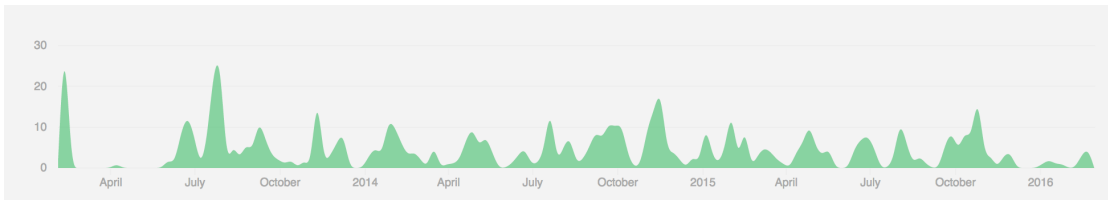


FIGURE 3.7: Commit history from Feb 3, 2013 to Feb 29, 2016, showing the regular code development that makes version control such a necessity to a collaborative code project. Produced using the Github API and plotting capability.

The densities in the model are then multiplied by this factor. This has the effect of enhancing ‘ $\rho^2$ ’ processes such as recombination or collisional excitation, and

### 3.9 Code Validation

The main challenge for high performance scientific computing can be elegantly summarised by Ferland’s (2002) epitaph, ‘*Reliability in the face of complexity*’. I have already delved into some of the complexity in this case, so it is important to assess whether the code is also reliable before I present results.

#### 3.9.1 Testing against Cloudy

#### 3.9.2 Testing against Tardis

### 3.10 Code Maintenance and Version Control

As part of the expansion of the team working on PYTHON I was responsible for bringing the code under the auspices of a robust version control system. Thanks to these efforts, the code is now hosted on GitHub at <https://github.com/agnwinds/python/>. Our team uses a Pull & Fork model for collaborative code development, in which major changes are made in a forked repository before the developer submits a ‘Pull request’ to the main repository. To test the code, we use a combination of Travis CI build tests – run per commit to the upstream repo – and our own test suite which is run every night on a multi-core server.

#### 3.10.1 Parallelisation

## Chapter 4

# Quasar Emission Line Equivalent Widths as Probes of Orientation and Unification

### 4.1 Data Sample

To construct our sample, we start with the the Shen et al. (2010; hereafter S10) catalog of 105,783 quasars from the The Sloan Digital Sky Survey (SDSS) DR7. As we will use emission line diagnostics in this study, we must further divide this sample according

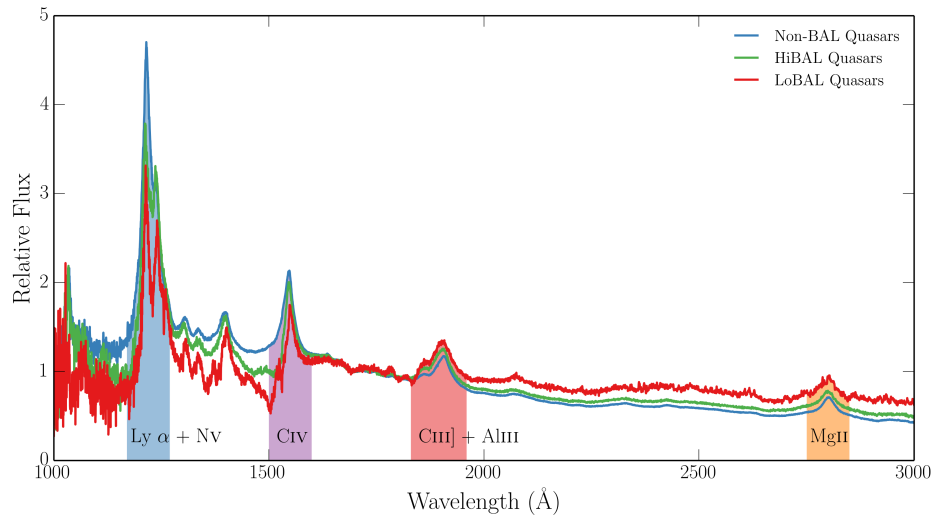


FIGURE 4.1: SDSS Composite spectra

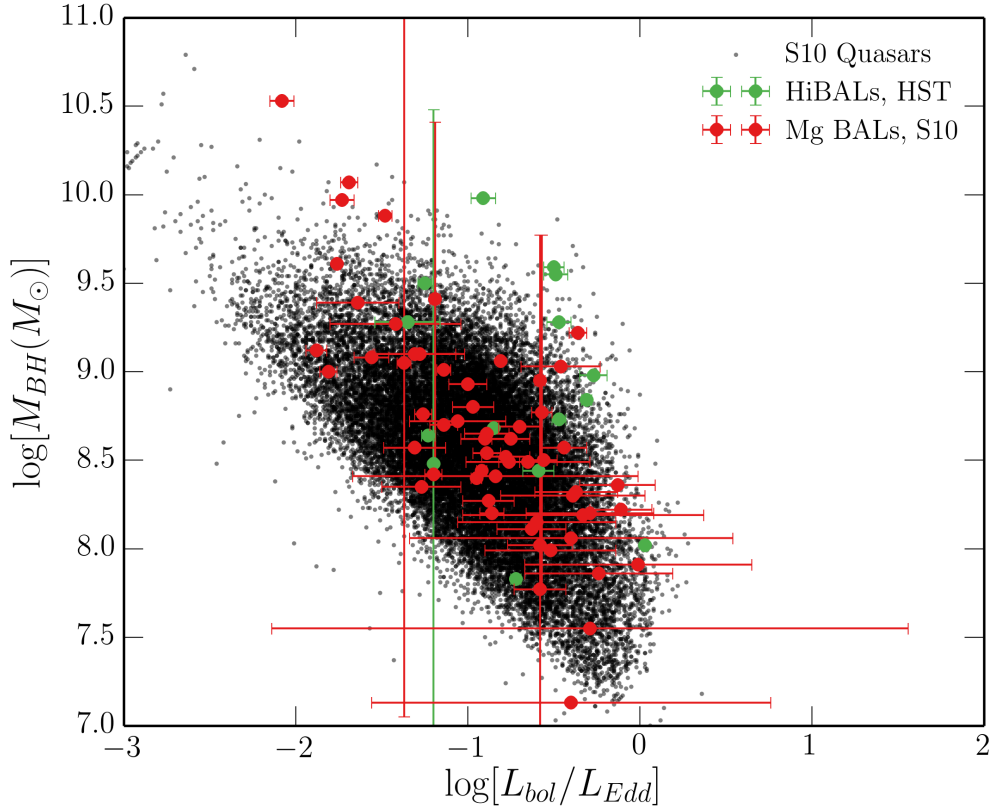


FIGURE 4.2: BH mass and Eddington fraction for the BAL samples plotted over the overall quasar sample from S10.

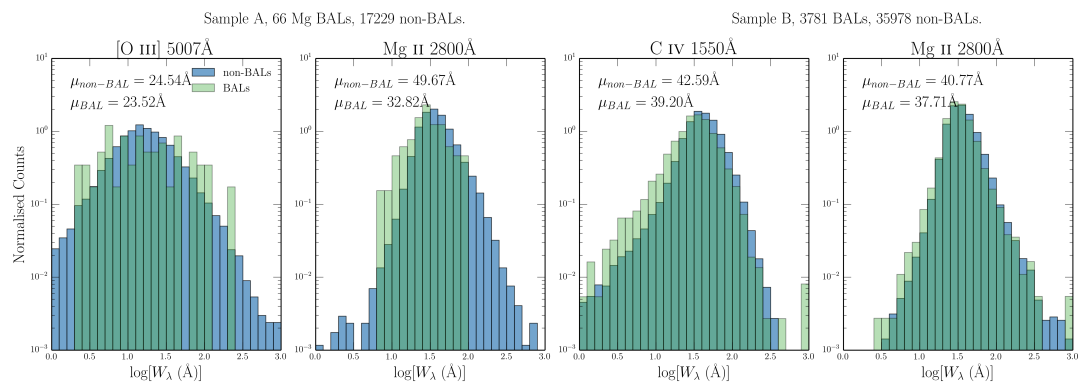


FIGURE 4.3: Histograms of equivalent widths for three emission lines from the two different samples.

to which emission lines are present in the SDSS wavelength range at a given redshift. Sample A contains all quasars within the redshift range  $0.35 < z < 0.83$ , such that the Mg II 2800A and OIII 5007A line EWs are both measured, and Mg II BAL identification is possible. Sample B contains all quasars within the redshift range  $1.45 < z < 2.28$ , such that the EWs and presence of BALs in Mg II 2800A and CIV 1550A are both measurable. The details of these samples are shown in table 1.

In attempting to draw broad conclusions about unification models as a whole, we would like to be able to construct a large homogenous dataset of *HiBAL* and non-BAL quasars with both OIII 5007A EWs. Unfortunately, the wavelength limits of SDSS do not allow this. One of the problems with using just LoBAL quasars as tests of unification is that there is evidence that they are drawn from a different population than normal quasars, perhaps suggesting an *evolutionary* origin. Examples include anomalously high LoBAL fractions in dust-reddened quasar samples ([Urrutia et al. 2009](#)) and infra-red selected samples ([Dai et al. 2012](#)); although see also [Lazarova et al. \(2012\)](#). To partially address this issue, we also build a small sample of HiBAL quasars in SDSS by cross-matching the S10 catalog with BALs identified in the HST COS archive. BALs were selected from the COS spectra using the balnicity index (Weymann et al. 1991),  $BI$ , defined as

$$BI = \int_{3000 \text{ km s}^{-1}}^{25000 \text{ km s}^{-1}} C \left( 1 - \frac{f(v)}{0.9} \right) dv. \quad (4.1)$$

The constant  $C = 0$  everywhere, unless the normalized flux has satisfied  $f(v) < 0.9$  continuously for at least  $2000 \text{ km s}^1$ , whereby  $C$  is set to 1. HST objects were designated as HiBALS by satisfying the condition that  $BI > 0$  in one of CIV, NV, SiIV. The mass and Eddington fraction measurements from S10, with errorbars, are shown against the background distribution of all quasars.

Figure 2 shows histograms of a number of different emission line properties for samples A and B. As discussed by previous authors (e.g. [Weymann et al. 1991](#)), we find that BAL and non-BAL quasars really do seem to possess very similar emission line properties. The EW is related to the ‘face-on’ equivalent width,  $EW_0$  by the equation

$$EW = EW_0 / \epsilon(\theta) \quad (4.2)$$

where  $\theta$  is the viewing angle with respect to the symmetry axis and  $\epsilon(\theta)$  is the ‘angular

emissivity function', which describes how the continuum luminosity from the disc varies as a function of viewing angle. For a foreshortened disc this is simply  $\epsilon(\theta) = \cos \theta$ .

Thus, if BAL quasars are viewed from a larger viewing angle on average then one would expect them to possess higher EWs, with a broader distribution. It is already apparent from figure 1 that the BAL distribution mean is not systematically higher than the non-BAL mean – in fact, it is lower. This is not expected from a model in which the continuum is foreshortened and BAL outflows are at all equatorial. This problem is examined further in section 4.3. First, we will examine the motivations for different forms of  $\epsilon(\theta)$  in AGN and quasars.

## 4.2 The Angular Distribution of Emission from an Accretion Disc and Broad-Line Region

The most widely-used theoretical model for an accretion disc was proposed by Shakura & Sunyaev (1973; hereafter SS73). There are a number of well-documented problems when fitting AGN SEDs with SS73 accretion disc models (REFs), and there are also tensions with the ‘accretion disc size’ relation from time lags (Edelson et al. 2015) and microlensing (Morgan et al. 2010). Despite these problems, Capellupo et al. (2015) recently had some success fitting VLT XSHOOTER spectra of AGN when the effects of GR, mass-loss and comptonisation were included. In this section, we start by discussing the angular distribution of emission from an SS73 disc, before discussing opacity and GR effects. In order to explore these effects, we use AGNSPEC (Hubeny et al. 2000; Davis & Hubeny 2006; Davis et al. 2007). We stress that the discussion here is not limited to SS73 discs; the only real condition for the expected angular distributions derived here is that the disc is geometrically thin and optically thick.

### 4.2.1 Standard Thin Disc Models

A geometrically thin, optically thick disc will appear foreshortened and limb darkened (if temperature decreases with height from the central disc plane). Foreshortening is a simple  $\cos \theta$  geometric effect, where  $\theta$  is the inclination with respect to the vertical z

axis, which is perpendicular to the disc plane. Limb darkening,  $\eta(\theta)$ , is given by

$$\eta(\theta) = a(1 + b \cos \theta), \quad (4.3)$$

where  $a$  is a normalisation constant and  $b$  governs the strength of the limb darkening.  $b = 3/2$ , known as the Eddington approximation tends to give good agreement with solar observations (e.g. [Mihalas 1982](#)). The two effects can be combined to give an angular emissivity function, of

$$\epsilon(\theta) = a \cos \theta \left(1 + \frac{3}{2} \cos \theta\right). \quad (4.4)$$

#### 4.2.2 Including GR, Comptonisation and Opacity Effects

In reality, limb darkening is not frequency independent and depends on the bound-free and bound-bound opacities in the disc. In addition, it has been shown that GR can ‘isotropize’ the radiation field in XRBs ([Zhang et al. 1997](#); [Muñoz-Darias et al. 2013](#)), in some cases overcoming foreshortening effects. To assess the impact of GR and disc opacities on  $\epsilon(\theta)$  we use AGNSPEC models, which uses stellar atmosphere calculations to calculate the SED in a series of annuli, before using the KERRTRANS code to calculate the emergent SED by ray-tracing along Kerr geodesics. In Fig. 4.4, we show  $\epsilon(\theta)$  as a function of  $\theta$  for AGNSPEC models for minimally and maximally spinning BHs, compared to foreshortened and limb-darkened predictions for SS73 models. Clearly, there is very little effect; the accretion disc is still strongly anisotropic in the relevant wavebands.

#### 4.2.3 Alternative Continuum Models: Irradiation and Truncated Discs

Alternative Models exist...

### 4.3 Predicted EW distributions compared to observations: A Monte Carlo approach

We assume  $\epsilon(\theta) = \cos \theta$ , as this is the conservative estimate.

Our Monte Carlo simulation undergoes the following steps:

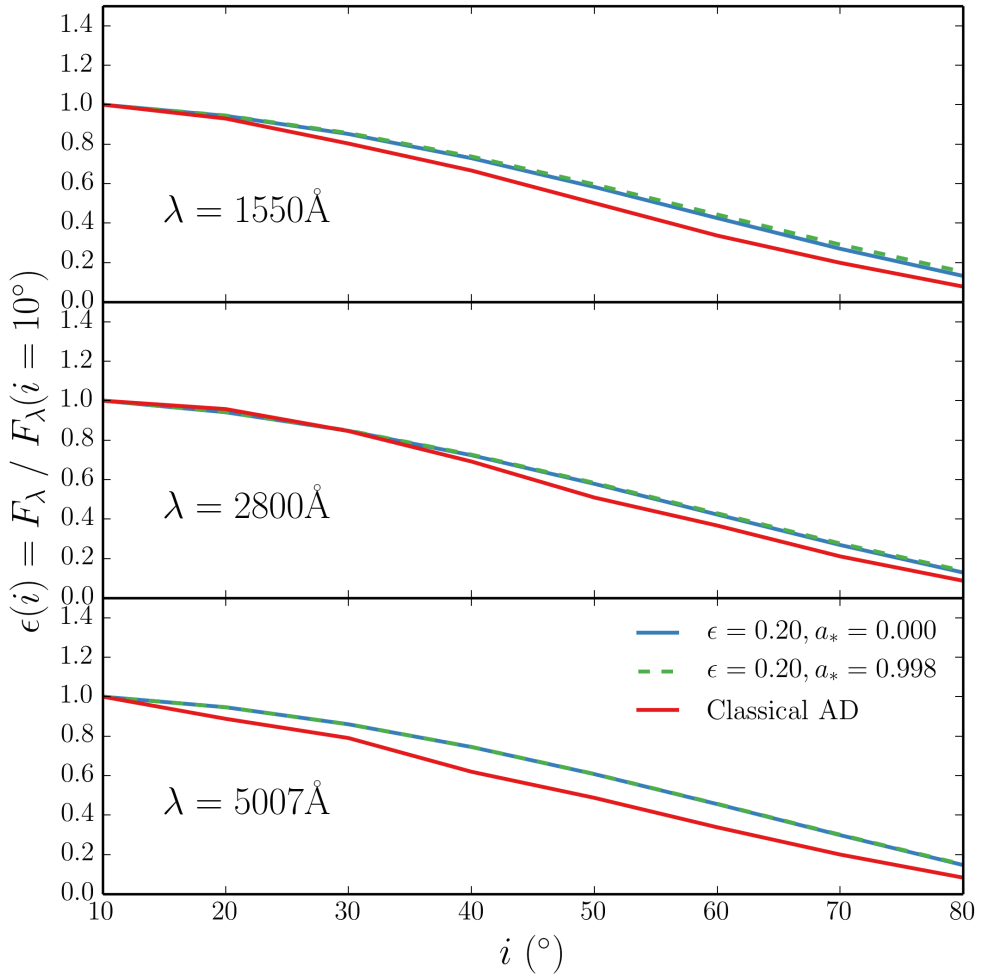


FIGURE 4.4: Monochromatic continuum luminosities from AGNSPEC and classical thin disc models.

1. A set of isotropic angles is chosen such that  $P(\theta) \propto d\Omega(\theta)$ . If  $\theta_{min} < \theta < \theta_{max}$  then the fake object is flagged as a mock BAL. If  $\theta < \theta_{min}$  then the fake object is designated a non-BAL, and otherwise the object is ignored. To be included in the sample, the object also has to survive a selection test based on a arbitrary flux selection limit, to simulate the distribution of angles in a flux-limited sample.
2. We then construct our best estimate of the intrinsic (i.e. ‘face-on’) EW distribution for non-BAL quasars. This is done via a  $\chi^2$  minimisation, by finding the gaussian with  $\mu$  and  $\sigma$  which best reproduces the observed distribution when convolved with the non-BAL angles generated in the previous step. a  $\chi^2$  minimisation.

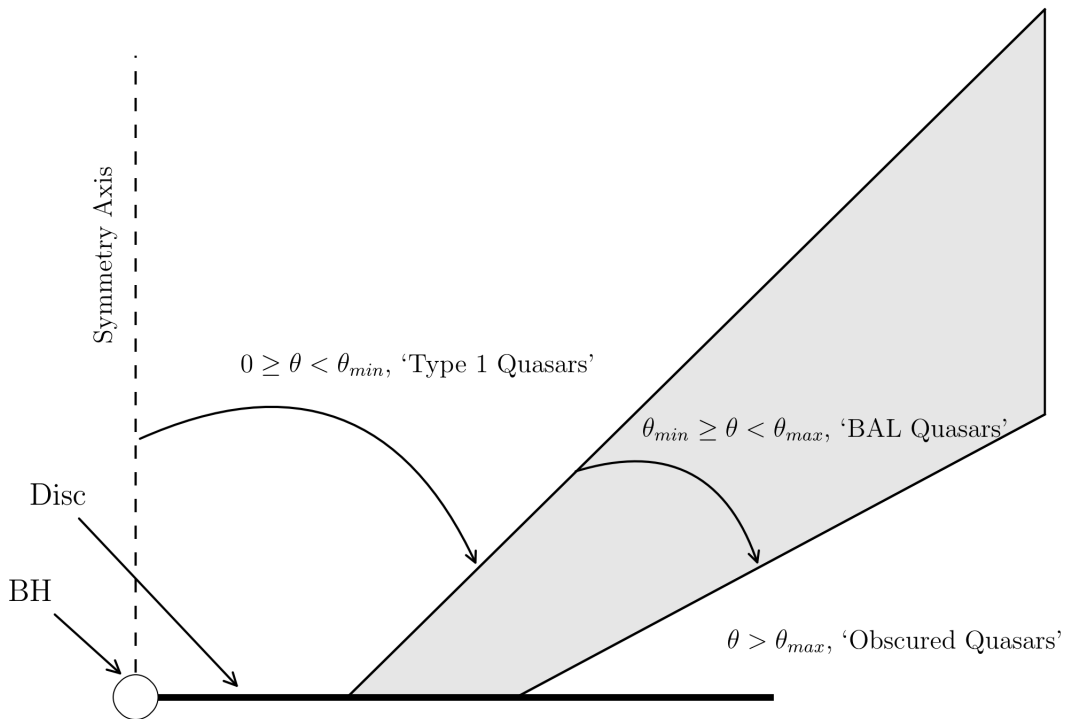
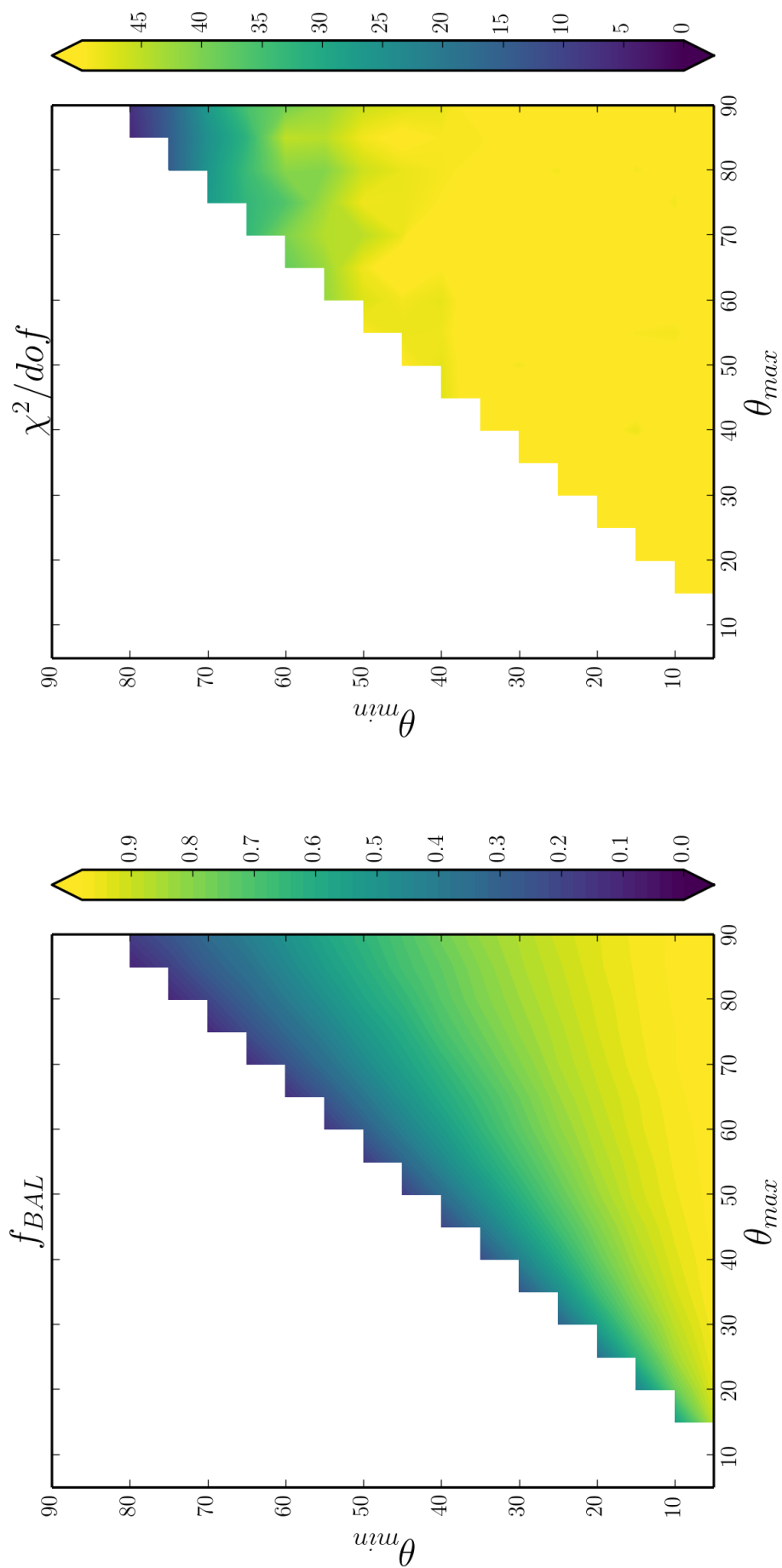


FIGURE 4.5: The geometry of the toy model used to carry out the Monte Carlo simulations

3. For each mock sample, a  $\text{EW}_0$  is drawn from the intrinsic gaussian.
4. a mock EW is estimated such that  $\text{EW} = \text{EW}_0/\epsilon(\theta)$ , and this process is repeated to build up a mock sample of objects.
5. The number of objects in the mock sample with  $\theta_{min} < \theta < \theta_{max}$  is recorded, providing an estimate of the expected BAL fraction for this wind geometry. This already includes a selection effect for the weaker continuum flux.
6. The value of the K-S test statistic is recorded, in which the mock BAL sample is compared to the real BAL sample. We also record the mean and variance of the mock sample. This allows us to ascertain which regions of parameter space best fit the observed BAL distribution

This process is repeated for a grid of  $\theta_{min}$  and  $\theta_{max}$ . The results are shown in figure 4.6, in which we plot the mean, standard deviation and  $f_{BAL}$  as a function of  $\theta_{min}$  and  $\theta_{max}$ . As expected, we find that equatorial viewing angles are strongly disfavoured.



## 4.4 Discussion

We have demonstrated that the EW distributions of the OIII emission line in quasars is not consistent with a model in which BALs are viewed from equatorial angles and the continuum emission originates from a foreshortened accretion disc. This conclusion would be strengthened were we to include limb darkening. This conclusion is extendible to the broad emission lines (IS IT?), with the caveat that those lines are dipole transitions and so opacity effects can change the angular distribution of emission. A number of other observations...

### 4.4.1 Radio Observations

Figure ? shows the equivalent width distributions in radio-loud quasars, split into core or lobe dominated. This designation is commonly used as an orientation indicator ([Orr & Browne 1982](#); [Wills & Brotherton 1995](#)). Although th

In this case, we can see that A full investigation of this is beyond the scope

### 4.4.2 Polarisation

Discuss polarisation

### 4.4.3 Compton-thick Fractions

Compton-thick Fractions

### 4.4.4 Theoretical Considerations

Discuss Proga models: They tend to rise fairly equatorially (see eg. PK04) Talk to Nick?

## 4.5 Conclusions

We find four possible scenarios:

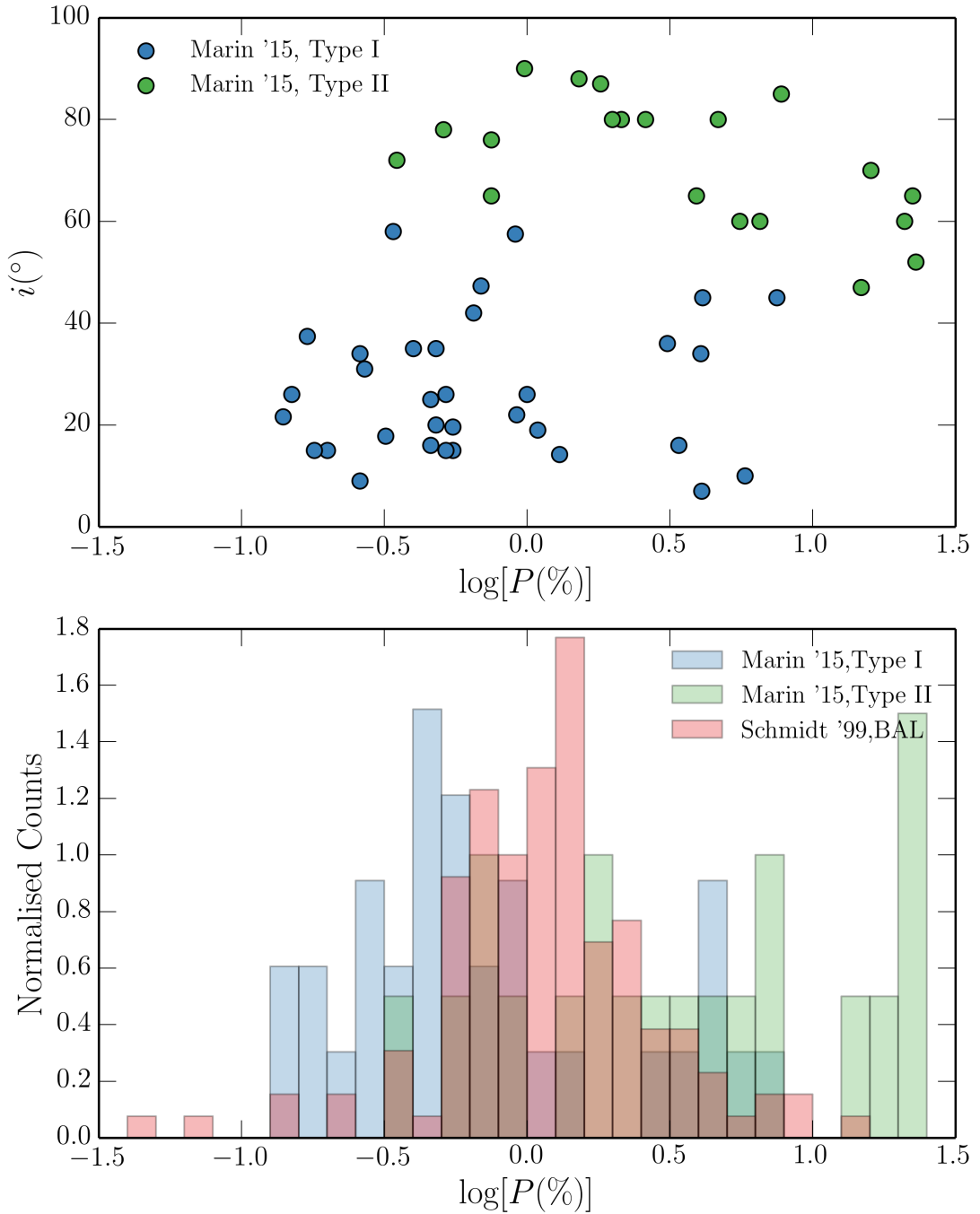


FIGURE 4.7: *Top:* Polarisation percentages as a function of measured inclination from Marin et al. (2015) for Type I and Type II AGN. *Bottom:* Histograms of polarisation percentages for BAL quasars from Schmidt et al. (1999) together with the Marin et al. (2015) AGN sample.

- *Scenario 1:* Quasar discs are much more isotropic than one might expect from an SS73 type disc. We have ascertained that general relativistic effects cannot account for discrepancy in the UV. Reprocessing by surrounding dense plasma with a large covering factor, or limb brightening caused by X-ray irradiation, may provide possible explanations which we do not yet confirm or refute.
- *Scenario 2:* Quasar discs are strongly anisotropic, as expected from a geometrically thin, optically thick accretion disc. In this case we expect  $f_{BAL} \sim 1$  due to the selection effects at work, and a velocity field yadiyada.
- *Scenario 3:* BAL outflows are more collimated than expected from early polarisation measurements. This easily explains the emission line properties of BAL and non-BAL quasars. However, equatorial geometries have been most successful when modelling BAL quasars, and there are clear differences in the polarisation properties of BAL and non-BAL quasars. We recommend that future RT modelling efforts explore different outflow geometries and that detailed polarisation modelling is undertaken to constrain the outflow opening angles.
- *Scenario 4:* The geometric unification model does not explain the incidence of BALs in quasar, or requires an additional component which is *time-dependent*, such as an evolutionary or accretion state origin for BAL outflows. In this scenario, BAL quasars would be seen from very similar angles to non-BAL quasars. However, the evidence for this is limited and there is no good model for why outflows would exist only for  $\sim 20\%$  of a quasar's lifetime. Even if this is the case, then the covering factor of the outflow still needs to be constrained in order to estimate the BAL duty cycle.

Of these, we favour scenario 3, as RT modelling of complex geometries is often degenerate (see Borguet et al. 2010 and Matthews et al. 2015 for details) and the differences in measured polarisation angle to not necessarily

# Bibliography

- Abbott D. C., 1982, ApJ 259, 282
- Abbott D. C., Lucy L. B., 1985, ApJ 288, 679
- Adams F. C., Graff D. S., Richstone D. O., 2001, ApJ Letters 551, L31
- Alexander D. M., Bauer F. E., Brandt W. N., Daddi E., Hickox R. C., Lehmer B. D., Luo B., Xue Y. Q., Young M., Comastri A., Del Moro A., Fabian A. C., Gilli R., Goulding A. D., Mainieri V., Mullaney J. R., Paolillo M., Rafferty D. A., Schneider D. P., Shemmer O., Vignali C., 2011, ApJ 738, 44
- Allen J. T., Hewett P. C., Maddox N., Richards G. T., Belokurov V., 2011, MNRAS 410, 860
- Antonucci R., 1988, in M. Kafatos (ed.), Supermassive Black Holes, p. 26
- Antonucci R., 2013, Nature 495, 165
- Antonucci R., Geller R., Goodrich R. W., Miller J. S., 1996, ApJ 472, 502
- Antonucci R. R. J., Miller J. S., 1985, ApJ 297, 621
- Arav N., 1996, ApJ 465, 617
- Arav N., Korista K. T., Barlow T. A., Begelman, 1995, Nature 376, 576
- Arévalo P., Uttley P., 2006, MNRAS 367, 801
- Balbus S. A., Hawley J. F., 1991, ApJ 376, 214
- Baldi R. D., Capetti A., Robinson A., Laor A., Behar E., 2016, MNRAS
- Baldry I. K., Glazebrook K., Brinkmann J., Ivezić Ž., Lupton R. H., Nichol R. C., Szalay A. S., 2004, ApJ 600, 681

- Baptista R., Silveira C., Steiner J. E., Horne K., 2000, MNRAS 314, 713
- Bartlett E., 2013, Ph.D. thesis, University of Southampton
- Becker R. H., White R. L., Gregg M. D., Brotherton M. S., Laurent-Muehleisen S. A., Arav N., 2000, ApJ 538, 72
- Begelman M. C., McKee C. F., Shields G. A., 1983, ApJ 271, 70
- Bell E. F., McIntosh D. H., Katz N., Weinberg M. D., 2003, ApJs 149, 289
- Belloni T. (ed.), 2010, The Jet Paradigm, Vol. 794 of *Lecture Notes in Physics, Berlin Springer Verlag*
- Benz A. O., Fuerst E., Kiplinger A. L., 1983, Nature 302, 45
- Bîrzan L., McNamara B. R., Nulsen P. E. J., Carilli C. L., Wise M. W., 2008, ApJ 686, 859
- Blandford R. D., Payne D. G., 1982, MNRAS 199, 883
- Blandford R. D., Znajek R. L., 1977, MNRAS 179, 433
- Bondi H., 1952, MNRAS 112, 195
- Bondi H., Hoyle F., 1944, MNRAS 104, 273
- Bongiorno A., Schulze A., Merloni A., Zamorani G., Ilbert O., La Franca F., Peng Y., Piconcelli E., Mainieri V., Silverman J. D., Brusa M., Fiore F., Salvato M., Scoville N., 2016, A&A 588, A78
- Bonning E. W., Cheng L., Shields G. A., Salviander S., Gebhardt K., 2007, ApJ 659, 211
- Borguet B., Hutsemékers D., 2010, A&A 515, A22
- Borguet B. C. J., Arav N., Edmonds D., Chamberlain C., Benn C., 2013, ApJ 762, 49
- Boroson T. A., Meyers K. A., 1992, ApJ 397, 442
- Bowler R. A. A., Hewett P. C., Allen J. T., Ferland G. J., 2014, MNRAS 445, 359
- Braito V., Reeves J. N., Dewangan G. C., George I., Griffiths R. E., Markowitz A., Nandra K., Porquet D., Ptak A., Turner T. J., Yaqoob T., Weaver K., 2007, ApJ 670, 978

- Brown J. C., Richardson L. L., Antokhin I., Robert C., Moffat A. F. J., St-Louis N., 1995, A&A 295, 725
- Burkert A., Silk J., 2001, ApJ Letters 554, L151
- Capellupo D. M., Hamann F., Barlow T. A., 2014, MNRAS 444, 1893
- Capellupo D. M., Hamann F., Shields J. C., Rodríguez Hidalgo P., Barlow T. A., 2011, MNRAS 413, 908
- Capellupo D. M., Hamann F., Shields J. C., Rodríguez Hidalgo P., Barlow T. A., 2012, MNRAS 422, 3249
- Capellupo D. M., Netzer H., Lira P., Trakhtenbrot B., Mejía-Restrepo J., 2015, MNRAS 446, 3427
- Cappi M., Mihara T., Matsuoka M., Hayashida K., Weaver K. A., Otani C., 1996, ApJ 458, 149
- Cassinelli J. P., 1979, ARAA 17, 275
- Castor J. I., Abbott D. C., Klein R. I., 1975, ApJ 195, 157
- Castor J. L., 1974, MNRAS 169, 279
- Cavagnolo K. W., McNamara B. R., Wise M. W., Nulsen P. E. J., Brüggen M., Gitti M., Rafferty D. A., 2011, ApJ 732, 71
- Chamberlain C., Arav N., Benn C., 2015, MNRAS 450, 1085
- Chartas G., Kochanek C. S., Dai X., Poindexter S., Garmire G., 2009, ApJ 693, 174
- Chen B., Dai X., Baron E., 2013a, ApJ 762, 122
- Chen B., Dai X., Baron E., Kantowski R., 2013b, ApJ 769, 131
- Clavel J., Schartel N., Tomas L., 2006, A&A 446, 439
- Cohen M. H., Ogle P. M., Tran H. D., Vermeulen R. C., Miller J. S., Goodrich R. W., Martel A. R., 1995, ApJ Letters 448, L77
- Cohen R. D., Puetter R. C., Rudy R. J., Ake T. B., Foltz C. B., 1986, ApJ 311, 135
- Connolly S. D., McHardy I. M., Dwelly T., 2014, MNRAS 440, 3503

- Coppejans D. L., Körding E. G., Miller-Jones J. C. A., Rupen M. P., Knigge C., Sivakoff G. R., Groot P. J., 2015, MNRAS 451, 3801
- Cordova F. A., Mason K. O., 1982, ApJ 260, 716
- Cottis C. E., Goad M. R., Knigge C., Scaringi S., 2010, MNRAS 406, 2094
- Crenshaw D. M., Rodriguez-Pascual P. M., Penton S. V., Edelson R. A., Alloin D., Ayres T. R., Clavel J., Horne K., Johnson W. N., Kaspi S., Korista K. T., Kriss G. A., Krolik J. H., Malkan M. A., Maoz D., Netzer H., O'Brien P. T., Peterson B. M., Reichert G. A., Shull J. M., Ulrich M.-H., Wamsteker W., Warwick R. S., Yaqoob T., Balonek T. J., Barr P., Bromage G. E., Carini M., Carone T. E., Cheng F.-Z., Chuvaev K. K., Dietrich M., Doroshenko V. T., Dultzin-Hacyan D., Filippenko A. V., Gaskell C. M., Glass I. S., Goad M. R., Hutchings J., Kazanas D., Kollatschny W., Koratkar A. P., Laor A., Leighly K., Lyutyi V. M., MacAlpine G. M., Malkov Y. F., Martin P. G., McCollum B., Merkulova N. I., Metik L., Metlov V. G., Miller H. R., Morris S. L., Oknyanskij V. L., Penfold J., Perez E., Perola G. C., Pike G., Pogge R. W., Pronik I., Pronik V. I., Ptak R. L., Recondo-Gonzalez M. C., Rodriguez-Espinoza J. M., Rokaki E. L., Roland J., Sadun A. C., Salamanca I., Santos-Lleo M., Sergeev S. G., Smith S. M., Snijders M. A. J., Sparke L. S., Stirpe G. M., Stoner R. E., Sun W.-H., van Groningen E., Wagner R. M., Wagner S., Wanders I., Welsh W. F., Weymann R. J., Wilkes B. J., Zheng W., 1996, ApJ 470, 322
- Croton D. J., Springel V., White S. D. M., De Lucia G., Frenk C. S., Gao L., Jenkins A., Kauffmann G., Navarro J. F., Yoshida N., 2006, MNRAS 365, 11
- Dabrowski Y., Fabian A. C., Iwasawa K., Lasenby A. N., Reynolds C. S., 1997, MNRAS 288, L11
- Dai X., Kochanek C. S., Chartas G., Kozłowski S., Morgan C. W., Garmire G., Agol E., 2010, ApJ 709, 278
- Dai X., Shankar F., Sivakoff G. R., 2008, ApJ 672, 108
- Dai X., Shankar F., Sivakoff G. R., 2012, ApJ 757, 180
- Davis S. W., Hubeny I., 2006, ApJs 164, 530
- Davis S. W., Woo J.-H., Blaes O. M., 2007, ApJ 668, 682

- de Kool M., Begelman M. C., 1995, ApJ 455, 448
- Denney K. D., De Rosa G., Croxall K., Gupta A., Bentz M. C., Fausnaugh M. M., Grier C. J., Martini P., Mathur S., Peterson B. M., Pogge R. W., Shappee B. J., 2014, ApJ 796, 134
- Dexter J., Agol E., 2011, ApJ Letters 727, L24
- Dhillon V. S., 1996, in A. Evans, J. H. Wood (eds.), IAU Colloq. 158: Cataclysmic Variables and Related Objects, Vol. 208 of *Astrophysics and Space Science Library*, 3
- Dhillon V. S., Rutten R. G. M., 1995, MNRAS 277, 777
- Díaz Trigo M., Boirin L., 2015, ArXiv e-prints
- Done C., Davis S. W., Jin C., Blaes O., Ward M., 2012, MNRAS 420, 1848
- Done C., Jin C., 2015, ArXiv e-prints
- Drew J., Verbunt F., 1985, MNRAS 213, 191
- Echevarria J., 1988, MNRAS 233, 513
- Edelson R., Gelbord J. M., Horne K., McHardy I. M., Peterson B. M., Arévalo P., Breeveld A. A., De Rosa G., Evans P. A., Goad M. R., Kriss G. A., Brandt W. N., Gehrels N., Grupe D., Kennea J. A., Kochanek C. S., Nousek J. A., Papadakis I., Siegel M., Starkey D., Uttley P., Vaughan S., Young S., Barth A. J., Bentz M. C., Brewer B. J., Crenshaw D. M., Dalla Bontà E., De Lorenzo-Cáceres A., Denney K. D., Dietrich M., Ely J., Fausnaugh M. M., Grier C. J., Hall P. B., Kaastra J., Kelly B. C., Korista K. T., Lira P., Mathur S., Netzer H., Pancoast A., Pei L., Pogge R. W., Schimoia J. S., Treu T., Vestergaard M., Villforth C., Yan H., Zu Y., 2015, ApJ 806, 129
- Edge D. O., Shakeshaft J. R., McAdam W. B., Baldwin J. E., Archer S., 1959, MmRA 68, 37
- Eggleton P. P., 1983, ApJ 268, 368
- Ehman J. R., Dixon R. S., Kraus J. D., 1970, AJ 75, 351
- Ekers J. A., 1969, Australian Journal of Physics Astrophysical Supplement 7

- Elitzur M., 2012, ApJ Letters 747, L33
- Elitzur M., Ho L. C., Trump J. R., 2014, MNRAS 438, 3340
- Elvis M., 2000, ApJ 545, 63
- Elvis M., Wilkes B. J., McDowell J. C., Green R. F., Bechtold J., Willner S. P., Oey M. S., Polomski E., Cutri R., 1994, ApJs 95, 1
- Fabian A. C., 2012, ARAA 50, 455
- Fabian A. C., Kunieda H., Inoue S., Matsuoka M., Mihara T., Miyamoto S., Otani C., Ricker G., Tanaka Y., Yamauchi M., Yaqoob T., 1994, PASJ 46, L59
- Fabian A. C., Nandra K., Reynolds C. S., Brandt W. N., Otani C., Tanaka Y., Inoue H., Iwasawa K., 1995, MNRAS 277, L11
- Fath E. A., 1909, Lick Observatory Bulletin 5, 71
- Fender R. P., 2001, MNRAS 322, 31
- Fender R. P., Belloni T. M., Gallo E., 2004, MNRAS 355, 1105
- Fender R. P., Gallo E., Russell D., 2010, MNRAS 406, 1425
- Ferrarese L., Merritt D., 2000, ApJ Letters 539, L9
- Filiz Ak N., Brandt W. N., Hall P. B., Schneider D. P., Anderson S. F., Gibson R. R., Lundgren B. F., Myers A. D., Petitjean P., Ross N. P., Shen Y., York D. G., Bizyaev D., Brinkmann J., Malanushenko E., Oravetz D. J., Pan K., Simmons A. E., Weaver B. A., 2012, ApJ 757, 114
- Foltz C. B., Weymann R. J., Morris S. L., Turnshek D. A., 1987, ApJ 317, 450
- Frank J., King A., Raine D., 1992, Accretion power in astrophysics.
- Fukumura K., Tombesi F., Kazanas D., Shrader C., Behar E., Contopoulos I., 2015, ApJ 805, 17
- Gallagher S. C., Brandt W. N., Chartas G., Garmire G. P., 2002, ApJ 567, 37
- Gallagher S. C., Brandt W. N., Sambruna R. M., Mathur S., Yamasaki N., 1999, ApJ 519, 549

- Gallo E., Fender R. P., Pooley G. G., 2003, MNRAS 344, 60
- Gandhi P., Hönig S. F., Kishimoto M., 2015, ApJ 812, 113
- Gandhi P., Terashima Y., Yamada S., Mushotzky R. F., Ueda Y., Baumgartner W. H., Alexander D. M., Malzac J., Vaghmare K., Takahashi T., Done C., 2013, ApJ 773, 51
- Ganguly R., Bond N. A., Charlton J. C., Eracleous M., Brandt W. N., Churchill C. W., 2001, ApJ 549, 133
- Ganguly R., Sembach K. R., Tripp T. M., Savage B. D., Wakker B. P., 2006, ApJ 645, 868
- Gardner E., Done C., 2016, ArXiv e-prints
- Gebhardt K., Bender R., Bower G., Dressler A., Faber S. M., Filippenko A. V., Green R., Grillmair C., Ho L. C., Kormendy J., Lauer T. R., Magorrian J., Pinkney J., Richstone D., Tremaine S., 2000, ApJ Letters 539, L13
- Ghosh K. K., Punsly B., 2007, ApJ Letters 661, L139
- Gibson R. R., Jiang L., Brandt W. N., Hall P. B., Shen Y., Wu J., Anderson S. F., Schneider D. P., Vanden Berk D., Gallagher S. C., Fan X., York D. G., 2009, ApJ 692, 758
- Gierliński M., Done C., 2004, MNRAS 349, L7
- Gierliński M., Done C., 2006, MNRAS 371, L16
- Giustini M., Cappi M., Chartas G., Dadina M., Eracleous M., Ponti G., Proga D., Tombesi F., Vignali C., Palumbo G. G. C., 2011, A&A 536, A49
- Gofford J., Reeves J. N., Braito V., Nardini E., Costa M. T., Matzeu G. A., O'Brien P., Ward M., Turner T. J., Miller L., 2014, ApJ 784, 77
- Gofford J., Reeves J. N., McLaughlin D. E., Braito V., Turner T. J., Tombesi F., Cappi M., 2015, MNRAS 451, 4169
- Gofford J., Reeves J. N., Tombesi F., Braito V., Turner T. J., Miller L., Cappi M., 2013, MNRAS 430, 60

- Goodrich R. W., 1997, ApJ 474, 606
- Goodrich R. W., Miller J. S., 1995, ApJ Letters 448, L73
- Gough B., 2009, GNU Scientific Library Reference Manual - Third Edition, Network Theory Ltd., 3rd edition
- Green A. R., McHardy I. M., Lehto H. J., 1993, MNRAS 265, 664
- Green P. J., Aldcroft T. L., Mathur S., Wilkes B. J., Elvis M., 2001, ApJ 558, 109
- Greenstein J. L., Oke J. B., 1982, ApJ 258, 209
- Groot P. J., Rutten R. G. M., van Paradijs J., 2004, A&A 417, 283
- Grupe D., Mathur S., Elvis M., 2003, AJ 126, 1159
- Grupe D., Nousek J. A., 2015, AJ 149, 85
- Gültekin K., Richstone D. O., Gebhardt K., Lauer T. R., Tremaine S., Aller M. C., Bender R., Dressler A., Faber S. M., Filippenko A. V., Green R., Ho L. C., Kormendy J., Magorrian J., Pinkney J., Siopis C., 2009, ApJ 698, 198
- Haardt F., Maraschi L., 1991, ApJ Letters 380, L51
- Hall P. B., Anderson S. F., Strauss M. A., York D. G., Richards G. T., Fan X., Knapp G. R., Schneider D. P., Vanden Berk D. E., Geballe T. R., Bauer A. E., Becker R. H., Davis M., Rix H.-W., Nichol R. C., Bahcall N. A., Brinkmann J., Brunner R., Connolly A. J., Csabai I., Doi M., Fukugita M., Gunn J. E., Haiman Z., Harvanek M., Heckman T. M., Hennessy G. S., Inada N., Ivezić Ž., Johnston D., Kleinman S., Krolik J. H., Krzesinski J., Kunszt P. Z., Lamb D. Q., Long D. C., Lupton R. H., Miknaitis G., Munn J. A., Narayanan V. K., Neilsen E., Newman P. R., Nitta A., Okamura S., Pentericci L., Pier J. R., Schlegel D. J., Snedden S., Szalay A. S., Thakar A. R., Tsvetanov Z., White R. L., Zheng W., 2002, ApJs 141, 267
- Hall P. B., Anosov K., White R. L., Brandt W. N., Gregg M. D., Gibson R. R., Becker R. H., Schneider D. P., 2011, MNRAS 411, 2653
- Halpern J. P., 1984, ApJ 281, 90
- Hamann F., Chartas G., McGraw S., Rodriguez Hidalgo P., Shields J., Capellupo D., Charlton J., Eracleous M., 2013, MNRAS 435, 133

- Hamann W.-R., Koesterke L., 1998, A&A 335, 1003
- Hamann W.-R., Leuenhagen U., Koesterke L., Wessolowski U., 1992, A&A 255, 200
- Hamann W.-R., Oskinova L. M., Feldmeier A., 2008, in W.-R. Hamann, A. Feldmeier, L. M. Oskinova (eds.), Clumping in Hot-Star Winds, 75
- Hamann W.-R., Wessolowski U., Koesterke L., 1994, A&A 281, 184
- Häring N., Rix H.-W., 2004, ApJ Letters 604, L89
- Hassall B. J. M., 1985, MNRAS 216, 335
- Haug K., 1987, AP&SS 130, 91
- Hazard C., Mackey M. B., Shimmins A. J., 1963, Nature 197, 1037
- Hazard C., Morton D. C., Terlevich R., McMahon R., 1984, ApJ 282, 33
- Heap S. R., Boggess A., Holm A., Klinglesmith D. A., Sparks W., West D., Wu C. C., Boksenberg A., Willis A., Wilson R., Macchetto F., Selvelli P. O., Stickland D., Greenstein J. L., Hutchings J. B., Underhill A. B., Viotti R., Whelan J. A. J., 1978, Nature 275, 385
- Heil L. M., Vaughan S., Uttley P., 2012, MNRAS 422, 2620
- Hessman F. V., Robinson E. L., Nather R. E., Zhang E.-H., 1984, ApJ 286, 747
- Higginbottom N., Knigge C., Long K. S., Sim S. A., Matthews J. H., 2013, MNRAS 436, 1390
- Higginbottom N., Proga D., Knigge C., Long K. S., Matthews J. H., Sim S. A., 2014, ApJ 789, 19
- Hillier D. J., 1984, ApJ 280, 744
- Hillier D. J., 1991, A&A 247, 455
- Hillier D. J., Miller D. L., 1999, ApJ 519, 354
- Hoare M. G., Drew J. E., 1991, MNRAS 249, 452
- Hoare M. G., Drew J. E., 1993, MNRAS 260, 647
- Hogg J. D., Reynolds C., 2015, ArXiv e-prints

- Honeycutt R. K., Schlegel E. M., Kaitchuck R. H., 1986, ApJ 302, 388
- Hönig S. F., Kishimoto M., Tristram K. R. W., Prieto M. A., Gandhi P., Asmus D., Antonucci R., Burtscher L., Duschl W. J., Weigelt G., 2013, ApJ 771, 87
- Horne K., 1993, Eclipse Mapping of Accretion Disks: The First Decade, 117
- Horne K., Marsh T. R., 1986, MNRAS 218, 761
- Hoyle F., Lyttleton R. A., 1939, Proceedings of the Cambridge Philosophical Society 35, 405
- Hubeny I., Agol E., Blaes O., Krolik J. H., 2000, ApJ 533, 710
- Humphrey A., Binette L., 2014, MNRAS 442, 753
- Idan I., Lasota J.-P., Hameury J.-M., Shaviv G., 2010, A&A 519, A117
- Ioannou Z., van Zyl L., Naylor T., Charles P. A., Margon B., Koch-Miramond L., Illovaisky S., 2003, A&A 399, 211
- Iwasawa K., Fabian A. C., Mushotzky R. F., Brandt W. N., Awaki H., Kunieda H., 1996a, MNRAS 279, 837
- Iwasawa K., Fabian A. C., Reynolds C. S., Nandra K., Otani C., Inoue H., Hayashida K., Brandt W. N., Dotani T., Kunieda H., Matsuoka M., Tanaka Y., 1996b, MNRAS 282, 1038
- Janiuk A., Czerny B., Madejski G. M., 2001, ApJ 557, 408
- Ju W., Stone J. M., Zhu Z., 2016, ArXiv e-prints
- Kaastra J. S., Kriss G. A., Cappi M., Mehdipour M., Petrucci P.-O., Steenbrugge K. C., Arav N., Behar E., Bianchi S., Boissay R., Branduardi-Raymont G., Chamberlain C., Costantini E., Ely J. C., Ebrero J., Di Gesu L., Harrison F. A., Kaspi S., Malzac J., De Marco B., Matt G., Nandra K., Paltani S., Person R., Peterson B. M., Pinto C., Ponti G., Nuñez F. P., De Rosa A., Seta H., Ursini F., de Vries C. P., Walton D. J., Whewell M., 2014, Science 345, 64
- Kaastra J. S., Mewe R., Liedahl D. A., Komossa S., Brinkman A. C., 2000, A&A 354, L83

- Kafka S., Honeycutt R. K., 2004, AJ 128, 2420
- Kerzendorf W. E., Sim S. A., 2014, MNRAS 440, 387
- King A., 2003, ApJ Letters 596, L27
- Knigge C., Baraffe I., Patterson J., 2011, ApJs 194, 28
- Knigge C., Drew J. E., 1997, ApJ 486, 445
- Knigge C., Long K. S., Blair W. P., Wade R. A., 1997, ApJ 476, 291
- Knigge C., Long K. S., Wade R. A., Baptista R., Horne K., Hubeny I., Rutten R. G. M., 1998a, ApJ 499, 414
- Knigge C., Long K. S., Wade R. A., Baptista R., Horne K., Hubeny I., Rutten R. G. M., 1998b, ApJ 499, 414
- Knigge C., Scaringi S., Goad M. R., Cottis C. E., 2008, MNRAS 386, 1426
- Knigge C., Woods J. A., Drew J. E., 1995, MNRAS 273, 225
- Koratkar A., Blaes O., 1999, PASP 111, 1
- Körding E., Rupen M., Knigge C., Fender R., Dhawan V., Templeton M., Muxlow T., 2008, Science 320, 1318
- Kormendy J., Ho L. C., 2013, ARAA 51, 511
- Kotov O., Churazov E., Gilfanov M., 2001, MNRAS 327, 799
- Kraft R. P., Mathews J., Greenstein J. L., 1962, ApJ 136, 312
- Kriss G. A., Krolik J. H., Otani C., Espey B. R., Turner T. J., Kii T., Tsvetanov Z., Takahashi T., Davidsen A. F., Tashiro M., Zheng W., Murakami S., Petre R., Mihara T., 1996, ApJ 467, 629
- Krolik J. H., Begelman M. C., 1986, in Bulletin of the American Astronomical Society, Vol. 18 of *BAAS*, 903
- Krolik J. H., Kriss G. A., 2001, ApJ 561, 684
- Krolik J. H., Voit G. M., 1998, ApJ Letters 497, L5
- Kromer M., Sim S. A., 2009, MNRAS 398, 1809

- Kusterer D.-J., Nagel T., Hartmann S., Werner K., Feldmeier A., 2014, A&A 561, A14
- Kuulkers E., Motta S., Kajava J., Homan J., Fender R., Jonker P., 2015, The Astronomer's Telegram 7647
- La Dous C., 1989, MNRAS 238, 935
- Laor A., 1991, ApJ 376, 90
- Laor A., Davis S. W., 2014, MNRAS 438, 3024
- Lasota J.-P., 2001, NAR 45, 449
- Lazarova M. S., Canalizo G., Lacy M., Sajina A., 2012, ApJ 755, 29
- Liebert J., Stockman H. S., 1985, in D. Q. Lamb, J. Patterson (eds.), *Cataclysmic Variables and Low-Mass X-ray Binaries*, Vol. 113 of *Astrophysics and Space Science Library*, p. 151
- Long K. S., Blair W. P., Davidsen A. F., Bowers C. W., Dixon W. V. D., Durrance S. T., Feldman P. D., Henry R. C., Kriss G. A., Kruk J. W., Moos H. W., Vancura O., Ferguson H. C., Kimble R. A., 1991, ApJ Letters 381, L25
- Long K. S., Knigge C., 2002, ApJ 579, 725
- Long K. S., Wade R. A., Blair W. P., Davidsen A. F., Hubeny I., 1994, ApJ 426, 704
- Lucy L. B., 2002, A&A 384, 725
- Lucy L. B., 2003, A&A 403, 261
- Lusso E., Worseck G., Hennawi J. F., Prochaska J. X., Vignali C., Stern J., O'Meara J. M., 2015, MNRAS 449, 4204
- Lynden-Bell D., 1969, Nature 223, 690
- Lyubarskii Y. E., 1997, MNRAS 292, 679
- Madau P., Ghisellini G., Fabian A. C., 1994, MNRAS 270, L17
- Magdziarz P., Blaes O. M., Zdziarski A. A., Johnson W. N., Smith D. A., 1998, MNRAS 301, 179

- Magorrian J., Tremaine S., Richstone D., Bender R., Bower G., Dressler A., Faber S. M., Gebhardt K., Green R., Grillmair C., Kormendy J., Lauer T., 1998, AJ 115, 2285
- Mangham S. W., Knigge C., Matthews J. H., Long K. S., Sim S. A., Higginbottom N., 2016, in prep.
- Marinucci A., Bianchi S., Matt G., Alexander D. M., Baloković M., Bauer F. E., Brandt W. N., Gandhi P., Guainazzi M., Harrison F. A., Iwasawa K., Koss M., Madsen K. K., Nicastro F., Puccetti S., Ricci C., Stern D., Walton D. J., 2016, MNRAS 456, L94
- Marscher A. P., 2006, in P. A. Hughes, J. N. Bregman (eds.), Relativistic Jets: The Common Physics of AGN, Microquasars, and Gamma-Ray Bursts, Vol. 856 of *American Institute of Physics Conference Series*, p. 1
- Marsh T. R., Horne K., 1990, ApJ 349, 593
- Matt G., Guainazzi M., Maiolino R., 2003, MNRAS 342, 422
- Matthews J. H., Knigge C., Long K. S., Sim S. A., Higginbottom N., 2015, MNRAS 450, 3331
- Matthews J. H., Knigge C., Long K. S., Sim S. A., Higginbottom N., Mangham S. W., 2016, MNRAS
- Matzeu G. A., Reeves J. N., Nardini E., Braito V., Costa M. T., Tombesi F., Gofford J., 2016, MNRAS 458, 1311
- Mauche C. W., 1996, ArXiv Astrophysics e-prints
- Mauche C. W., Raymond J. C., 1987, ApJ 323, 690
- Mazzali P. A., Lucy L. B., 1993, A&A 279, 447
- McConnell N. J., Ma C.-P., 2013, ApJ 764, 184
- McHardy I. M., Koerding E., Knigge C., Uttley P., Fender R. P., 2006, Nature 444, 730
- Mihalas D. M., 1982, Stellar atmospheres.
- Miller L., Turner T. J., 2013, ApJ Letters 773, L5
- Miller L., Turner T. J., Reeves J. N., 2008, A&A 483, 437

- Misawa T., Charlton J. C., Eracleous M., Ganguly R., Tytler D., Kirkman D., Suzuki N., Lubin D., 2007, ApJs 171, 1
- Misawa T., Eracleous M., Chartas G., Charlton J. C., 2008, ApJ 677, 863
- Misra R., Kembhavi A. K., 1998, ApJ 499, 205
- Mitsuda K., Inoue H., Nakamura N., Tanaka Y., 1989, PASJ 41, 97
- Morabito L. K., Dai X., Leighly K. M., Sivakoff G. R., Shankar F., 2013, ArXiv e-prints
- Morgan C. W., Kochanek C. S., Morgan N. D., Falco E. E., 2010, ApJ 712, 1129
- Motta S., Beardmore A., Oates S., Sanna N. P. M. K. A., Kuulkers E., Kajava J., Sanchez-Fernandez C., 2015, The Astronomer's Telegram 7665
- Muñoz-Darias T., Coriat M., Plant D. S., Ponti G., Fender R. P., Dunn R. J. H., 2013, MNRAS 432, 1330
- Murray N., Chiang J., 1996, Nature 382, 789
- Murray N., Chiang J., 1997, ApJ 474, 91
- Murray N., Chiang J., Grossman S. A., Voit G. M., 1995, ApJ 451, 498
- Nandra K., Pounds K. A., 1994, MNRAS 268, 405
- Narayan R., McClintock J. E., 2012, MNRAS 419, L69
- Narayan R., McClintock J. E., Tchekhovskoy A., 2014, Energy Extraction from Spinning Black Holes Via Relativistic Jets, 523
- Narayan R., Yi I., 1994, ApJ Letters 428, L13
- Narayan R., Yi I., 1995, ApJ 452, 710
- Nardini E., Reeves J. N., Gofford J., Harrison F. A., Risaliti G., Braito V., Costa M. T., Matzeu G. A., Walton D. J., Behar E., Boggs S. E., Christensen F. E., Craig W. W., Hailey C. J., Matt G., Miller J. M., O'Brien P. T., Stern D., Turner T. J., Ward M. J., 2015, Science 347, 860
- Nestor D., Hamann F., Rodriguez Hidalgo P., 2008, MNRAS 386, 2055
- Neugebauer G., Oke J. B., Becklin E. E., Matthews K., 1979, ApJ 230, 79

- Noebauer U. M., Long K. S., Sim S. A., Knigge C., 2010, ApJ 719, 1932
- North M., Knigge C., Goad M., 2006, MNRAS 365, 1057
- O'Dowd M. J., Bate N. F., Webster R. L., Labrie K., Rogers J., 2015, ArXiv e-prints
- Orr A., Molendi S., Fiore F., Grandi P., Parmar A. N., Owens A., 1997, A&A 324, L77
- Orr M. J. L., Browne I. W. A., 1982, MNRAS 200, 1067
- Osaki Y., 1974, PASJ 26, 429
- Otani C., Kii T., Reynolds C. S., Fabian A. C., Iwasawa K., Hayashida K., Inoue H., Kunieda H., Makino F., Matsuoka M., Tanaka Y., 1996, PASJ 48, 211
- Owocki S., 2014, ArXiv e-prints
- Owocki S. P., Castor J. I., Rybicki G. B., 1988, ApJ 335, 914
- Patterson J., 1984, ApJs 54, 443
- Patterson J., 1994, PASP 106, 209
- Patterson J., Patino R., Thorstensen J. R., Harvey D., Skillman D. R., Ringwald F. A., 1996, AJ 111, 2422
- Pauldrach A. W. A., Kudritzki R. P., Puls J., Butler K., Hunsinger J., 1994, A&A 283, 525
- Penrose R., Floyd R. M., 1971, Nature Physical Science 229, 177
- Pereyra N. A., Kallman T. R., Blondin J. M., 1997, ApJ 477, 368
- Perley R. A., Dreher J. W., Cowan J. J., 1984, ApJ Letters 285, L35
- Ponti G., Fender R. P., Begelman M. C., Dunn R. J. H., Neilsen J., Coriat M., 2012, MNRAS 422, L11
- Potash R. I., Wardle J. F. C., 1980, ApJ 239, 42
- Pounds K., Lobban A., Reeves J., Vaughan S., 2016, MNRAS 457, 2951
- Pounds K. A., Nandra K., Stewart G. C., Leighly K., 1989, MNRAS 240, 769
- Pounds K. A., Reeves J. N., 2009, MNRAS 397, 249

- Prinja R. K., Smith L. J., 1992, A&A 266, 377
- Proga D., 2005, in J.-M. Hameury, J.-P. Lasota (eds.), *The Astrophysics of Cataclysmic Variables and Related Objects*, Vol. 330 of *Astronomical Society of the Pacific Conference Series*, 103
- Proga D., Kallman T. R., 2004, ApJ 616, 688
- Proga D., Kallman T. R., Drew J. E., Hartley L. E., 2002, ApJ 572, 382
- Proga D., Stone J. M., Drew J. E., 1998, MNRAS 295, 595
- Proga D., Stone J. M., Kallman T. R., 2000, ApJ 543, 686
- Puccetti S., Fiore F., Risaliti G., Capalbi M., Elvis M., Nicastro F., 2007, MNRAS 377, 607
- Puebla R. E., Diaz M. P., Hillier D. J., Hubeny I., 2011, ApJ 736, 17
- Randall S. W., Forman W. R., Giacintucci S., Nulsen P. E. J., Sun M., Jones C., Churazov E., David L. P., Kraft R., Donahue M., Blanton E. L., Simionescu A., Werner N., 2011, ApJ 726, 86
- Read J. I., Trentham N., 2005, Philosophical Transactions of the Royal Society of London Series A 363
- Reeves J. N., O'Brien P. T., Ward M. J., 2003, ApJ Letters 593, L65
- Reeves J. N., Wynn G., O'Brien P. T., Pounds K. A., 2002, MNRAS 336, L56
- Reynolds C. S., 1999, in J. Poutanen, R. Svensson (eds.), *High Energy Processes in Accreting Black Holes*, Vol. 161 of *Astronomical Society of the Pacific Conference Series*, 178
- Reynolds C. S., Fabian A. C., 1995, MNRAS 273, 1167
- Ringwald F. A., Naylor T., 1998, AJ 115, 286
- Risaliti G., Elvis M., Fabbiano G., Baldi A., Zezas A., Salvati M., 2007, ApJ Letters 659, L111
- Risaliti G., Elvis M., Nicastro F., 2002, ApJ 571, 234
- Ross R. R., Fabian A. C., 2005, MNRAS 358, 211

- Rottenberg J. A., 1952, MNRAS 112, 125
- Rupke D. S. N., Veilleux S., 2011, ApJ Letters 729, L27
- Rutten R. G. M., van Paradijs J., Tinbergen J., 1992, A&A 260, 213
- Sabra B. M., Hamann F., 2001, ApJ 563, 555
- Scaringi S., Körding E., Uttley P., Knigge C., Groot P. J., Still M., 2012, MNRAS 421, 2854
- Scaringi S., Maccarone T. J., Koerding E., Knigge C., Vaughan S., Marsh T. R., Aranzana E., Dhillon V., Barros S. C. C., 2015, ArXiv e-prints
- Schechter P., 1976, ApJ 203, 297
- Schmidt M., 1963, Nature 197, 1040
- Schmidt M., 1965a, ApJ 141, 1295
- Schmidt M., 1965b, ApJ 141, 1
- Schmutz W., 1997, A&A 321, 268
- Setti G., Woltjer L., 1989, A&A 224, L21
- Seyfert C. K., 1943, ApJ 97, 28
- Shakura N. I., Sunyaev R. A., 1973, A&A 24, 337
- Shankar F., Calderone G., Knigge C., Matthews J., Buckland R., Hryniwicz K., Sivakoff G., Dai X., Richardson K., Riley J., Gray J., La Franca F., Altamirano D., Croston J., Gandhi P., Höning S., McHardy I., Middleton M., 2016, ApJ Letters 818, L1
- Shaviv G., Wehrse R., 1991, A&A 251, 117
- Shi Y., Rieke G. H., Smith P., Rigby J., Hines D., Donley J., Schmidt G., Diamond-Stanic A. M., 2010, ApJ 714, 115
- Shlosman I., Vitello P., 1993, ApJ 409, 372
- Silk J., Rees M. J., 1998, A&A 331, L1
- Silva C., Uttley P., Costantini E., 2015, in The Extremes of Black Hole Accretion, 63

- Sim S. A., 2004, MNRAS 349, 899
- Sim S. A., Drew J. E., Long K. S., 2005, MNRAS 363, 615
- Sim S. A., Long K. S., Miller L., Turner T. J., 2008, MNRAS 388, 611
- Sim S. A., Miller L., Long K. S., Turner T. J., Reeves J. N., 2010a, MNRAS 404, 1369
- Sim S. A., Proga D., Miller L., Long K. S., Turner T. J., 2010b, MNRAS 408, 1396
- Simon L. E., Hamann F., 2010, MNRAS 409, 269
- Sluse D., Hutsemékers D., Anguita T., Braibant L., Riaud P., 2015, ArXiv e-prints
- Smak J., 1981, ACTAA 31, 395
- Soltan A., 1982, MNRAS 200, 115
- Somerville R. S., Primack J. R., Faber S. M., 2001, MNRAS 320, 504
- Springel V., Di Matteo T., Hernquist L., 2005, ApJ Letters 620, L79
- Stalin C. S., Srianand R., Petitjean P., 2011, MNRAS 413, 1013
- Stockman H. S., Angel J. R. P., Miley G. K., 1979, ApJ Letters 227, L55
- Strateva I., Ivezić Ž., Knapp G. R., Narayanan V. K., Strauss M. A., Gunn J. E., Lupton R. H., Schlegel D., Bahcall N. A., Brinkmann J., Brunner R. J., Budavári T., Csabai I., Castander F. J., Doi M., Fukugita M., Győry Z., Hamabe M., Hennessy G., Ichikawa T., Kunszt P. Z., Lamb D. Q., McKay T. A., Okamura S., Racusin J., Sekiguchi M., Schneider D. P., Shimasaku K., York D., 2001, AJ 122, 1861
- Struve O., 1935, ApJ 81, 66
- Suleimanov V., Hertfelder M., Werner K., Kley W., 2014, ArXiv e-prints
- Surdej J., Hutsemekers D., 1987, A&A 177, 42
- Tatum M. M., Turner T. J., Sim S. A., Miller L., Reeves J. N., Patrick A. R., Long K. S., 2012, ApJ 752, 94
- Thorne K. S., 1974, ApJ 191, 507
- Tohline J. E., Osterbrock D. E., 1976, ApJ Letters 210, L117

- Tombesi F., Cappi M., Reeves J. N., Palumbo G. G. C., Yaqoob T., Braito V., Dadina M., 2010, A&A 521, A57
- Tombesi F., Meléndez M., Veilleux S., Reeves J. N., González-Alfonso E., Reynolds C. S., 2015, Nature 519, 436
- Tran H. D., 2001, ApJ Letters 554, L19
- Trump J. R., Hall P. B., Reichard T. A., Richards G. T., Schneider D. P., Vanden Berk D. E., Knapp G. R., Anderson S. F., Fan X., Brinkman J., Kleinman S. J., Nitta A., 2006, ApJs 165, 1
- Turing A. M., 1948, QJMAM 1(1), 287
- Urrutia T., Becker R. H., White R. L., Glikman E., Lacy M., Hodge J., Gregg M. D., 2009, ApJ 698, 1095
- Urry C. M., Padovani P., 1995, PASP 107, 803
- Uttley P., Cackett E. M., Fabian A. C., Kara E., Wilkins D. R., 2014, AAPR 22, 72
- Uttley P., McHardy I. M., 2001, MNRAS 323, L26
- Uttley P., McHardy I. M., Vaughan S., 2005, MNRAS 359, 345
- Van de Sande M., Scaringi S., Knigge C., 2015, MNRAS 448, 2430
- van Regemorter H., 1962, ApJ 136, 906
- Voit G. M., Weymann R. J., Korista K. T., 1993, ApJ 413, 95
- Wade R. A., 1984, MNRAS 208, 381
- Wade R. A., 1988, ApJ 335, 394
- Walton D. J., Miller J. M., Harrison F. A., Fabian A. C., Roberts T. P., Middleton M. J., Reis R. C., 2013, ApJ Letters 773, L9
- Wang B., Han Z., 2012, NAR 56, 122
- Warner B., 2003, Cataclysmic Variable Stars
- Weymann R. J., Morris S. L., Foltz C. B., Hewett P. C., 1991, ApJ 373, 23
- White N. E., Stella L., Parmar A. N., 1988, ApJ 324, 363

- Wills B. J., Brotherton M. S., 1995, ApJ Letters 448, L81
- Woltjer L., 1959, ApJ 130, 38
- Woods D. T., Klein R. I., Castor J. I., McKee C. F., Bell J. B., 1996, ApJ 461, 767
- Woods J. A., 1991, Ph.D. thesis, D. Phil thesis, Univ. Oxford , (1991)
- Yong S. Y., Webster R. L., King A. L., 2016, PASA 33, e009
- Zakamska N. L., Strauss M. A., Krolik J. H., Collinge M. J., Hall P. B., Hao L., Heckman T. M., Ivezić Ž., Richards G. T., Schlegel D. J., Schneider D. P., Strateva I., Vanden Berk D. E., Anderson S. F., Brinkmann J., 2003, AJ 126, 2125
- Zanstra H., 1929, Publications of the Dominion Astrophysical Observatory Victoria 4, 209
- Zhang S. N., Cui W., Chen W., 1997, ApJ Letters 482, L155
- Zhou H., Wang T., Wang H., Wang J., Yuan W., Lu Y., 2006, ApJ 639, 716
- Zubovas K., King A., 2013, ApJ 769, 51